SEISMIC LITHOFACIES PREDICTION AND RESERVOIR CHARACTERISATION IN DEEP-OFFSHORE NIGER DELTA, NIGERIA

BY

EBERE BENARD
(119078152)
(B.Sc. (Geology) and M.Sc. (Exploration Geophysics), University of Port Harcourt)

A THESIS SUBMITTED TO THE SCHOOL OF POST GRADUATE STUDIES UNIVERSITY OF LAGOS, AKOKA LAGOS, NIGERIA FOR THE AWARD OF DOCTOR OF PHILOSOPHY (Ph.D.) DEGREE IN GEOPHYSICS.

DECEMBER, 2016

SCHOOL OF POSTGRADUATE STUDIES
UNIVERSITY OF LAGOS

CERTIFICATION

This is to certify that the Thesis:

SEISMIC LITHOFACIES PREDICTION AND RESERVOIR CHARACTERIZATION IN DEEP-OFFSHORE NIGER DELTA, NIGERIA

Submitted to the
School of Postgraduate Studies
University of Lagos

For the award of the degree of

DOCTOR OF PHILOSOPHY (Ph.D.)

is a record of original research carried out

By:

BENARD, EBERE
In the Department of Geosciences

EBERE BENARD		08/12/16
AUTHOR'S NAME	**SIGNATURE**	**DATE**
Prof. Elijah A. Ayolabi		12/12/2016
1ST SUPERVISOR'S NAME	**SIGNATURE**	**DATE**
2ND SUPERVISOR'S NAME	**SIGNATURE**	**DATE**
DR Akinmosin, A.	RAP.	08-12-2016.
3RD SUPERVISOR'S NAME	**SIGNATURE**	**DATE**
DR. L. ADEOTI		08-12-2016
1ST INTERNAL EXAMINER	**SIGNATURE**	**DATE**
PROF S. B. OLOBANIYI		8/12/16
2ND INTERNAL EXAMINER	**SIGNATURE**	**DATE**
Prof M. O. OLORUNFEMI		08/12/2016
EXTERNAL EXAMINER	**SIGNATURE**	**DATE**
DR. O. G. Omogunloye		08/12/2016
SPGS REPRESENTATIVE	**SIGNATURE**	**DATE**

DEDICATION

To my late father and grand father

In memoriam

ACKNOWLEDGEMENTS

I wish to express my sincere gratitude to my supervisors: Prof. E. A. Ayolabi, Dr. C. O. Dublin-Green and Dr. A. Akinmosin; for their support and contributions towards the success of this research work. I also want to thank the Head of Department, Prof. S. B. Olabaniyi; Dr. L. Adeoti, Dr. S. Bankole, Dr. A. Opatola, Dr. S. Oladele, all the academic and non-academic staff of the Geosciences' Department, who had assisted me for the successful completion of the Ph.D research work.

I give special thanks to Sarah Kabon, Glen Penfield, and Prof. N. F. Ukaigwe for their immense support and inspiration in the course of this project work.

May I also acknowledge the management of SAPETRO, Total, Petrobras, Chinese National Oil Company (CNOOC), Nigerian National Petroleum Company (NNPC) and, the Department of Petroleum Resources (DPR) for providing the data set for this project with permission to publish the research results. My appreciation also goes to Schlumberger for providing Petrel software for this research.

I will not forget to acknowledge my friends: Gabriel Omolaiye, Clement Onyekwelu; my younger brother King Benard and many other persons for their encouragement.

Finally, I thank my wife Rosita Benard, my son Jeremy Benard, and my daughter Tiffany Benard for their sacrifice of time and love.

TABLE OF CONTENTS

CHAPTER TWO: LITERATURE REVIEW

CHAPTER THREE: MATERIALS AND METHODS

CHAPTER FOUR RESULTS AND DISCUSSION

List of Tables

List of Figures

ABSTRACT

The deepwater Niger Delta is associated with local mud diapirism and complex sand distribution. Hence, sequence stratigraphic prediction of reservoir sands and seal, as well as geostatistical reservoir characterisation, have not been effective in the deepwater environments due to the isolated nature of the reservoir sand bodies dispersed in shale-prone environments. Consequently, the exploration risk of drilling dry holes and the challenges of deepwater field development are very high. Hence, this study is aimed at predicting and characterising deepwater reservoir systems, as a means of reducing geologic uncertainties in the study area.

About 600 km^2 of three dimensional seismic data, log suite from seven wells, and 60 m sedimentological core footage were utilized in the study. The methodology combined qualitative log analysis, petrophysics, rock physics, seismic attribute analysis, sedimentology, and geostatistics.

Sedimentological evidence from core including sand injectite, floating mudclast, faint normal grading, parallel lamination, lenticular beddings, normal and inverse grading, has shown that the sedimentation mechanisms in the deepwater Niger Delta comprises of sediment slumping, sliding, debris flow, turbidity current flow, pelagic and hemipelagic settling, with no diagnostic support for hyperpycnal flow. Also, the study has shown the depositional model to be a hybrid of turbidite fan, debrite lobes and channel sands dispersed in background shale. The predicted reservoir facies include channels sands and fan lobes having good to excellent reservoir qualities, with porosity ranging between 0.21 and 0.36. The reservoir sands are easily distinguished from the background shale based on diagnostic elastic properties which measure stiffness, rigidity, and incompressibility. The reservoir sands are characterised by low lambda-rho, low Poisson's ratio, low primary versus shear wave velocity ratio, low closure stress scalar; and high mu-rho. This study has also shown the diagnostic post-stack seismic attributes for reservoir characterization in the study area to include: sweetness, envelope, reflection intensity, and root mean square amplitude. These diagnostic seismic attributes have correlation of between 0.66 and 0.8 with elastic rock properties in predicting lithofacies. Also, the use of seismic attributes as training image for geostatistical modeling of channel sands and fan lobes reconstruct reservoir geometries much better for field development than variogram and object-based geostatistical techniques.

Finally, this study has proved that the integration of rock physics, post-stack seismic attributes and sedimentology is very effective in addressing the inherent challenges of predicting and characterizing geometrically complex reservoir facies in the shale-prone deepwater setting of the offshore Niger Delta.

Key words: Characterisation, deepwater, geostatistics, seismic attribute, seismic lithofacies.

CHAPTER ONE

1.0 INTRODUCTION

1.1 Background to the Study

The ability to discriminate lithofacies based on rock physics properties and diagnostic seismic attributes, is key to deepwater siliciclastic reservoir facies prediction and characterisation. Sandstones and shales in siliciclastic Formations have been observed to deform differently at specific burial depth (Bjorlykke, 2010). This implies that rock physics analysis of critical changes in the gross rock rigidity and incompressibility can be used to discriminate between lithofacies types in siliciclastic depositional setting like the deepwater Niger Delta (Avseth and Mukerji, 2002; Goodway *et al*., 2010). Primary wave velocity, shear velocity, density, elastic moduli, and their associated derivatives have been proved to be reliable in discriminating between hydrocarbon sand, wet sand and shale in siliciclastic environments. On the order hand, seismic waveform and multi-attribute analysis of three dimensional (3D) seismic data are useful in mapping the morphology of deepwater clastics (Avseth *et al*., 2000; Hart, 2008).

Seismic attributes are derivatives from the original amplitude seismic that can be used to characterise lithological variation, stratigraphy, faults and fractures, hydrocarbon responses, as well as subtle detection of depositional facies architecture from seismic in three dimension (Hart, 2002). Several attributes have been formulated over the years including, stratigraphic, structural, and complex trace attributes. The complex trace analysis mathematically involves the Hilbert transformation of a real seismic trace to its imaginary component. While the real seismic trace represents the kinetic energy of particles that oscillate with respect to seismic wave energy; the imaginary signal measures the potential energy within the rock medium (Taner *et al*., 1979).

According to Ulrych *et al*. (2007), seismic attributes can be extracted instantaneously from common mid-point seismic data to review subtle geologic features.

Of particular interest to this study, is the fact that deepwater clastics and turbidite systems in the deepwater Niger Delta and similar depositional settings are associated with diapiric structural evolution and complex sand distribution (Corredor *et al*., 2005). This has strong implication in exploration, lithofacies prediction, reservoir characterisation, inter-well property modeling and field development (Deptuck *et al*., 2003; Adeogba *et al*., 2005, Corredor *et al*., 2005; Heino and Davies, 2006; Connor *et al*., 2009; Stevenson *et al*., 2012; and Celik, 2013). Hence, it is obvious that to reduce exploration risk associated with reservoir prediction; and to reduce uncertainty in the reservoir characterisation of deepwater clastics, it is important to establish a quantitative relationship between siliciclastic reservoir properties with seismic responses. According to Avseth *et al*. (2001), there is a link between amplitude characteristics and depositional patterns. Hence it is possible to discriminate lithofacies and fluid changes in attribute maps and strata cubes.

The focus of this study is to integrate quantitative rock physics, 3D seismic attributes data and core in order to reduce geologic risk and uncertainties inherent in the offshore Niger Delta. This is necessary as deepwater reservoir systems have been recognized as complex and variable. The complexity is reflected in the depositional mechanism, depositional environment, external morphology and geometry, sand distribution and reservoir quality of deepwater deposits (Stow *et al*., 1999; Caers *et al*., 2001; Strebelle, 2002). Massive sand bodies of economic importance are usually associated with deepwater systems in siliciclastic basins of West Africa (Shanmugam, 2006). Also, notable petroleum producing sandstone reservoirs have been reported in the North Sea, Norwegian Sea, Gulf of Mexico, Offshore Brazil, and Offshore West Africa including the

Offshore Niger Delta (Shanmugam, 2006). But, irrespective of the economic importance of the deepwater systems, the technical challenges associated with the exploration and the recovery of hydrocarbon in related reservoir types still remain very high (Wood *et al*., 2000).

1.2 Statement of the Problem

The study area lies within the mud diapir, inner fold and thrust belts of the deep offshore Niger Delta, characterised by interplay of local mud diapirism and complex sand distribution pattern. Hence, exploration and reservoir characterisation methods including: regional seismic and sequence stratigraphic techniques, seismo-structural mapping, and the use of outcrop analogs, have not been very effective in the study area (Lawrence and Bosman-Smith, 2000; Bakke *et al*., 2013). The reason being that deepwater depositional facies exhibit different external geometries on seismic data that are not diagnostic of unique depositional systems tracts. Hence, reservoir and seal prediction is difficult in the deepwater and ultra-deepwater (Posamentier *et al*., 1991; Steffen, 1993; Shanmugam, 2006). Consequently, inter-well lithofacies and property prediction using variogram and object-based geostatistical methods are unreliable in deepwater channel and turbidite environment due to their complex depositional geometries and architectures (Caers *et al*., 2001; Strebelle, 2002). This depositional environment consist of isolated reservoir sand bodies encased in background shale. Hence, there is therefore the need to integrate rock physics, 3D seismic attributes and sedimentology, in order to address the inherent reservoir prediction challenges in the study area, and therefore reduce geologic uncertainties.

1.3 Aim and Objectives of the Study

The aim of this study is to characterise deepwater reservoir systems and predict lithofacies types by integrating rock physics, seismic attributes, and sedimentological core data, as a means of reducing geologic uncertainty in exploration and field development in the study area.

The specific objectives of the study are to:-

i. investigate the mechanisms of deepwater sedimentation;
ii. characterise and define the depositional model for sand distribution;
iii. identify deepwater reservoirs and discriminate their elastic rock physics properties;
iv. determine the most appropriate post-stack seismic attributes for reservoir characterisation; and
v. compare results of calibrated seismic attributes as input for multiple point geostatistics, with two-point variogram and object-based facies modeling techniques.

1.4 Significance of the Study

The integration of rock physics, seismic attributes and core sedimentological analysis will provide information on the processes and mechanism of sandstone deposition, architectural facies patterns and depositional environment in the study area. These information will aid reservoir characterisation and conceptual geological modeling of the study area. These knowledge will in turn aid the direct prediction of hydrocarbon sands using seismic data, as well as the geostatistical modeling of sandstone facies for reservoir characterisation and field development studies.

1.5 Definition of Terms

Attribute: Specific information set used to describe a property.

Complex Seismic Trace: Representation of seismic data as real and imaginary amplitude data through a 90 degrees phase shift.

Deepwater: Water depth greater than 200 m below the offshore continental shelf.

Diapir: Massive low density flow structure such as shale (mud) and salt.

Elastic Rock Property: Rock property derived from the combination of primary wave velocity, secondary wave velocity and density.

Facies: A body of rock that can be defined by specific properties and characteristics.

Fault: Vertical displacement of rock layers along the plain of movement.

Formation: Mappable geological units.

Fold: Structural deformation that results to bending of planner surfaces.

Geostatistics: A subset of statistics used to describe and analyze spatial variability of subsurface geological variable.

Lithofacies: A rock unit that is defined by the lithological composition.

Lithology: Rock unit defined by specific physical characteristics such as colour, texture, grain size and mineral composition.

Meandering channel: A bending river landscape.

Primary Seismic Wave: The first seismic signal that is reflected through a subsurface rock layer.

Post-Stack Seismic: Seismic data volume that is processed after the individual traces have been merged.

Reservoir: A porous rock unit that can house fluid and allow it to flow.

Seismic: Energy **waves** that travels through the earth layers as a result of rock vibration.

Seismic Lithofacies: A rock unit that is characterised by unique acoustic and elastic seismic properties.

Siliciclastic: Silica rich sedimentary rocks formed and deposited through mechanical processes.

Sedimentary Rock: Aggregate of minerals derived from pre-existing rocks through weathering, transportation, deposition and burial.

Sandstone: Sedimentary rock composed of aggregate of quartz-rich grains with particle size between 1/16 mm and 2 mm.

Shale: Fine grained clastic sedimentary rock composed of clay rich minerals and mud.

Shear Seismic Wave: The second seismic signal that is reflected through a subsurface rock layer.

Seismic Trace: Collection of seismic wavelets characterised by basic physical properties such as amplitude, wavelength and frequency.

Stratigraphy: The description of different rock layers.

Sedimentology: The study of the processes of formation and environments where sandstone, shale, and mud and deposited.

Turbidites: This refers to sediments deposited by sediment-laden water currents along a slope or channel.

Variogram: Bivariate statistical measure of spatial relationship between variables.

Wavelet: Basic unit of a seismic trace.

1.6 Abbreviations

3D: Three Dimension

AVO: Amplitude Variation with Offset

CSS: Closure Stress Scalar

GR: Gamma Ray

Max: Maximum

Min: Minimum

MPS: Multiple Point Statistics

PEF: Photo Electric Factor

RI: Reflection Intensity

RMS: Root Mean Square

Vp: Primary Wave Velocity

Vs: Shear Wave Velocity

CHAPTER TWO

2.0 LITERATURE REVIEW

2.1 Previous Work

Most research works in the deepwater Niger Delta were focused on the understanding of the structural complexity in the fold and thrust belts (Wu and Bally, 2000; Corredor *et al.*, 2005; Connor *et al*., 2009). Published articles in the Niger Delta offshore belts are scarce in the area of quantitative seismic facies prediction and geostatistical modeling of channels and turbidite reservoir systems been a frontier exploration province (Adeogba *et al*., 2005; Heino and Davies, 2006; Stevenson *et al.*, 2012; and Celik, 2013). In similar geologic setting of the deepwater Gulf of Mexico, seismic geometries are more indicative of local basinal processes such as diapirism and slumping than extrabasinal controls including: sea level change, regional subsidence and provenance (Lawrence and Bosman-Smith, 2000; Bakke *et al.*, 2013). The implication is that the deepwater environment is characterised by several minibasins having differential supply of clastic sediments. Hence, within a depositional episode, some minibasins will receive large volume of sand, while others may receive only mud. Hence, regional sequence stratigraphic criteria for reservoir and seal prediction in deepwater sediments are difficult to define (Posamentier *et al*., 1991; Steffen, 1993). Consequently, regional data base of the continental shelf, shallow slope, shallow analog and outcrop studies of turbidite systems have not been very effective for deepwater facies prediction. In the deep-water fold and thrust belts, depositional facies including more distal basin fans are associated with structural traps formed by contractional folds as in the case of Agbami, Bonga, Chota, Ngolo and Nnwa deep-water fields (Corredor *et al*., 2005; Biloti and Shaw, 2005).

Turbidite and deepwater channel reservoir systems are associated with complex sand distribution (Caers *et al*., 2001). They can simply be defined as isolated sand facies surrounded by shale in characteristic slope, basin floor, and channel setting. These facies types constitute technical challenge in reservoir characterisation and deepwater development studies, including: reservoir and seal prediction as well as inter-well sand correlation (Wood *et al*., 2000). Also, the mechanism of deepwater sedimentation has been a subject of debate. In marine and lacustrine environments, meandering channel levee systems and distal fan lobes have been attributed to powerful hyperpycnal flow over long distances on the sea bed (Mutti *et al*., 1996; Zavala *et al.*, 2006; Mulder and Chapron, 2011). Turbidity current and debris flow models have also been proposed respectively for the deepwater Niger Delta and Angola (Graue, 2000; and Abreu *et al*., 2003). Incorrect use of these models have implication in frontier exploration (Shanmugam, 1998).

The technical challenges of deepwater hydrocarbon exploration, development and production, still remain high due to inherent complex depositional pattern of turbidite and channel sands. According to Pettingill and Weimer (2001), over 70% of unrecovered hydrocarbon are trapped in turbidite and related reservoir systems. Consequently, two-point geostatistical methods using variogram analysis are not very efficient in modeling reservoir properties in depositional settings associated with complex geometrical trends such as turbidite lobes and sinuous channels (Strebelle, 2002). Variogram estimation is inherently affected by insufficient data pairs, extreme values, presence of outliers, and biased geological sampling for effective averaging and prediction of unsampled locations (Kelkar and Perez, 2002). However, to accurately represent complex geologic features such as turbidites and channel sands, a measure of correlation between multiple spatial locations is required.

Some authors have reported the application of seismic attributes as being very useful in predicting reservoir properties such as lithology, volume of shale, net-to-gross sand and porosity in complex depositional environments (Leiphant and Hart, 2001; Meyer *et al*., 2001; McGrory *et al*., 2006). This implies that lithology sensitive seismic attributes can serve as training image for facies classification and multiple point facies modeling of complex reservoirs. Hence, the use of high resolution seismic attributes as training images, can be integrated as a complimentary technique to the use of variogram, in modeling complex curvilinear reservoirs systems (Journel, 2005).

2.2 Location of the Study Area

The field under study is situated within the mud diapir, inner fold and thrust belt of deepwater Niger Delta, at water depth greater than 1000 m. The area of study covers approximately 600 km^2 in areal extent. The geology is very complex, and is characterised by rapid deposition of prograding sands on over-pressured mobile shale of the Akata Formation. The sedimentary succession of the slope and basin floor deepwater setting, is considered to be dominated by pelagic and hemipelagic marine shales (>80%); with interbedded sandstone deposits of debris flow, turbidites and channel-levee complexes (Graue, 2000). According to Corredor *et al*. (2005), the offshore Niger Delta has been subdivided into five structural zones with distinct depositional framework (Figures 1 and 2). These zone include the following:-

i. Extensional province: This zone lies beneath the continental shelf and is characterised by both basinward-dipping and counter-regional growth faults, associated rollovers and depocenters.

ii. Mud diapir zone: This is located beneath the upper continental slope, and is characterised by passive, active and reactive mud diapirs. The mud diapirs include shale ridges and massifs, shale overhangs, vertical mud diapirs, and interdiapir depocenters.

iii. Inner fold and thrust belt: This zone extends in an actuate path across the center of the offshore delta. It is characterised by basinward verging thrust faults and associated folds. It consist of Tertiary to Holocene deep marine sediments.

iv. Transitional detached fold zone: This zone lies beneath the lower continental slope, and is characterised by large areas of little or no deformation. It is interspersed with large detachment folds above structurally thickened Akata Formation.

v. Outer fold and thrust belt: It consists of northern and southern sections that define two outer lobes of the delta. It is characterised by both basinward and hinterland-verging thrust faults and associated folds. Growth sedimentation rates are low relative to uplift.

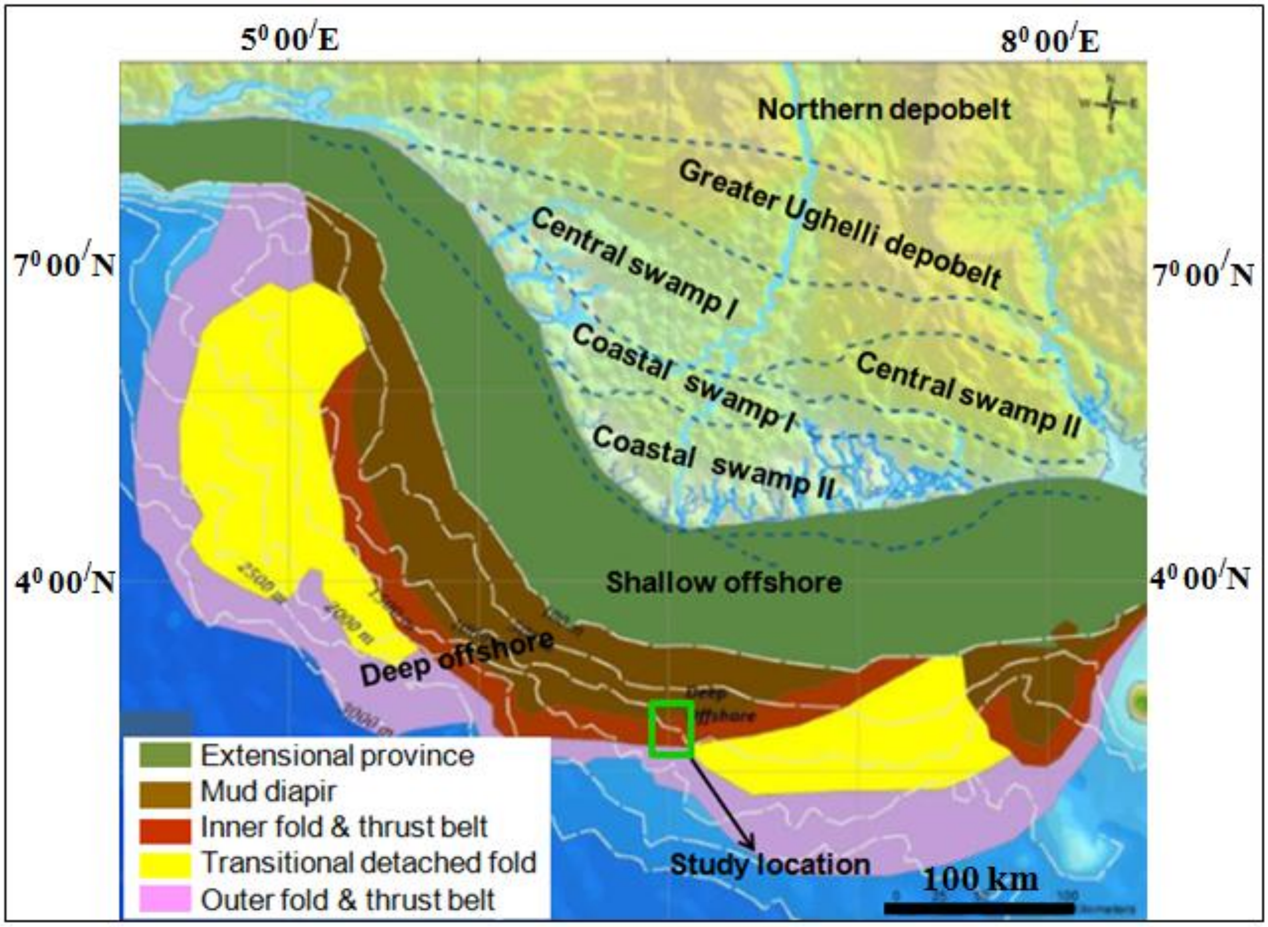

Figure 1: Map of Niger Delta showing the study location, the depobelts, and five offshore structural provinces (Adapted from Corredor, *et al*., 2005)

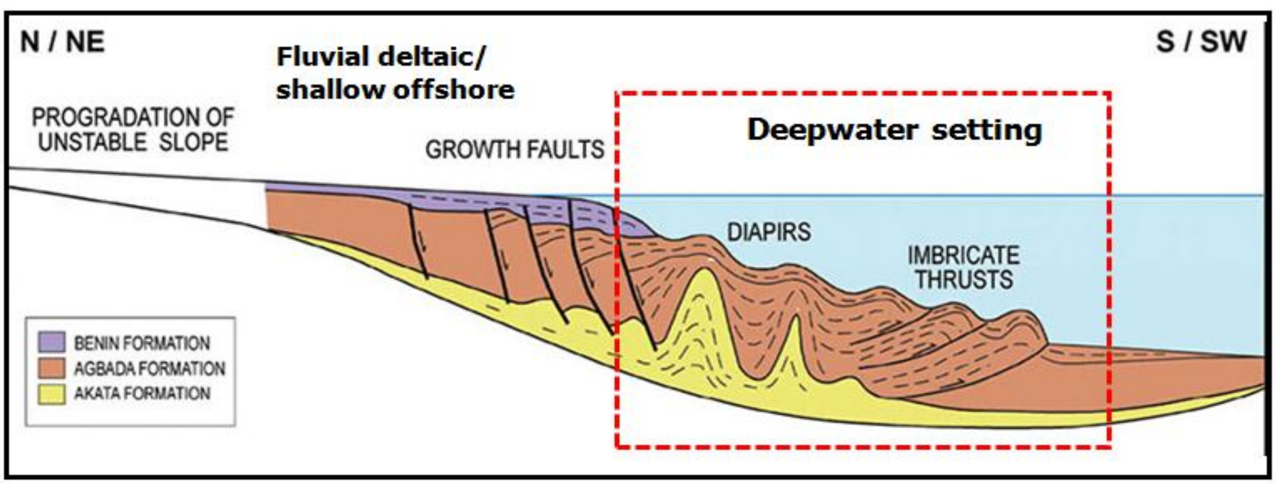

Figure 2: Geologic cross section of the Niger Delta continental shelf and offshore setting (After Corredor *et al.*, 2005)

2.3 Geology of Niger Delta

The Niger Delta Basin is situated on the passive margin of West Africa. The sub-aerial part of the delta covers about 75,000 km2 and extends for more than 300 km from the apex to the mouth (Figure 3). The basin started as a proto-Niger Delta following the tectonic evolution of the Benue-Abakaliki Trough (Bustin, 1988). This tectonic episode occurred in the Early Cretaceous as a failed arm of a rift triple junction associated with the opening of the South Atlantic (Burke, 1972; Weber and Daukoru, 1975; Whiteman, 1982). The Niger Delta is characterised by major regressive phase from the Eocene to Holocene; this was initiated by the uplift of the Benin and Calabar flanks during the Paleocene to Early Eocene (Murat, 1972). Following the Miocene uplift of the Cameroon Mountains, the Niger Delta has prograded with the seaward shift of the coastline (Whiteman, 1982). The modern Niger Delta records major regressive-transgressive sequences in the Late Pleistocene; this is related to eustatic sea level changes during the late glaciation (Allen, 1965; Oomkens, 1974). Cretaceous tectonic elements of the Benue Trough had influenced the drainage pattern in the lower Anambra Basin. Consequently, the early Niger Delta in the Eocene to middle Miocene began to advance southwards along three distinct sedimentary axes. The Niger Delta continued to grow in the Eocene in response to the epeirogenic movements along the Benin and Calabar flanks (Murat, 1972). According to Allen (1963), about 22 distributaries discharges radially into the basin in the modern Niger Delta. These river systems serve as fairway for sand transportation into the deepwater settings. Three of these rivers: Ramos, Forcados in the west and Nun River at the delta nose carry over 70% of sediments into the sea. Erosional canyons of early to middle Miocene age were incised in the Niger Delta shelf and slope during periods of sea level fall (Doust and Omatsola, 1990). Several large submarine fan channels extend down slope across the continental rise from erosional submarine canyons on the upper slope (Damuth, 1994). Major canyons in the offshore Niger Delta include, Lagos, Avon, Mahin, Niger, Qua-Ibo and Calabar canyon.

The Niger Delta Basin is characterised by three main lithostratigraphic units, the Akata, Agbada, and Benin Formation from the oldest to the youngest (Short and Stauble, 1967). Sediment deposition in the Tertiary prograding Niger Delta Basin is complicated by depositional patterns restricted to series of fault-controlled sub-basins, referred to as depobelts that strike northwest to southeast, sub-parallel to the present shoreline (Knox and Omatsola, 1989). The depobelts were associated with increasing deltaic sediment loads that forced underlying marine shale to move upward and basinward. The depobelts represent different offlapping siliciclastic sedimentation cycles in the Niger Delta (Stacher, 1995). Each depobelt is a separate unit defined by a break in the regional dip of the prograding delta, and is bounded landward and basinward by growth faults and counter regional faults or growth faults of the next seaward belts respectively (Evamy *et al.*,1978; Doust and Omatsola,1990). As shown in Figure 1, five depobelts have been recognized in the Niger Delta based on their sedimentology, deformation and petroleum history. According to Doust and Omatsola (1990), the northern delta depobelts which include the Northern and Greater Ughelli depobelts overly relatively shallow basement and have the oldest faults. The central delta depobelts consisting of Central swamp I, Central swamp II, Coastal swamp I and Coastal Swamp II have well defined structures. While the distal depobelts including: the Shallow offshore and deep offshore depobelts are structurally complex due to internal gravity tectonics on the modern continental slope.

2.4 Stratigraphy and Depositional Environment of Deepwater Niger Delta

The Niger Delta is a prograding delta with three main lithostratigraphic units: Akata, Agbada, and Benin Formation in ascending order (Figure 3b). The Formations are stratigraphyically related in space and time, having ages between Eocene and Holocene. These Formations also have lateral equivalent in the Anambra Basin of the Lower Benue Trough (Table 1). The stratigraphy of Niger Delta is subdivided into the following units: an upper sequence of massive sand and gravel deposited under continental condition, transitional series of sandstone and shale intercalation deposited under a parallic condition, and a basal marine shale section with isolated sand lenses and turbidite deposits (Evamy *et al*., 1978). According to Nwachukwu and Chukwura (1986), the depositional environments for the Niger Delta clastics span from the delta plain in the continental setting, through a transitional delta front environment, to the prodelta and submarine fan environment typical of the deepwater Niger Delta.

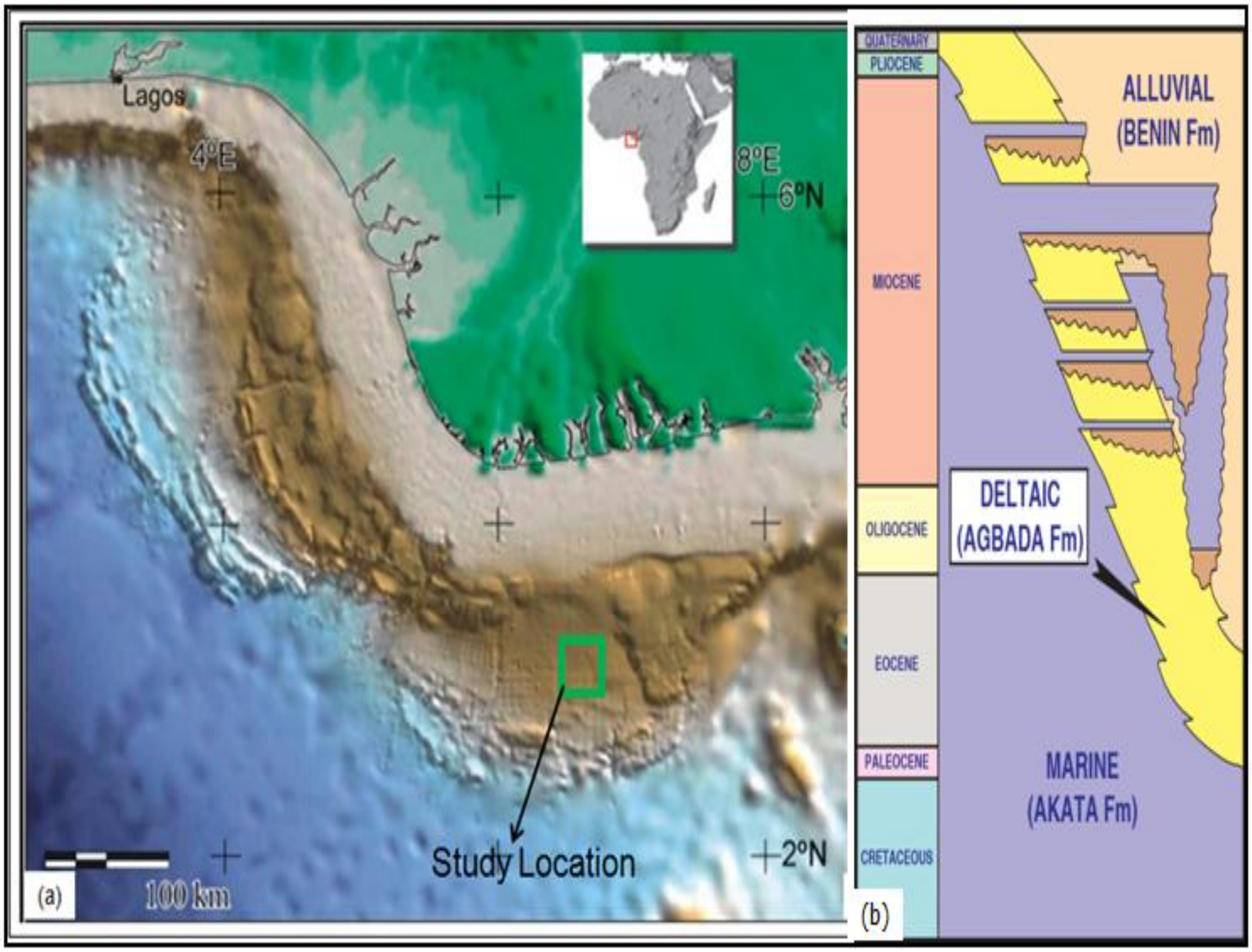

Figure 3: (a)Bathymetry sea floor (After Corredor *et al*., 2005) and (b) Stratigraphic column (After Tuttle *et al*., 1999)

Table 1: Niger Delta and Anambra Basin Geologic Formations (Modified from Short and Stauble, 1967).

SUBSURFACE			OUTCROP		
FORMATION	**AGE**	**M.A**	**FORMATION**	**AGE**	M.A
BENIN	**Oligocene-Recent**	**<33.9**	**BENIN**	**Miocene?** **Pleistocene/Pliocene**	**23.0-0.01**
AGBADA	**Eocene-Recent**	**<56**	**OGWASHI-ASABA**	**Oligocene - Miocene**	**33.9-23.0**
			AMEKI	**Eocene**	**56 -33.9**
AKATA	**Eocene-Recent**	**<56**	**IMO**	**Paleocene - L. Eocene**	**66 -56**
EQUIVALENT NOT KNOWN			**NSUKKA**	**Maastrichtian - Paleocene**	**72.1 -56**
			AJALI	**Maastrichtian**	**72.1 - 66**
			MAMU		
			NKPORO	**Campanian-Santonian**	**83.6-72.1**
				Campanian/Maastrichtian	**86.3 - 66**
			AWGU	**Turonian-Coniacian/Santonian**	**93.9-83.6**
			EZE-AKU SHALE	**Turonian**	**93.9-89.8**
			ASU RIVER GROUP	**Albian**	**113 -100**

The delta plain environment is generally associated with sandstone units representing braided stream, point-bar, channel-fill, and crevasse splays, as well as back-swamp shale deposits (Frankl and Cordry, 1967; Weber, 1971). The depositional environments within the delta front are characterised by tidal channel, distributary mouth bar, lagoon, barrier bar deposits, and beach sands. The prodelta and submarine fan environments are peculiar to the deepwater Niger Delta, with continuous deposition of pelagic and hemipelagic shale. This shale unit is mainly under-compacted and over-pressured, and also contains isolated sand lenses and turbidite (Avbovbo, 1978).

2.4.1 Benin Formation

The Continental Benin Formation is the uppermost unit in the Niger Delta and is composed of Late Eocene to Holocene continental deposits. These include alluvial and coastal plain sands that are about 2000 m (6600 ft) in thickness (Avbovbo, 1978). Onshore in some coastal regions, the Benin Formation overlies the Agbada Formation (Kulke, 1995). Offshore, the continental sands of the Benin Formation become thinner and disappear near the shelf edge (Cohen and McClay, 1996) as illustrated in Figure 2. On seismic sections, the Benin Formation exhibits parallel reflection configurations that are associated with variable frequency and amplitude; as well as low discontinuities that decrease landwards.

2.4.2 Agbada Formation

This formed the major petroleum-bearing unit in the Niger Delta. The paralic clastic sequence known as the Agbada Formation is present in all the depobelts and ranged in age from Eocene to Pleistocene. It is more than 3500 m (11,500 ft) thick and represents the actual deltaic sequence that accumulated in the delta-front, delta-topset, and fluviodeltaic environments (Doust and Omatsola, 1990). Channel and basin floor fan deposits in the Agbada Formation formed the primary reservoirs in the Niger Delta. On seismic, they are characterised by parallel, hummocky, acoustically chaotic, slightly divergent, highly divergent and sigmoid/oblique clinoform (Adeogba *et al.*, 2005).

2.4.3 Akata Formation

This is composed of clays, shales and silts which occur at the base of the delta sequence. The Akata Formation is generally believed to contain source rocks; and might also contain some turbidite sands. On seismic sections, the Akata Formation is generally devoid of internal reflections, with the exception of a strong, high-amplitude reflection that was locally present in the middle of the formation (Bilotti and Shaw, 2005). On the other hand, the mid-Akata Formation served as an important structural marker for defining detachment levels, and is recognized on seismic section as transparent and chaotic reflections. The Akata Formation exhibited low primary wave seismic velocities (≈2000 m/s; ≈6600 ft/s), and in addition reflects regional fluid overpressures (Bilotti and Shaw, 2005). The Formation has a thickness range of about 2000 m (6,600 ft) to 7000 m (23,000 ft). In deep-water, it is up to 5000 m (16,400 ft) thick (Doust and Omatsola, 1990). The Akata Formation, being composed of massive shale deposits and turbidite sands would likely occur on seismic as acoustically chaotic and transparent facies (Adeogba *et al.*, 2005).

2.5 Petroleum Geology and Petroleum System of Deepwater Niger Delta

2.5.1 Petroleum Geology

The classification scheme of Worrall *et al*. (2001) has been used to describe the petroleum geology of deepwater systems and to divide the plays into four types of basins:

a. Basins with large mobile substrates, fed by large rivers: These basin types are associated with large volume of sediments transported into the deepwater environments. They have high potential for reservoir presence, and may have multiple play types and migration pathways. Large volume of sedimentary fill deposited within extensional and contractional domains, in this type of basin favours hydrocarbon generation. The mobile substrate in deepwater Angola (Congo Basin) and northern Gulf of Mexico consists of salt, while the deepwater Niger Delta has mobile shale substrate.

b. Basins with mobile substrates fed by small rivers: These are common along steep margins, where high-sediment-load smaller rivers flow into the basin. Typical examples include the Island of Borneo and the Campos Basin in Brazil. Neocomian lacustrine source rocks occur below mobile Aptian salt in the Campos Basin.

c. Basins with non-mobile substrates fed by small rivers: These basins type are characterised by the reservoirs draping over basement highs, which directly affects petroleum migration. The Wet Shetland island, More and Voring Basins in Offshore Norway fall under this basin type (Gjelberg *et al*., 2001)

d. Basins containing non-deepwater reservoirs: These basin type contain reservoirs that were not originally deposited in deepwater setting. The paleo-environment may have been fluvial, deltaic or shallow marine. Jurassic and Cretaceous fluvial-deltaic syn-rift strata in the north-west shelf of Australia, carbonate reservoirs in the Maampaga Field of

Philippines, and some Albian discoveries in the Campos Basin, Brazil, are typical examples of non-deepwater reservoir in deepwater basins.

2.5.2 Petroleum Systems

Six basic elements of the petroleum systems of the deepwater and ultra deepwater settings as described by Pettingill and Weimer (2002), are summarized below:

i) Reservoir

Most deepwater discoveries were made in reservoirs of Cenozoic age, with the remaining contributions from Cretaceous reservoirs. About 90% of deepwater reservoirs are sandstone of deepwater origin, while the remaining 10% include shallow marine and fluvial sandstones, as well as carbonates. Deepwater reservoirs generally have good reservoir qualities, with over 30% porosity and thousands of milliDarcy permeability respectively. The good reservoir quality of deepwater reservoirs is a function of sedimentary processes of mature river systems transporting the sediments. High porosity of deepwater sandstones is attributed to low geothermal gradient and unconsolidation resulting from overpressure. Generally, deepwater reservoir connectivity and continuity ranges from poor to excellent. Also, high net-to-gross channel-fill and basin floor sheet sands, have excellent reservoir quality, while low net-to-gross channel-fill and thin-bed levees have poor reservoir quality. Low net-to-gross reservoirs pose more technical challenges in deepwater exploration and development. Consequently, the ability to predict deepwater reservoirs prior to drilling is critical.

ii) Traps

Trapping style in deepwater plays varies with basin type and tectonic regime. Significant proportion of turbidite plays have stratigraphic component to their traps. Common to the deepwater Niger Delta and other West African Basins, is a combination of structural-stratigraphic traps (Pettingill, 1998). Other trapping styles include: structural traps in emerging fold belts plays, and depositional mounding in unconfined settings (Kirk, 1994). Pure stratigraphic traps are also possible in unconfined setting due to lateral pinch out (Clemenceau *et al*., 2000).

iii) Seal

The deepwater marine environment is mud-prone and therefore associated with adequate top seals. However, seal integrity may pose serious risk due to overpressures and crestal faulting. Reservoir pressure, overburden pressure, and rock strength are critical elements for evaluating seal integrity.

iv) Source Rock

According to Duval *et al*. (1998), the deposition of potential marine source rocks in the deepwater environment, is associated with major marine transgressions and favourable oceanographic conditions. The source rock type may include Type I, II and III kerogens, which differ for different offshore basins. Different source rocks had been reported along the West African margin. In the deepwater sections of Niger Delta and northern Equatorial Guinea, the Akata Shale, Eocene to Oligocene in age, is considered the main source rock. It is progressively younger basinward with variation in efficiency towards the ultra deepwater setting (Doust and Omatsola, 1990; Tuttle *et al.*,1999). Deepwater related source rocks include Jurassic, Cretaceous and Tertiary strata. Lacustrine source rocks are common in the syn-rift setting such as the Campos Basin of Brazil and part of West African margin (Schiefelbein *et al.,* 2000). Also, Tertiary terigenous gas-prone materials have good source rock potentials. These materials initially deposited in coastal and shallow marine settings, are transported into deepwater environment during Tertiary lowstands to form oil-prone source rocks (Schiefelbein *et al*., 1999; Peters *et al*., 2000). There have been much discussion on the nature and distribution of source rock in the Niger Delta. The Akata Formation is considered the main source rock for hydrocarbon in the Niger Delta up to the deepwater environment in water depth of 2500 m (Bustin, 1988; Duost and Omatsola 1990; Haack *et al*., 2000; and Cobbold *et al*., 2008). However, Cretaceous source rocks have also been identified in the Niger Delta (Schiefelbein *et al*., 1999; Haack *et al*., 2000; Morgan, 2003; Saugy and Eyer, 2003).

v) Generation and Migration

Most source rocks in the deepwater environments are considered to have recently reached the hydrocarbon generation window, hence timing is of very high risk. Adjacent depocenters and faults serve as migration pathways for entrapments. The Cenozoic mobile shale in the deepwater Niger Delta are over-pressured with a system of fluid trapping and leaking that favours oil migration into fault traps. Faults and piercement structures can provide adequate vertical migration.

2.6 Deepwater Depositional Process and Environments

Common deepwater depositional processes include the following:-

- Gravity-driven flow (slides, slumps, debris flows, and turbidity currents)
- Deepwater bottom current

- Liquidization
- Clastic injection
- Mud diapirism
- Sediment plumes, wind transport, etc
- Pelagic and hemipelagic settling
- Tsunamis

The deepwater depositional environments associated with the processes listed above include: the deep-lacustrine environment, sub-marine slope environments, submarine canyon and gully environments, submarine fan environments, submarine non-fan environments, and submarine basin-plain environments.

2.6.1 Deepwater Depositional Processes

According to Shanmugam (2006), gravity-driven processes remained the most important mechanism for deepwater sediment transport into the deep marine environments. The gravity-driven processes include: slides, slumps, debris flows, and turbidity currents, commonly associated with shelf edge sediment failures. The mechanism of deepwater sedimentation typical of the different depositional processes, are best inferred from sedimentary features observed in core and outcrops. It is almost impossible to use plan morphological features on seismic data to interpret the mechanism of deepwater deposition. Typical gravity-driven deepwater processes and their associated features are presented thus.

i. **Sediment slides:**

This refers to the process and also the mass of sediment transported along a glide plane without any internal deformation. Large scale slides are seen in high-resolution seismic profile of modern systems. Diagnostic features of sediment slides include the following:-

- Gravel to mud lithofacies
- Clastic injections
- Sheet-like geometry
- Salt and shale diapirism

ii. **Slumps:**

This refers to mass of sediments transported along concave-up glide plane, with significant internal deformation due to rotational movement. Large scale modern slump occur as chaotic facies. Diagnostic features of deepwater slumps in sedimentary core include the following:-

- Gravel to mud lithofacies
- Basal zone of shearing
- Contorted layers interbedded with non-contorted layers at core scale
- Irregular upper contact
- Sand injections
- Steeply dipping and truncated layers
- Lenticular to sheet-like geometry with irregular thickness

iii. **Debris flow:**

This refers to slow moving mass of sediments that breaks up into smaller blocks at the axis of advance. Both muddy and sandy debris flow deposits (debrites) show the following features on core.

- Gravel to mud lithofacies
- Floating mudstone clast
- Planar clast fabric in muddy matrix
- Projected clast in mudstone
- Brecciated mudstone clasts in sandy matrix
- Planar clast fabric in sandy matrix
- Inverse grading of rock fragments
- Inverse grading, normal grading, inverse to normal grading
- Floating quartz granules in sandy matrix
- Inverse grading of granules in sands and pocket of gravel

iv. Turbidite:

This refers to deposits of turbidity currents. They are classified into coarse-grained, medium-grained and fine-grained turbidites with a standard sequence of structures within individual depositional units. Most turbidite deposits are associated with partial sequences (top-absent, mid-absent, base-absent). Important diagnostic features for recognition and interpretation of turbidites include the following:-

- Fine-grained sand to mud
- Normal grading without floating clasts or granules
- Reverse grading at base of thick coarse-grained beds

- Sequential grading within silt laminae in fine-grained beds
- Sharp or erosional base contact
- Gradational upper contact
- Thin layer (centimeter scale)
- Sheet-like geometry in basinal setting
- Lenticular geometry in channel-fill settings
- Parallel elongated clast
- Random orientation of clay particles
- Bioturbation at the top of beds

Generally, turbidity current versus debris flow models are used to predict reservoir sand distribution. Incorrect use of the models have implication in frontier exploration (Shanmugam, 1998). In the deepwater lower Miocene of offshore Angola, the origin of sinuous channel forms has been explained by turbidity currents (Abreu *et al*., 2003).

v. Sand injectite:

This results from the injection of sand into fine grained shale. It is caused by possible sedimentary slumping, depositional loading, glacial loading, tectonic stress, seismic induced liquification, igneous intrusion, and vertical migration of fluid.

vi. Mud diapirism:

This refers to sediment flowage and deformation due to rapid sedimentation caused by gravity instability. Sediment loading and rapid burial of cohesive sediments will commonly result to overpressure of the underlying mud.

vii. Pelagic and hemipelagic settling:

This refer to the settling of mud fractions derived from continental materials and shells of microfauna through the water column to the ocean floor. Common diagnostic features include the following:-

- Mudstone and shale lithofacies
- Parallel lamination
- Faint normal grading
- Bioturbation
- Deep-marine body and trace fossils

2.7 Deepwater Architectural Elements

Siliciclastic deposits in the deepwater environments have been classified into gravel-rich, sand-rich, mixed sand-mud, and mud-rich facies, based on grain size and sediment delivery systems (Reading and Richards, 1994; Richards *et al*., 1998). A three end-member sediment delivery systems have been defined for the deepwater systems which includes: single point-fed source fan, multiple point-source submarine ramp, and line-source submarine slope aprons. These depositional systems are characterised by five principal architectural elements: wedges, channels, lobes, sheets and chaotic mounds (Figure 4).

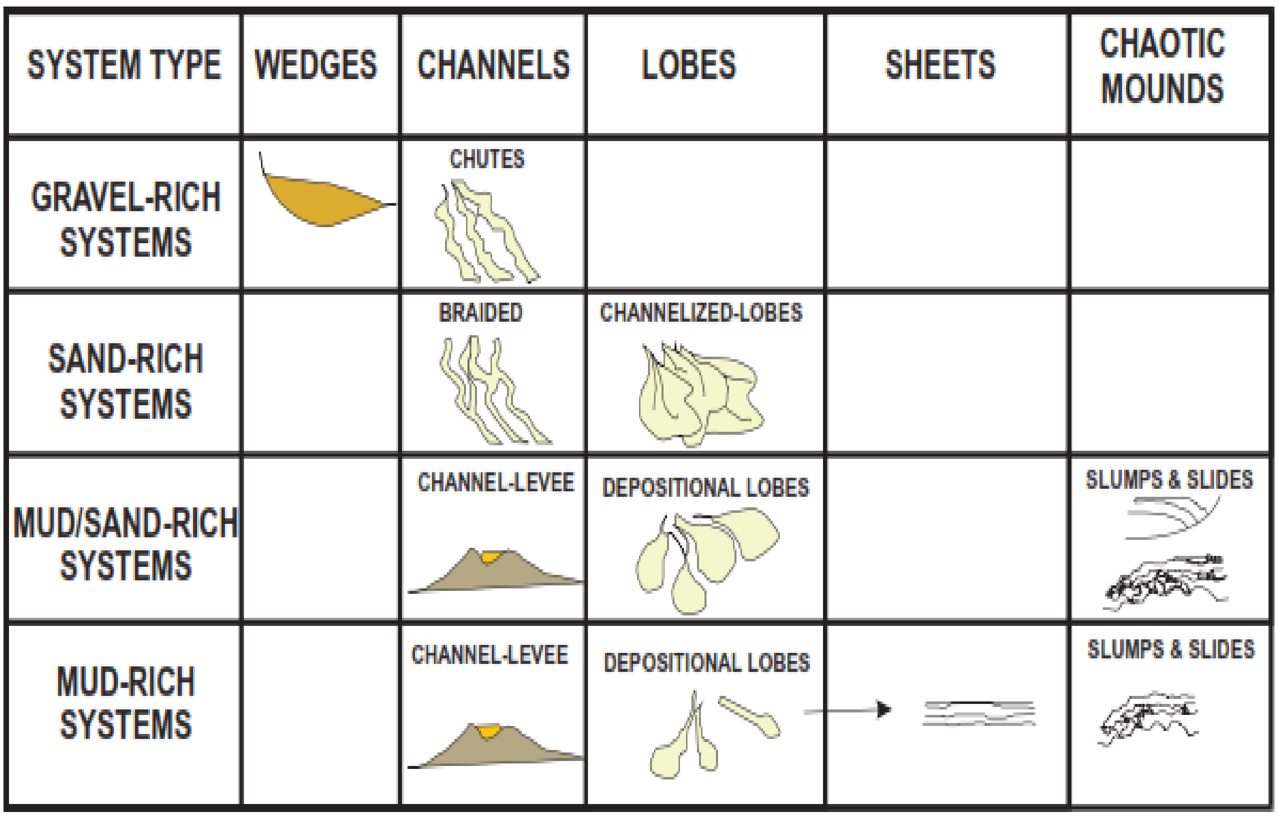

Figure 4: Principal architectural elements of deepwater clastic systems (After Readings and Richard, 1994)

- Wedges: This refers to sand-prone sedimentary unit that pinches out downslope by a downlap surface.
- Channels: This refers to elongate negative-relief features created by turbidity-current flow (Mutti and Normark, 1991). They represents extended linear fairway for sediment transport and depositions. Depending on grain size and sediment delivery systems, deepwater channels can be categorize as straight (chute and braided channels), and sinuous (channel-levees) geometries. Most channel-levee systems are associated with over-bank deposits. These are fine-grained, thin-bedded turbidite sediments, laterally extensive, and adjacent to the main channels in turbidite systems (Mutti and Normark, 1991).
- Lobes: Mutti and Normark (1987, 1991), defined lobes as areas of sand deposition, downslope from the main channel. Channelized lobes and depositional lobes are typical of deepwater settings.
- Sheets: Amalgamated and layered sand units, laterally continuous, with tabular external geometries are referred to as sheet (Mahaffie, 1994). The base of layered sheet sand is characterised by high net-to-gross, typical of the stacked assemblages of top-absent Bouma sequence. On the contrary, the upper section of sheet sands is characterised by low net-to-gross sand percentage, typical of a complete or base-absent Bouma sequence.
- Thin beds: This refers to very fine sands and silt deposits which include: levee, inter-channel, and outer fan/fringe deposits (Shew *et al.*, 1994). Thin beds generally contain ripple bedding, pinch-and-swell structures, convoluted beddings, minor bioturbation, and graded beds.

2.8 Deepwater Exploration History in Nigeria Niger Delta

Deepwater exploration in the offshore Niger Delta began in 1990, following the first acquisition of speculative two dimensional (2D) seismic data in the deepwater and ultra-deepwater Niger Delta offshore (Ofurhie *et al*., 2002). This seismic campaign was followed by a second 2D seismic acquisition and 3D seismic acquisition respectively, targeted at unveiling the petroleum potential in the deepwater setting. The exploration targets were deepwater channel related sand complexes and turbidite reservoir systems. The deepwater reservoir systems are believed to be associated with large hydrocarbon accumulation (Shanmugan 1992; Stow *et al*., 1999).The advent of deepwater exploration and production activity in the Niger Delta, was triggered by giant deepwater discoveries in the Gulf of Mexico and the Campos Basin of Brazil, from 1975 and 1984 respectively (Shanmugam, 2006). The deepwater Gulf of Mexico, Campos Basin in Brazil, and offshore West African constitute the "Golden triangle" petroleum exploration belt (Figure 5).

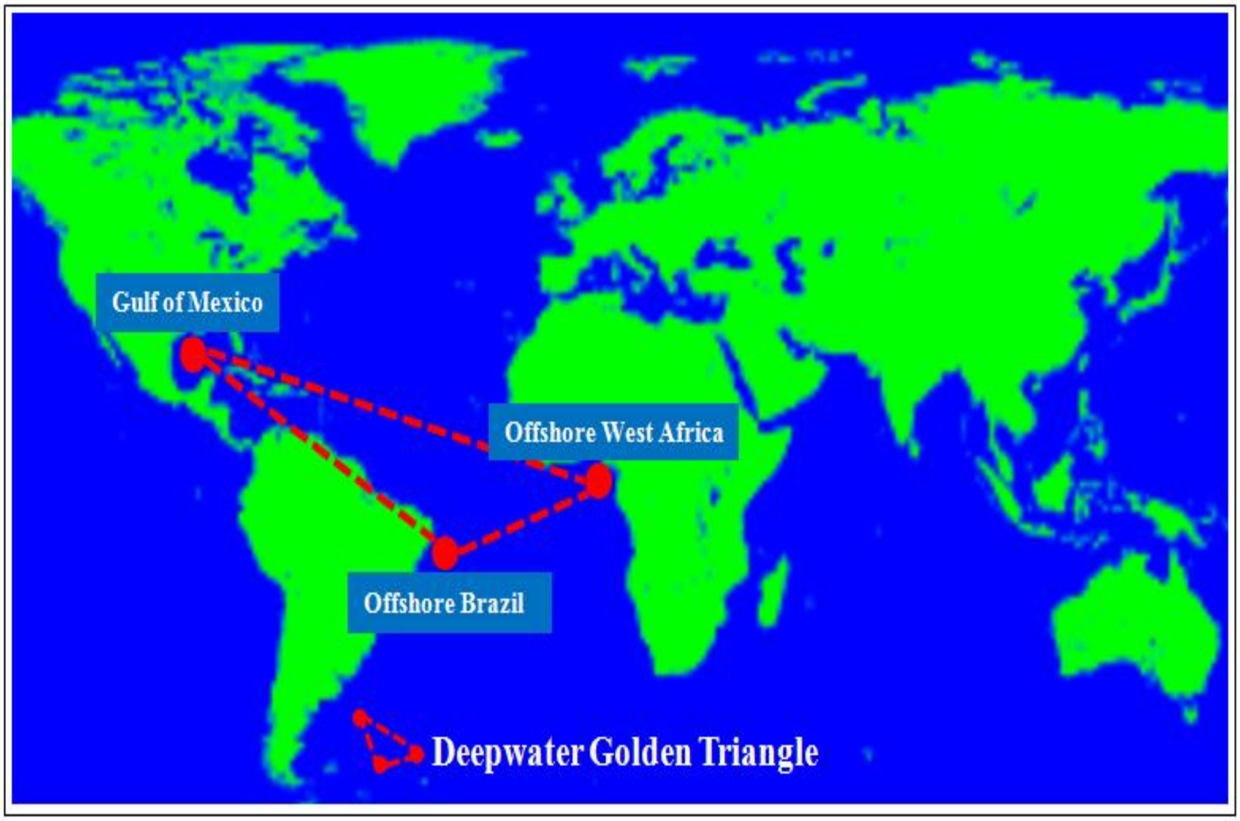

Figure 5: World map showing the deepwater Golden triangle (Adapted from Pettingill and Weimer, 2001)

Bonga Field was the first deepwater discovery in the Niger Delta in 1995, immediately after the Angola west African discovery in 1994. Later deepwater discoveries include: Agbami, Chota, Ngolo, Nnwa, Usan, Nsiko and Doro (Corredor *et al*., 2005; Biloti and Shaw, 2005). The Bonga discovery and some of the others consists of structural and combination traps in water depths greater than 500m (Table 2). Regrettably, several dry wells were also drilled in the same water depth during this period from 1995 to 2003. Consequently, most of the oil companies operating in the deepwater and ultra-deepwater acreages had to relinquish their blocks. Several factors were considered to be responsible for the failure cases: from structural traps integrity, source rocks maturity and timing, and reservoir presence. Failure rate was greater than 50% compared to success rate in the deepwater Niger Delta (Kostenko *et al*., 2008). Subsequently, there have been a decline in deepwater exploration activities since 2000.

Table 2 Some Niger Delta Deepwater Discoveries and their water depth

Field	Water Depth (m)	Year of Discovery	Recoverable Resources
Bonga	1125	1995	735MM bbl oil & 451 bcf gas
Bosi	1424	1996	2.3 tcf gas
Agbami	1435	1998	780MM bbl oil & 576 bcf gas
Nwa-Doro	1283	1999	4.4 tcf gas
Bonga SW	1245	2001	500 MM bbl oil & 500 bfc

2.9 Theoretical Concepts

The theoretical concepts for this study involved rock physics analysis, complex seismic trace and multi-attribute analysis, sedimentology, variogram and mulitiple-point geostatistics.

2.9.1 Rock Physics

Based on the stress-strain relationship , quartz-rich wet sand, oil sand, gas sand, and clay-rich shale will deform differently and therefore characterised by distinct rock physics responses (Avseth *et al*., 2005). Figure 6 is a schematic of siliciclastic rock deformation under normal stress, hydrostatic stress and shear stress respectively.

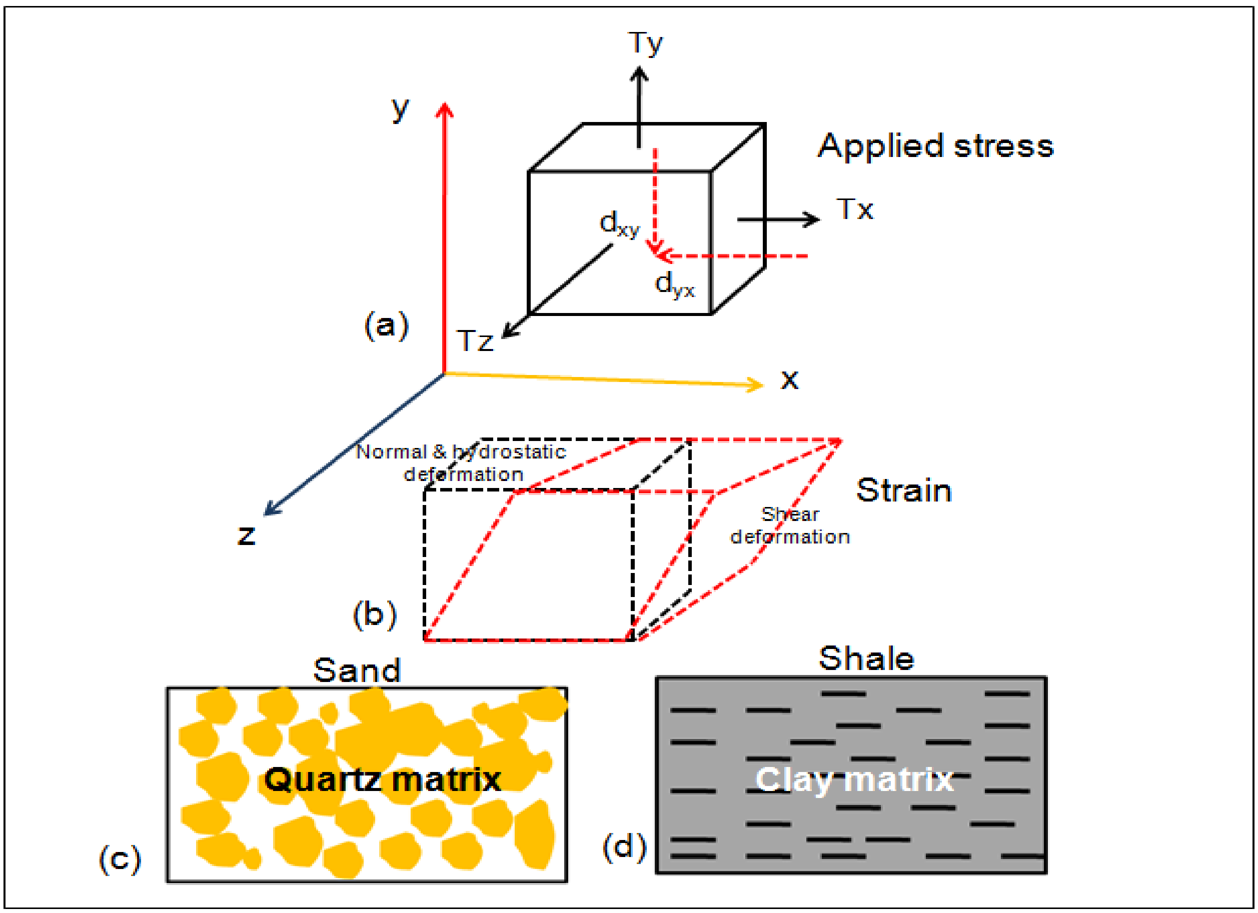

Figure 6: Schematic diagram of sandstone and shale deformation. Tx, Ty, and Tz represent normal stresses in the x, y, and z coordinate directions respectively. While d_{xy} and d_{yx} represents shear stresses tangential to x and y directions respectively.

The basic rock physics parameters and their derivative rock physics attributes, can be expressed by the result of the three dimensional tensor relationship between stress and strain as shown in equations 1a to 1e.

$$T_{ij} = \lambda\delta_{ij}\alpha_{kk} + 2\mu\alpha_{ij} \tag{1a}$$

$$T_{ij} = \mu\alpha_{ij} \tag{1b}$$

$$Vp = \sqrt{\frac{\lambda + 2\mu}{\rho}} \tag{1c}$$

$$Vp = \sqrt{\frac{k + \frac{4\mu}{3}}{\rho}} \tag{1d}$$

$$Vs = \sqrt{\frac{\mu}{\rho}} \tag{1e}$$

where T_{ij} =Stress tensor, λ =Lame' first parameter, δ_{ij} =Kroneka delta, α_{kk} =volume strain, μ=second Lame's parameter or shear (rigidity) modulus, α_{ij} =Strain tensor, *k*=bulk modulus, ρ =density, *Vp*= compressional velocity, and *Vs*=shear velocity.

For *i*=*j*, equation 1a represents compressional wave equation, and for $i \neq j$ equation 1b represents shear wave equation. The various elastic rock properties are defined in appendix A.

2.9.2 Complex Seismic Trace Analysis

The concept of complex trace analysis involves the Hilbert transform of the real seismic signal into its imaginary signal (Robertson and Nogami, 1984). The transformation is mathematical and allows the seismic trace to be expressed as an analytical signal having both the real and imaginary components. Complex trace analysis decomposes the seismic signal into functions that discriminate between the original trace amplitude information, and angular frequency and phase information (Equations 2 to 6).

$$U(t) = x(t) + iy(t) \tag{2}$$

where

$U(t)$=Complex seismic trace
$x(t) = f$ (real seismic signal) and,
$iy(t) = g$ (imaginary seismic signal)

By expressing the seismic trace as an analytical trace, specific seismic properties of a complex function can be extracted from the original seismic signal. These seismic properties include instantaneous amplitude, frequency and phase; which together with their higher order derivatives, are effective in predicting lithology variation, depositional features, reservoir properties and fluid; otherwise masked by the original amplitude signal (Hart, 2008). Typical examples of complex seismic attributes include: envelope or reflection strength, root mean square (RMS) amplitude, instantaneous frequency, instantaneous phase, acoustic impedance, sweetness, quadrature amplitude, etc (Schultz *et al*., 1994). Generally, these attributes are expected to capture subtle changes in waveform that can be linked to physical properties of depositional systems. The mathematical formulation of the various instantaneous attributes, and higher order derivatives, as well as their physical significance are presented below:-

i**. Instantaneous amplitude (envelope)**

This is the total instantaneous energy of the analytical signal. It is independent of phase and can be used to detect bright spots, sequence boundaries and subtle changes in lithologies. Mathematically, it is represented by equation 3.

Envelope = $\sqrt{f^2 + g^2}$ (3)

where *f* and *g* are the real and imaginary seismic signals respectively.

ii. Instantaneous phase

This is related to events continuity, faults, pinch-out, dips, and seismic sequence boundaries. Mathematically, instantaneous phase is expressed as

phase, $\phi(t) = \tan^{-1}[\frac{x(t)}{y(t)}]$ (4)

iii. Instantaneous frequency

This is the derivative of phase, and can be used to estimate seismic attenuation. The instantaneous frequency is characterised by sharp reduction in oil and gas reservoirs. However, it is very unstable in the presence of noise. Mathematically, frequency is expressed as,

$\omega(t) = \frac{d\phi(t)}{dt}$ (5)

iv. Sweetness

This a measure of the overall energy signature changes in the seismic data. It is expressed mathematically as the ratio of envelope and instantaneous frequency. It can easily distinguish channels and stratigraphic features based on seismic facies contrast. Sweetness is very useful in the detection and prediction of sand-filled channels in shaly deepwater successions (Hart, 2008). Sand prone facies are characterised by high sweetness, while shale facies will give low sweetness values. Mathematically, sweetness is expressed as

$$Sweetness = \frac{\sqrt{f^2 + g^2}}{\sqrt{\omega(t)}} \tag{6}$$

v. RMS amplitude

This is defined as the square root of the average amplitude squares within a specific analysis window. It is very sensitive to extreme amplitude values, and therefore discriminate between sand and shale. Shale-prone intervals usually have low amplitude while isolated sand bodies in shale such as channel fills and frontal splays are characterised by high amplitude. Amplitude characteristic of seismic reflection have been found to be directly linked to grain size. According to Deptuk *et al*. (2003); Posamentier and Kolla (2003); high amplitude response correspond to coarse grained sediments. Most channel terrace and thalweg containing coarse grained turbidite deposits have been associated with high amplitude, while the inter-channel sections typical of fine grained turbidity current plume and hemipelagic sedimentation display low amplitude values (Heino and Davies, 2006). It is mathematically expressed as

$$a_{irms} = \sqrt{\frac{1}{N}\sum_{i=1}^{N} a_i{}^2} \tag{7}$$

where a_i = amplitude, rms = root mean square, and N = sample number.

vi. Reflection intensity

This is the average amplitude over a specified seismic window multiplied by the sampled interval. It can be represented mathematically by RI.

$$RI = (t_2 - t_1) * \sum_{i=1}^{N} a_i \tag{8}$$

where $(t_2 - t_1)$ =sampled interval, a_i=amplitude, and N=sample number.

2.9.3 Bayesian Probability

This defines the relationship between the posterior probability and prior probability (Maiti and Tiwani, 2010).

$$p(A \mid B) = \frac{p(A \cap B)}{p(B)} \tag{9}$$

$p(A \mid B) =$ represent the probability of A, given that B has occurred (i.e. the posterior probability of A). $p(A \cap B)$ represents the probability that both A and B will occur.

$p(B)$ represents the probability of event B.

In equation 13, $p(A \cap B)$ can be represented as

$$p(B \mid A) * p(A) \tag{10}$$

By substituting equation 10 in equation 9,

$$p(A \mid B) = \frac{p(B \mid A) * p(A)}{p(B)} \tag{11}$$

Where $p(B)$ is unknown, equation 11 can be expressed as

$$p(A \mid B) \; \alpha \; p(B \mid A) * p(A) \tag{12}$$

The above equation implies that the posterior probability of an event A is related to the prior probability of event A. Hence if the sample is comprised of n and mutually exclusive events A_i, then

$$\sum_{i=1}^{n} p(A_i \mid B) = 1 \tag{13}$$

By combining equations 12 and 13, the posterior probability can always be calculated. This concept of Bayesian probability is very useful in representing and quantifying the relationship between seismic attributes and any geological facies (Maiti and Tiwani, 2010). For each facies, specific seismic attributes are defined as continuous properties. Probability of a seismic attribute to take a particular value between 0 and 1 given a particular facies is expressed by equation 1.

$$p(S_i \mid k_j) \tag{14}$$

Where S_i =the value of seismic attribute (attribute class), K_j = seismic facies

In practice, the seismic attribute is divided into discrete seismic facies classes, and the probability of each seismic facies class representing a specific geologic facies is estimated. Hence, given a specific seismic attribute, the posterior probability of geological facies can be expressed with the Baye's rule in equation 15.

$$p(K_j \mid S_i) \; \alpha \; p(S_i \mid K_j) * p(K_j) \tag{15}$$

2.9.4 Variogram Estimation

This involves the use of weighted arithmetic averaging to estimate unknown values at unsampled locations. Variogram is a bivariate statistical measure of spatial relationship used in the estimation of unsampled variables. Mathematically, it is defined as half the variance of the difference between two variables separated by a given distance (Kelkar and Perez, 2002).

$$\gamma\left(\vec{L}\right) = \frac{1}{2}V\left[X\left(\vec{u}\right) - X\left(\vec{u} + \vec{L}\right)\right] \tag{16}$$

γ = variogram, $\vec{L}$ = distance between sampled variables, V = variance, $X\left(\vec{u}\right)$ and $X\left(\vec{u}+\vec{L}\right)$ are sampled values at locations separated by distance, $\vec{L}$.

Variogram is closely related to covariance. While variogram measures the variance between sampled data points, covariance measures the similarity between the sampled data points (Appendix B). At zero distance between sampled locations, the variogram is expected to be equal to zero.

This relationship between variogram and covariance is given by equation 17.

$$\gamma\left(\vec{L}\right) = C(0) - C\left(\vec{L}\right) \tag{17}$$

where $C(0)$=covariance at zero distance, and $C\left(\vec{L}\right)$=covariance at a given separation distance between sampled location.

In practice, the estimated variogram based on the sample data is expressed as the equation 18.

$$\hat{\gamma}\left(\vec{L}\right) = \frac{1}{2n\left(\vec{L}\right)} \sum_{i=1}^{n\left(\vec{L}\right)} \left[x\left(\vec{u}_i\right) - x\left(\vec{u}_i + \vec{L}\right) \right]^2 \tag{18}$$

where $n\vec{L}$ =number of pairs at lag distance $\vec{L}$; $x\left(\vec{u}_i\right)$ and $x\left(\vec{u}_i + \vec{L}\right)$ =data values for the i^th^ pair located $\vec{L}$ lag distance apart.

By rearranging equation 19,

$$C\left(\vec{L}\right) = C(0) - \gamma\left(\vec{L}\right) \tag{19}$$

The matrix equation of covariance can be written as

$$\begin{bmatrix} C\left(\vec{u}_1, \vec{u}_1\right) \ldots\ldots\ldots C\left(\vec{u}_1, \vec{u}_n\right) \\ C\left(\vec{u}_n, \vec{u}_1\right) \ldots\ldots\ldots C\left(\vec{u}_n, u_n\right) \end{bmatrix} \begin{pmatrix} \lambda_1 \\ \lambda_n \end{pmatrix} = \begin{bmatrix} C\left(\vec{u}_1, \vec{u}_0\right) \\ C\left(\vec{u}_n, \vec{u}_0\right) \end{bmatrix} \tag{20}$$

where $C\left(\vec{u}_1, \vec{u}_1\right) = C\left(\vec{u}_n, \vec{u}_n\right) = C(0) = 100$

The covariance matrix equation can also be expressed as equation 21.

$$|C||\Lambda| = |c| \tag{21}$$

hence, $|\Lambda| = |C|^{-1}|c|$ (22)

where $|C|$ =the covariance among the sample points, $|C|^{-1}$ =inverse of matrix $|C|$ and $|\Lambda|$ =vector of weights assigned to samples

By solving for λ_1 and λ_n as the weighting on sampled locations in equation 20, unknown values can be estimated using different kriging methods.

In principle kriging technique can be expressed as equation 23 to estimate values at unsampled locations.

$$X^*\left(\vec{u}_0\right) = \sum_{i=1}^{n} \lambda_i X\left(\vec{u}_i\right) \tag{23}$$

Equation 23 can be modified and expressed as equation 24.

$$X^*\left(\vec{u}_0\right) = \lambda_0 + \sum_{i=1}^{n} \lambda_i X\left(\vec{u}_i\right) \tag{24}$$

where $X^*\left(\vec{u}_0\right)$ = the estimated value at unsampled location, $\vec{u}_0$, $X\left(\vec{u}_i\right)$ = the value at the neighboring location, $\vec{u}_i$, λ_i =the weight assigned to the neighboring value, $\lambda_0 = m\left(1 - \sum_{i=1}^{n} \lambda_i\right)$, m=mean of sampled values.

All kriging algorithms are based on equations 23 and 24 with minor variations depending on specific applications. The weight assigned to the individual neighboring points is derived from the covariance matrix equation as a function of different variogram models such as Isotropic, Gaussian, spherical and exponential variogram models (Appendix B).

2.9.5 Object-based Modeling

This refer to a set of geostatistical simulation techniques used to describe geological bodies, facies and lithhofacies with objects of discrete geometry. According to Kelkar and Perez (2002), the geostatistical techniques used for object-based facies modeling involves defining probability functions for different object dimensions. Typical geologic shapes for object modeling include parallelepiped, wedge, ellipsoid, lobe, sigmoid, channel, and dune. The most commonly used object modeling technique for describing geologic bodies by discrete shapes in reservoir models is the marked point process. The marked point process involves the simulation of an empty volume over the reservoir area of interest or zone. With an initial assumption of background facies fill in the entire volume, distinct objects are randomly inserted into the volume to replace the background. The simulation process allows the objects to be first inserted at conditioning data locations to honor the presence of observed geologic facies at wells. Thereafter, the objects are inserted randomly within the reservoir volume until the target volume fractions are attained.

2.9.6 Single Normal Equation

The single normal simulation equation (snesim) was reviewed and adopted for inter-well property prediction in this study in order to overcome the inherent limitations in the use of variogram and object-based facies prediction methods. The snesim equation allows the use of seismic attribute as training image for inter-well multiple-point geostatistical facies prediction. The equation uses kriging probability to quantify the joint dependency between a random binary variable (A_k) and random variable events (S_u) describing facies classes (S_k) at grid locations (U_x).

According to and Meyer *et al*. (2001) and Strebelle (2002).

$$\lambda = \frac{Cov[A_k, B]}{Var[B]} \tag{25}$$

where λ=weight assigned to neighboring value, Cov=covariance, Var= variance, A_k= binary random variable (e.g. lithofacies and depositional facies), B=conditioning data event (binary random variable constituted by the n conditioning data e.g. discrete seismic facies).

$$B = \begin{cases} 1 & \text{if } S(u_\alpha)=s_\alpha,\ \alpha=1, \ldots, n \\ 0 & \text{if not} \end{cases}$$

A_k=1 if facies class k occur and is 0 elsewhere

Using equation 25, the following conditional probability is derived,

$$P(A_k=1|B=1)=E[A_k]+\lambda[E[B]] \tag{26}$$

where $E[A_k]$ and E[B] are the expected values of discrete random variable (X) and so,

$$E[X]=\sum_{i=1}^{n} x_i P[x=1] \tag{27}$$

E[X]= Expectation value (weighted average outcome of random variables),

$\boldsymbol{x}_i$= the outcome of the random variable X, $P[X=x_i]$ = probability mass function for the i^{th} outcome of n-number of possible outcome.

From equations 25 and 26, the Bayes' rule is defined in equations 28 to 30.

$$P(A_k=1|B=1)= E_k[A] + \frac{E[A_k B] - E[A_k]E[B]}{E[B]} \tag{28}$$

$$P(A_k=1|B=1)= \frac{P(A_k=1, B=1)}{P(B=1)} \tag{29}$$

$$P(A_k=1|B=1)= \frac{P(B \mid A_k=1)P(B=1)}{P(B=1)} \tag{30}$$

CHAPETER THREE

3.0 MATERIALS AND METHOD

3.1 Data Gathering

An integrated data set was used to address the objectives of this study. The data set consist of approximately 600 km^2 of processed 3D seismic data acquired by SAPETRO, Total and their Joint Venture partners in 2004 (Figure 7). Other data set include wireline logs for seven (7) wells and photographs of about 60 m footage of core from 2 wells. Table 3 shows the available suite of logs for the respective wells.

The seismic data was acquired using air gun energy source pressurized at 2500 psi with volume capacity of 3090 cubic inch and towed at water depth of 5 m. The seismic signal was sampled every 2 ms and recorded using a 10 streamer receiver system of 600 m length each at 37.5 m spacing. Inline and crossline spacing are 18.7 m and 12.5 m respectively, with 234 m^2 bin size and 160 subsurface fold coverage. The processed post stack 3D seismic data was suitable for the purpose of study.

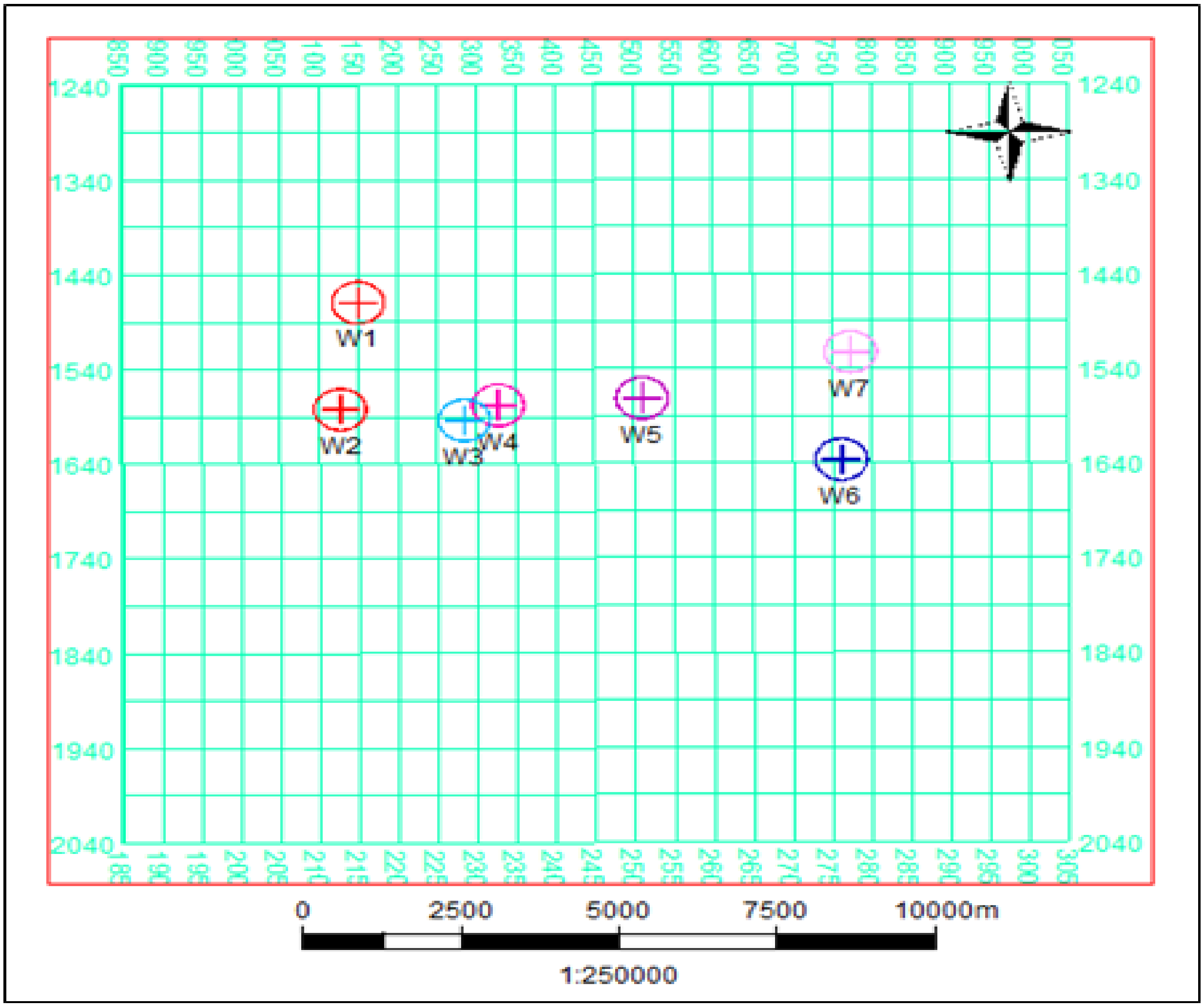

Figure 7: Base Map showing the 3D seismic coverage and Well locations for this study. The annotated symbols W1 to W6 represents well locations.

Table 3: Wireline Logs Suites

Well	Gama Ray	Caliper	Resistivity	Density	Neutron	PEF	Primary sonic	Shear sonic
W-1	✓	✓	✓	✓	✓	✓	✓	
W-2	✓	✓	✓	✓	✓	✓	✓	
W-3	✓	✓	✓	✓	✓	✓		
W-4	✓		✓	✓	✓	✓		
W-5	✓	✓	✓	✓	✓	✓	✓	✓
W-6	✓	✓	✓	✓	✓	✓	✓	
W-7	✓	✓	✓	✓	✓	✓		

3.2 Data Processing

3.2.1 Well Log and Rock Physics Analysis

Wireline logs including: gamma ray, deep resistivity, bulk density, neutron, photo electric factor (PEF), compressional sonic, and shear sonic, were qualitatively analyzed for lithology, pore fluid type, over-pressure, diagenetic changes and depositional facies (Rider, 1996). To ensure quality interpretation, the input logs were quality-checked and edited. Top and base of sand units were defined on the gamma ray log and attempt made to analyze similar log motif for depositional energy trend across the wells. The wireline logs were then quantitatively analyzed using standard petrophysical equations (Equations 31 to 36) and rock physics equations (Appendices A13 to A27). Shale volume (V_{shale}) was computed using the Larinov equation for unconsolidated Tertiary clastics (Equation 31).

$$V_{shale} = 0.08\left(2^{3.7 * I_{GR}} - 1\right) \tag{31}$$

$$I_{GR} = \frac{GR_{\log} - GR_{\min}}{GR_{\max} - GR_{\min}} \tag{32}$$

where I_{GR}=gamma ray index, GR_{log}=measured gamma ray log reading, GR_{min}=minimum gamma ray reading and GR_{max}=maximum gamma ray reading.

Also, porosity was calculated from density log using equation 33.

$$\rho_b = \rho_{ma}(1-\phi) + \phi\rho_f \tag{33}$$

where ρ_b =density reading from log, ρ_{ma} =density of mineral matrix, ρ_f =density of fluid, and ϕ =porosity. Elastic rock properties were estimated using standard rock physics equations and their derivatives (Appendices A13 to A27). Elastic rock properties, petrophysical and wireline log responses were then analyzed on cross plots using linear regression and cluster analysis. In order to qualitatively and quantitatively classify the distinct property trends and cluster patterns as discrete seismic lithofacies logs, polygon were digitized over distinct data clouds to serve as discrete facies filter.

The input logs for the computation of the elastic rock properties include primary sonic velocity, shear sonic velocity and density (Figure 8). However, the measured shear sonic velocity was only available for well W-5 in the study area. Hence, to estimate shear sonic velocity for the remaining six wells, an empirical equation (Benayol shear velocity equation) was derived for the study area. The empirical equations by Castagna *et al*. (1985); Han *et al*. (1986) and Castagna *et al*. (1993) were also used to estimate shear wave velocity in the study area for purpose of comparison.

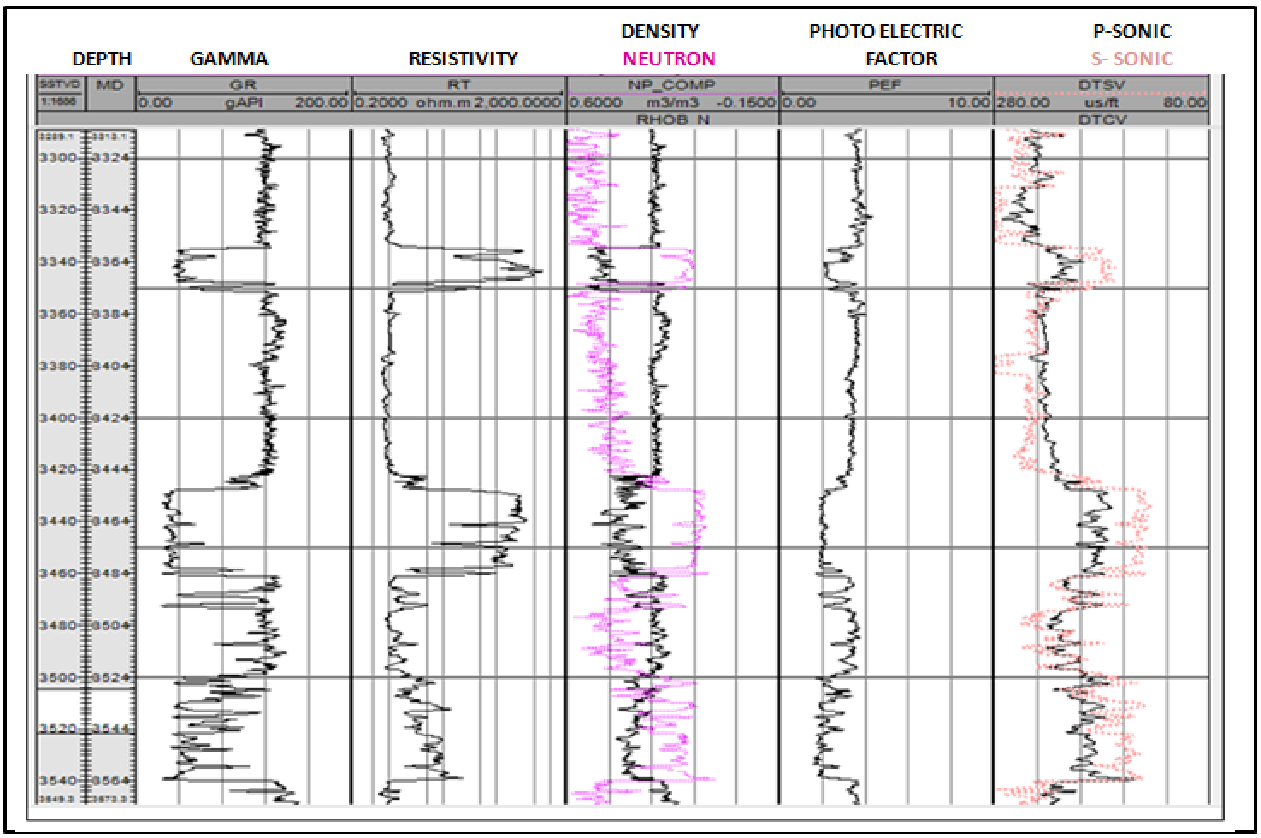

Figure 8: Reference well template showing the individual logs used for qualitative analysis of facies, petrophysical property estimation, and the computation of elastic rock physics properties.

3.2.2 Post-Stack Seismic Attributes Analysis

Different seismic attributes including: structural, stratigraphic, and instantaneous seismic attribute volumes were generated and used for multi-attribute analysis. The volume attributes were quantitatively calibrated and then screened in three dimension to reveal distinct seismic facies pattern.

3.2.2.1 Seismic Waveform and Spectral Analysis

Spectral analysis was done on the original seismic amplitude volume at different windows to determine the dominant frequency of the seismic data and tuning thickness using equation 34 (Widess, 1973). The dominant frequency was estimated by computing the reciprocal of the time difference between two successive seismic peaks or trough in seconds (Period).

$$V = f\lambda \tag{34}$$

where *V*=interval velocity, f =dominant frequency of seismic data, λ =seismic wavelength, and $\frac{\lambda}{4}$=tuning thickness (seismic resolvable limit) and $\frac{\lambda}{8}$=seismic detectable limit.

3.2.2.2 Synthetic Seismogram and Well-to-Seismic Correlation

Using density and sonic velocity logs, acoustic impedance was computed as a product of density and velocity, from which reflection coefficient was derived. By convolving the reflection coefficient with a basic wavelet extracted from the seismic volume, synthetic seismograph was generated from the reference well. Figure 9 shows the basic input logs, generated acoustic impedance log, reflection coefficient, synthetic seismogram and seismic trace.

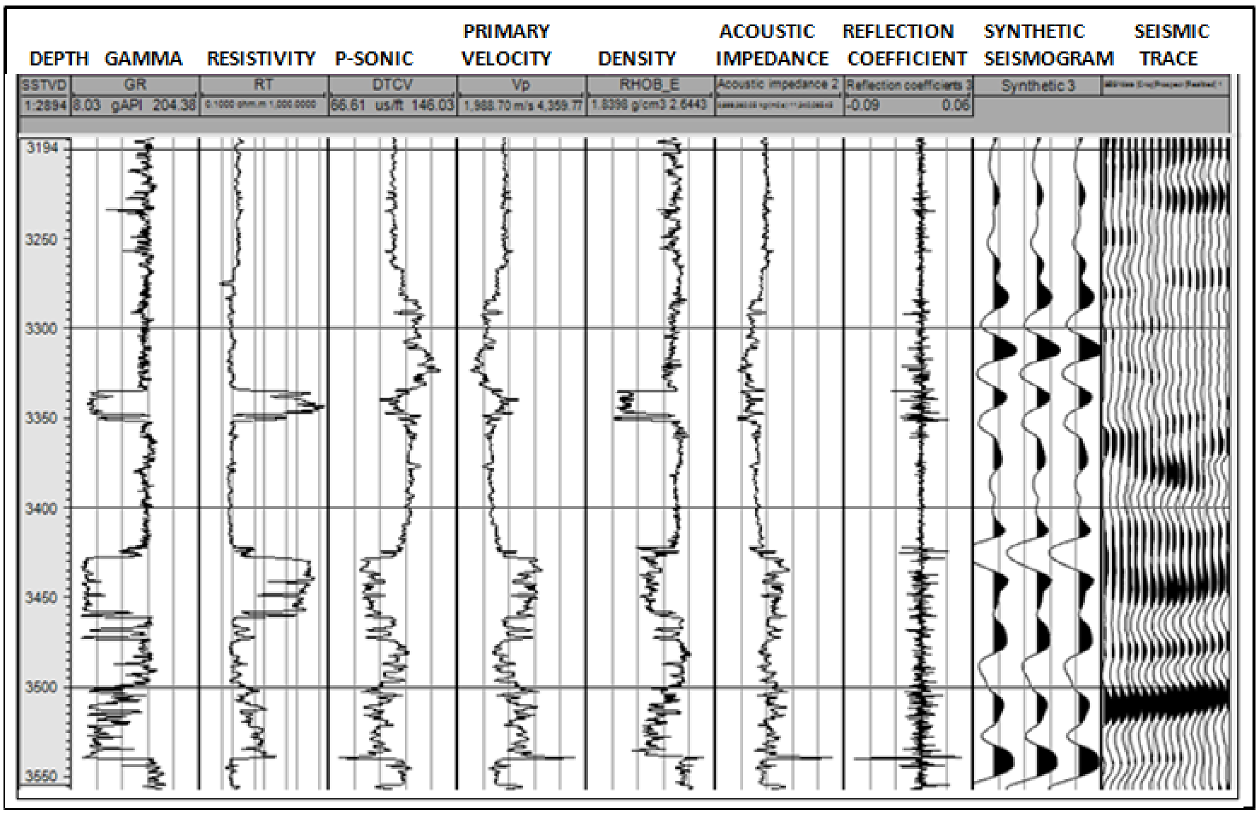

Figure 9: Well template showing the basic log inputs, generated acoustic impedance log, reflection coefficient, synthetic seismogram and seismic trace.

3.2.2.3 Seismo-structural and Stratigraphic Analysis

The seismic stratigraphic and structural analysis adopted for the study include the following steps below:-

i. Inlines, crossslines, and arbitrary lines, were analyzed across the 3D seismic volume using reflection termination, reflection configuration, frequency, and amplitude to identify stratigraphic elements on seismic. Also, time slices were screened for channel related morphological features.

ii. The sea bed and two proximal horizons were interpreted and mapped in time. Six other marker horizons were also interpreted and mapped for the reservoir zone of interest.

iii. 3D structural grids were constructed for the near surface and selected reservoir seismic windows respectively. The interpreted structure maps from seismic were used to construct 3D grid skeletons of 50 x 50 cell sizes. The structural maps and stratigraphic well tops were then combined with the 3D grid skeleton to define a geologic framework for property distribution.

iv. Seismic attribute volumes were generated and re-sampled into the 3D geologic framework for multi-attribute analysis. The attributes include variance attribute, RMS amplitude, reflection intensity, envelope, acoustic impedance, instantaneous frequency, quadrature amplitude, sweetness, etc.

v. A simple velocity model was used for depth conversion of the time structural maps and seismic attributes volumes. Using the time maps and well tops, a vertical velocity model was built for the zone of interest. Interval velocities from the wells were estimated by the simple interval velocity equation, $V=V_0=V_{int}$. The interval velocity values were interpolated by the convergent method in a 50 x 50 grid scale to generate constant interval velocity models for all the time surfaces. The V_0 represents a time depth relation (TDR) which was constant for each interval. The well TDR constant is equivalent to the calculated interval velocities between each of the time surfaces, computed from the checkshots and sonic derived average velocities. Figures 10 and 11 show typical seismic amplitude sections and RMS amplitude attribute sections respectively.

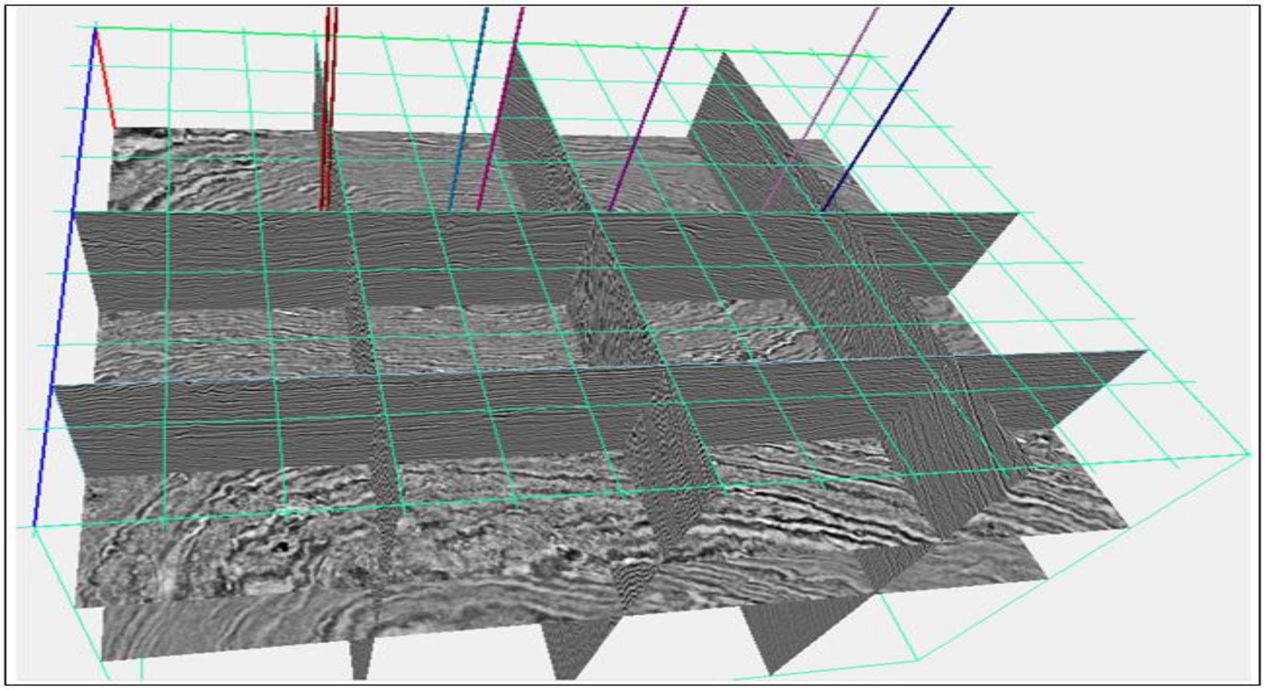

Figure 10: 3D seismic grid volume showing inlines, crosslines, time slices and vertical well trajectories.

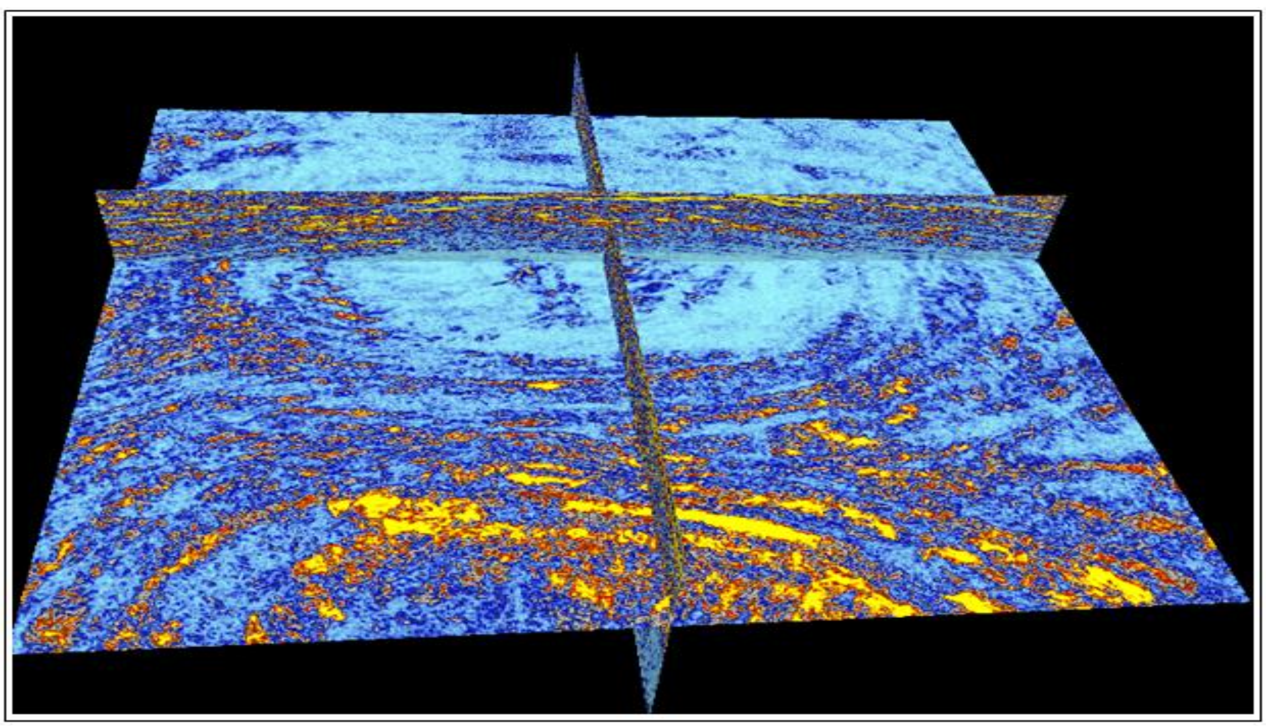

Figure 11: 3D grid showing typical seismic attribute (RMS amplitude)

3.2.2.4 Multi-attribute Analysis and Correlation

Several seismic attributes including complex trace attributes were re-sampled into constructed 3D grid cells and screened visually for diagnostic morphological patterns. The following steps were used for the multi-attribute analysis and correlation.

i. Synthetic seismic attribute logs were extracted from the attribute strata cubes and cross-plotted with derived elastic rock property logs.
ii. Seismic attributes having high correlation coefficients with elastic rock properties were identified.
iii. Using unsupervised classification and conditional probability rules shown in equations 25 to 30, discrete facies classes, seismic facies probabilities, and lithofacies probabilities were respectively defined from the re-sampled attribute volumes.

3.2.3 Core and Sedimentary Facies Analysis

3.2.3.1 Core Description and Depositional Facies Analysis

Core photographs of day light were described and analyzed for lithofacies variation, sedimentary structures, textural characteristics and depositional facies (Figures 12a, b and c). Observed grain size variation and sedimentary structures on core were integrated with gamma ray log motif and seismic architectural elements, to infer sedimentation mechanism, sedimentary facies. The observations were compared with sea bed and modern day depositional analogs to interpret sedimentation mechanism and facies architecture.

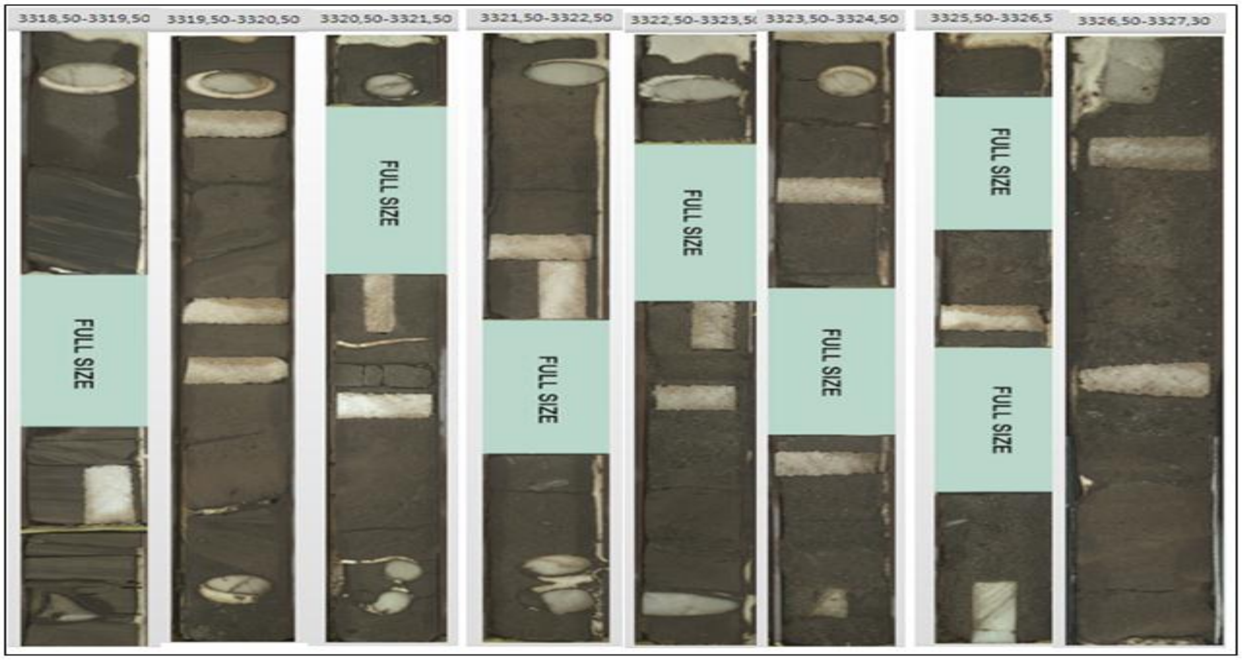

Figure 12a: Typical core photographs from 3318.50 m to 3327.30 m

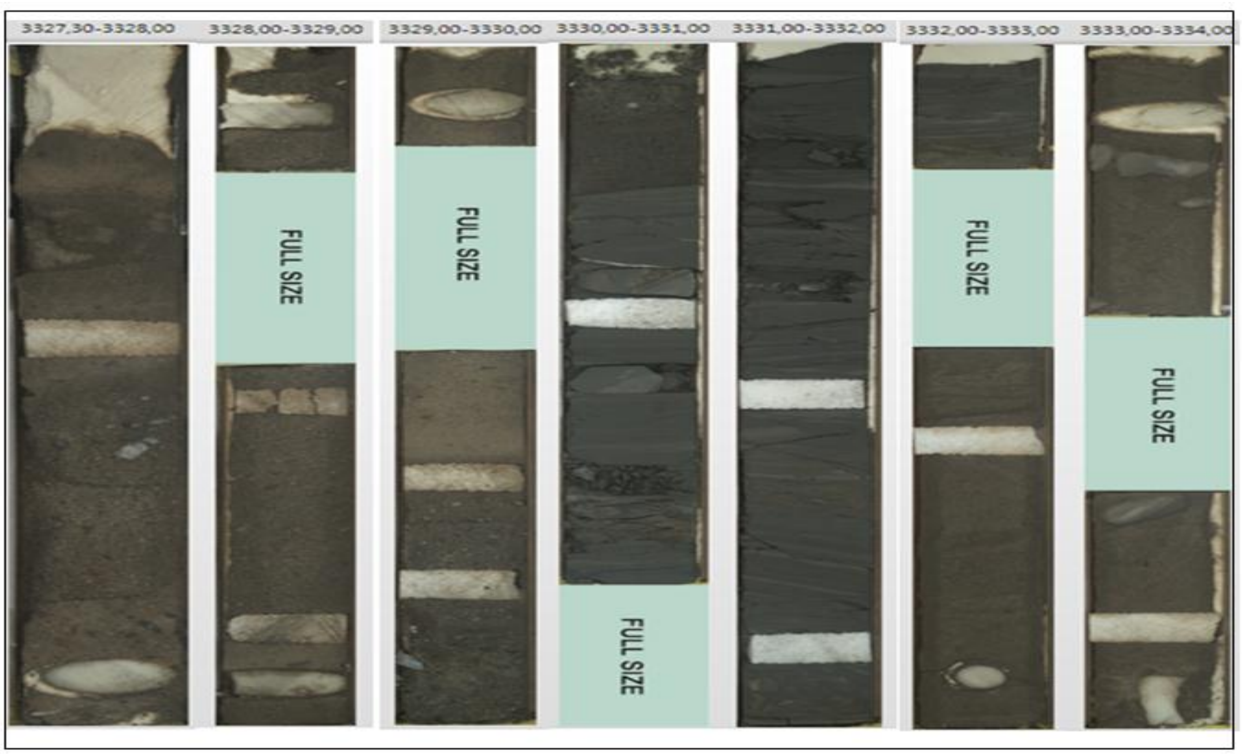

Figure 12b: Typical core photographs from 3327.30 m to 3334 m

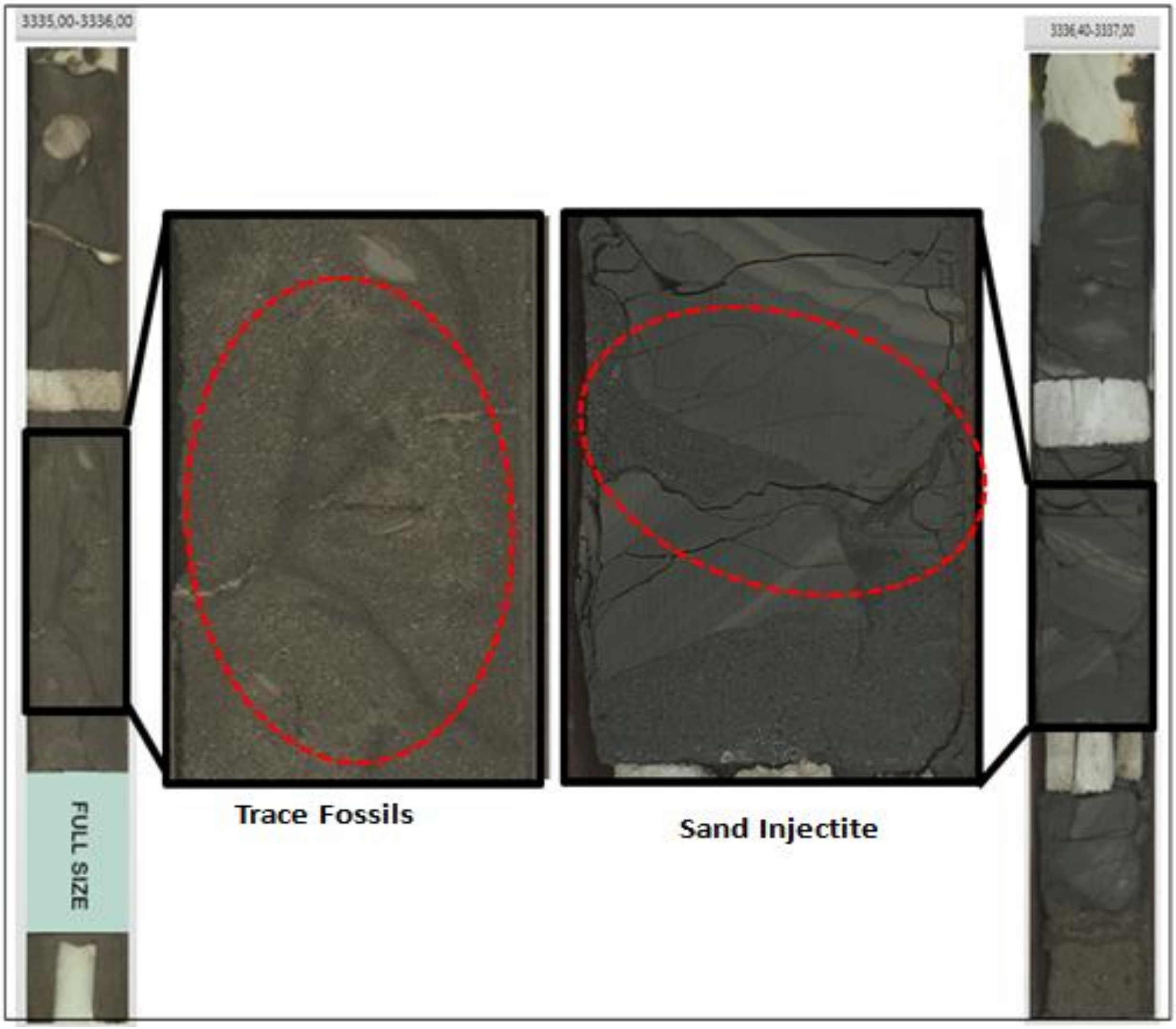

Figure 12c: Core photographs showing typical sedimentary structures

3.2.4 Geostatistical Facies Modeling

The following steps and methods were used for the geostatistical modeling of deepwater channel related sand bodies in the study area:-

i. Seismic lithologic facies and estimated petrophysical properties were upscaled into the geologic grid framework at all the grid cells intersected by the wells.

ii. Statistical histogram and facies proportion curve were used to quality-check the upscaled log properties based on different averaging methods.

iii. Data analysis using variogram modeling and transforms were used to capture and quantify the spatial relationship between sampled variables (Kelkar and Perez, 2002). As a rule of thumb, half the maximum distance between sampled variables were used as ranges to fit the model variogram to the experimental variogram in the major, minor and vertical direction. Indicator and normal score transforms were applied respectively to remove outliers from discrete facies and continuous petrophysical properties distribution respectively.

iv. Inter-well lithofacies modeling was carried out using different variogram estimation algorithms including: indicator kriging, SIS, and TGS techniques in five realization each (Kelkar and Perez, 2002).

v. Using object-based geostatistical algorithm, channel width, height, amplitude and wavelength were defined, and channel sand modeled from the sampled well locations across the reservoir interval in five realizations.

vi. Also, using the single normal equation (Meyer *et al.,* 2001), identified seismic attribute volumes were used as training image for multiple point geostatistical modeling of lithofacies. A weighted seismic probability function was integrated with the upscaled sand facies to derive sand probability volumes by modeling the probability trend.

vii. Finally, the sandstone lithofacies upscaled from the wells was combined with the sand probability grid, to predict lithofacies across the study area. Similarly, porosity and shale volume upscaled from the wells were biased to the lithfacies model using the sand probability as secondary property.

CHAPTER FOUR

4.0 RESULTS AND DISCUSSION

4.1 Qualitative Well Log Analysis

Qualitative analysis of the available suite of wireline logs shows two main lithological facies in the study area. The two main lithofacies are interpreted as sandstone and shale respectively. The logs which include: gamma ray log, deep resistivity log, neutron-density logs, photo electric factor (PEF), and sonic logs, reveal the sandstone facies to be hydrocarbon bearing. The hydrocarbon sands are characterised by low gamma ray, high resistivity, negative separation of neutron-density logs, low PEF and a narrow negative separation of the compressional and shear sonic readings, respectively. The high resistivity reading, large negative separation of the neutron-density readings, and negative separation of the compressional-shear sonic readings, indicate the presence of light hydrocarbon such as gas and gas condensate. However, the average bulk density reading in the sand intervals is about 2.0 g/cc. The PEF reading indicates the gross mineral composition of the sandstone and shale units. Low PEF correspond to low atomic weight minerals such as quartz which forms the main constituent of sandstones, while high PEF indicates relatively high atomic weight minerals such as the clay minerals predominant in shale. The compressional-shear sonic interval transit time shows a gradual decrease with depth, which is indicative of burial compaction. However, the sonic log pair show positive separation in shale, which track closer with depth. The effect of compaction on the shale intervals, is more significant than in the sandstone sections. Relatively, the compressional sonic log reads lower interval transit time in the sandstone than in the shale sections. This corresponds to a higher primary wave velocity in sandstone than shale. The results of the qualitative log analysis are shown in Figure 13. Also, gamma ray log interpretation of sandstone and shale units across the field is shown in Figure 14. The sand units generally display cylindrical and bell shape gamma ray log motifs with characteristic sharp base.

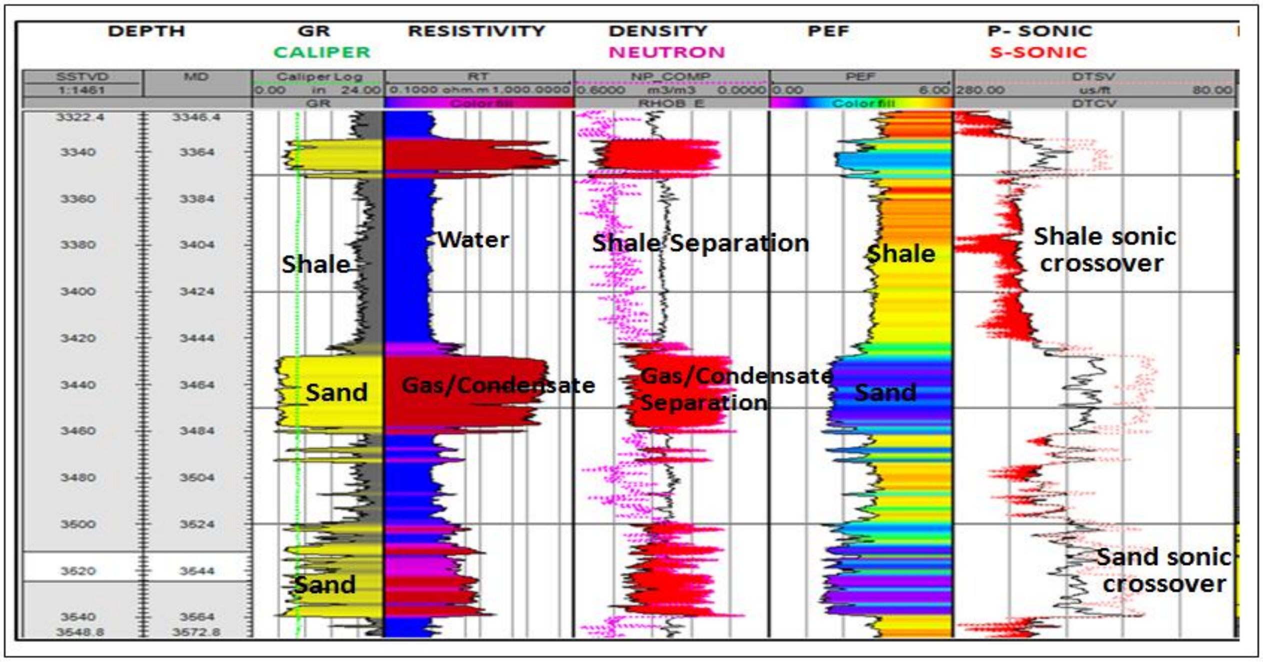

Figure 13: Well log analysis template

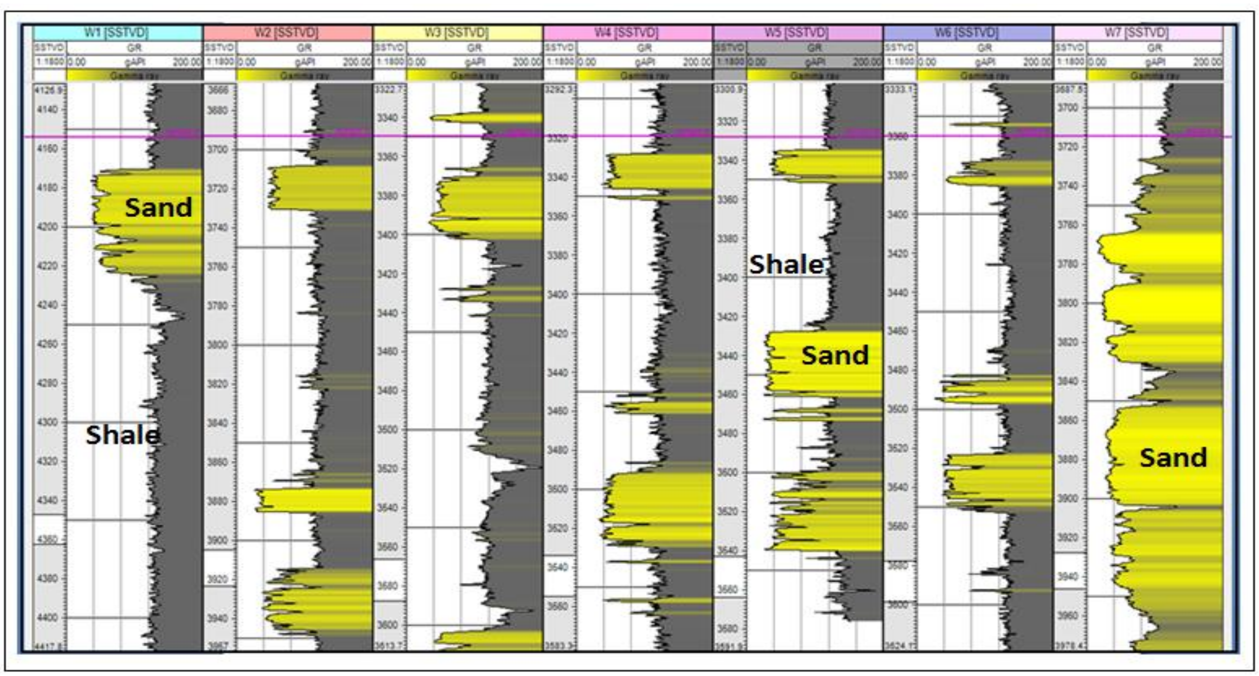

Figure 14: Well log sand correlation template

4.2 Petrophysical Estimation Results

Petrophysical interpretation of the available logs indicates quality reservoir sandstone units with shale volume generally less than 20%, and porosity averages of 32%, 24%, and 21%, respectively for the interpreted sand units shown on the shale volume, porosity and lithologic column respectively (Figure 15).

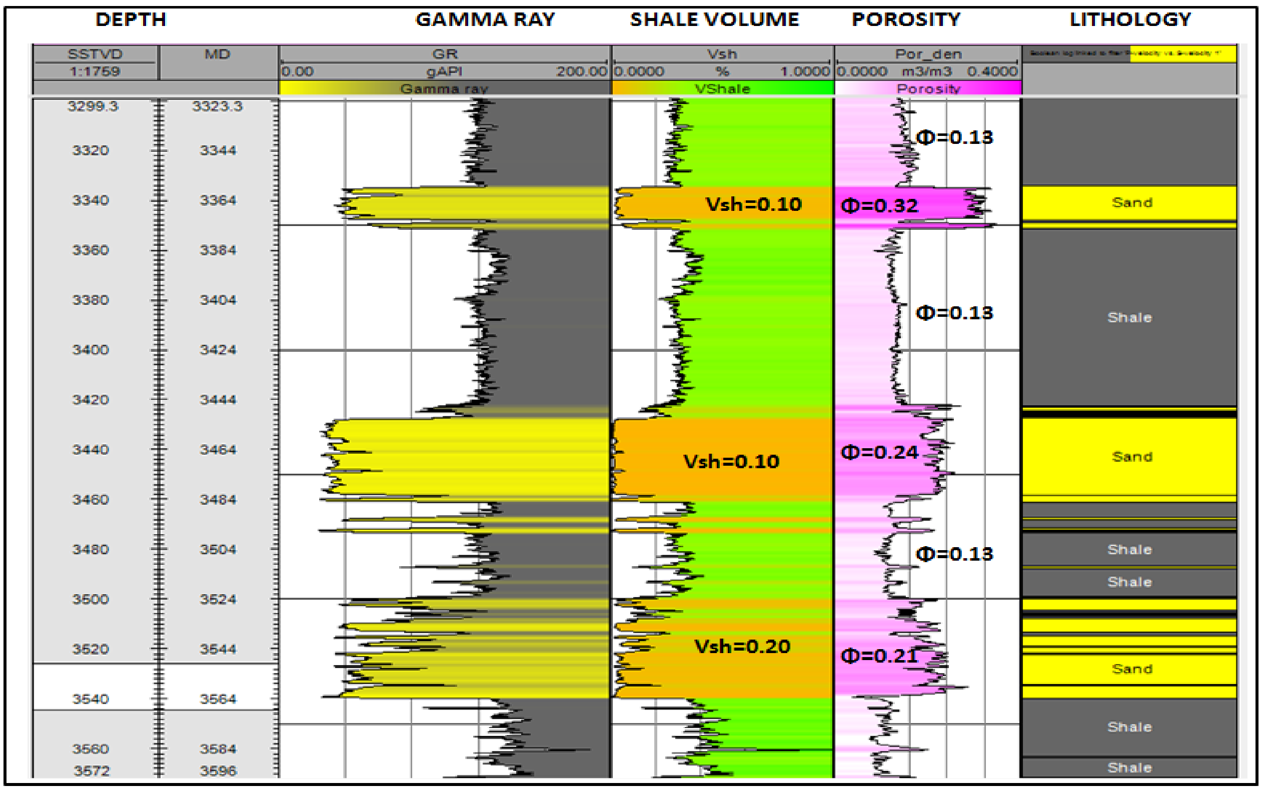

Figure 15: Petrophysical log template showing shale volume and porosity

4.3 Rock Physics Estimation Results

4.3.1 Shear Wave Velocity and Elastic Rock Property

The cross plot for the derivation of the empirical Benayol shear wave velocity equation ($V_s = 0.919V_p - 1.140$ km/s) in the study area is shown in Figure 16. This equation gives a better shear wave velocity estimate with uncertainty of between -13 m/s and +80 m/s. Table 4 and Figure 17 show the comparison between the measured and estimated shear wave velocities using Castagna *et al*.(1985), Han *et al.*(1986), Castagna *et al*.(1993) and the Benayol shear wave velocity equations respectively. Mathematical derivation of compressional wave sonic velocity, shear wave sonic velocity and density gives the resultant elastic rock properties including: shear impedance (SI), bulk modulus (K), Young's modulus (E), compressional-shear wave velocity ratio (Vp/Vs), Poisson's ratio (δ), mu-rho (μρ), lambda-rho(ʎρ) and closure stress scalar (css) as shown in Figure 18.

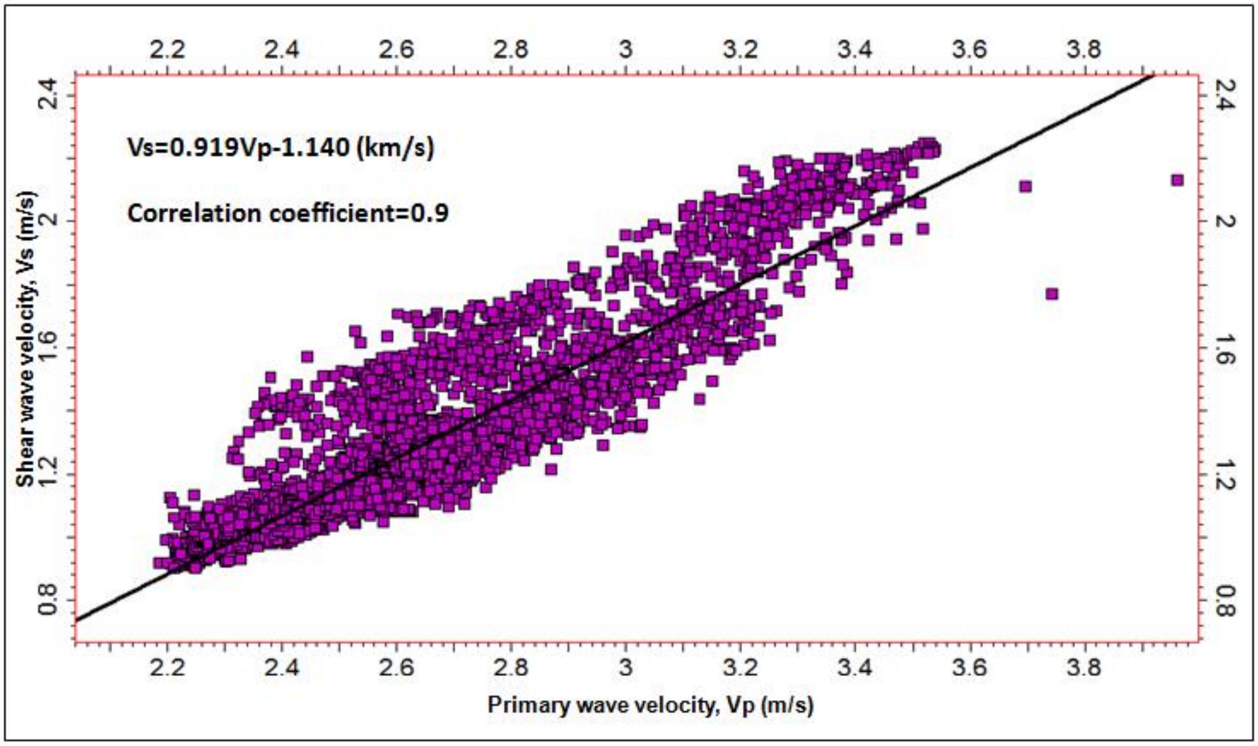

Figure 16: Primary wave velocity versus shear wave velocity plot and correlation

Table 4: Empirically derived shear wave velocities

Depth (m)	**Measured Shear Velocity (m/s)**	**Empirically Derived Shear Velocities**			
		Castagna *et al.*, 1985 (m/s) **V*s*=0.862V*p*-1.172**	**Han *et al.*, 1986 (m/s)** **V*s*=0.794V*p*-0.787**	**Castagna *et al.*, 1993 (m/s)** **V*s*=0.804V*p*-0.856**	**Benayol Equation (m/s)** **V*s*=0.919V*p*-1.140**
3308	***1474***	404	592	566	1504
3412	***1452***	426	614	588	1386
3455	***1867***	1084	1320	1291	1950
3506	***1538***	478	688	659	1504
3532	***1639***	823	1033	1004	1616
3576	***1505***	488	683	656	1488

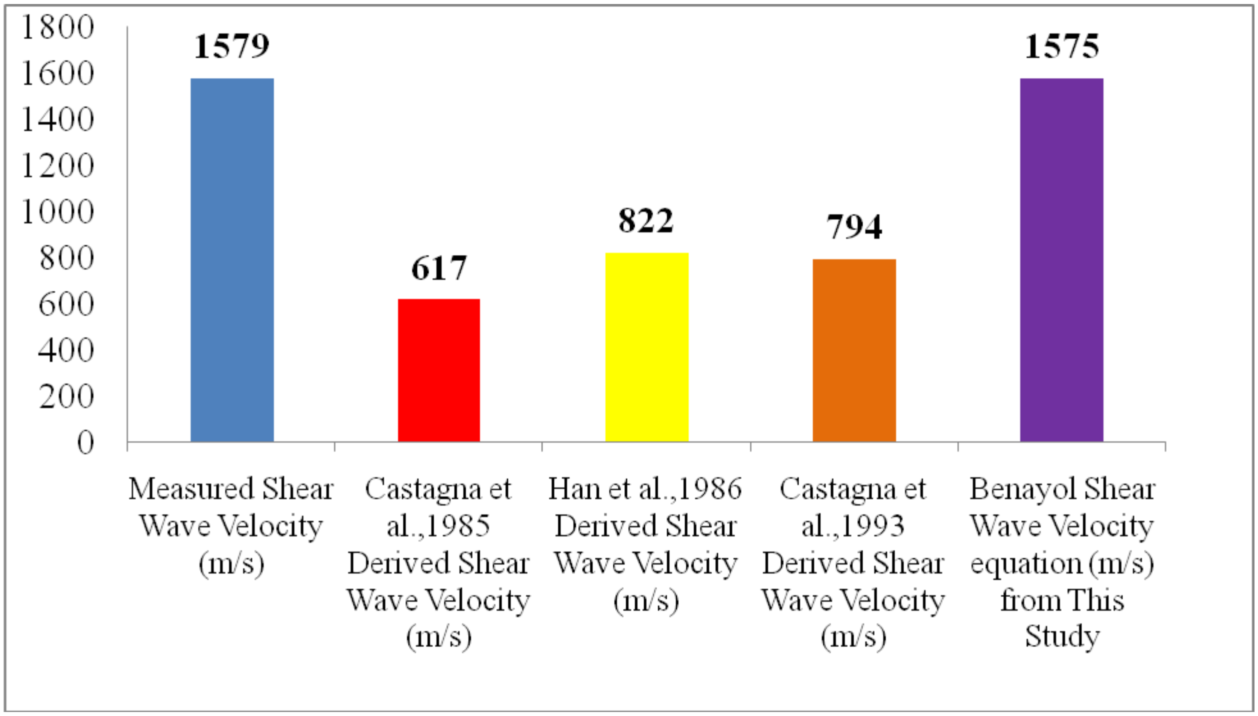

Figure 17: Measured and Empirical Shear Wave velocity averages

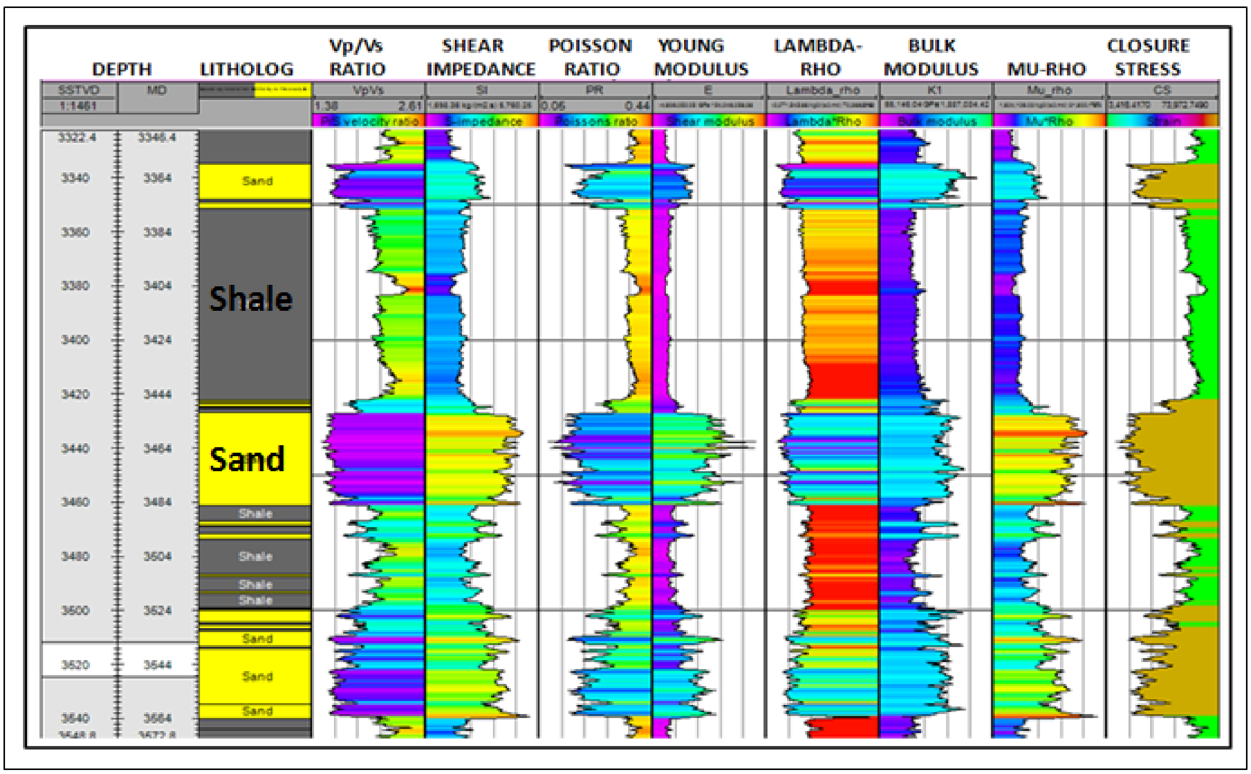

Figure 18: Lithofacies and elastic rock property logs

4.3.2 Rock Physics Cross Plots and Cluster Analysis

Cluster analysis of elastic rock properties, reservoir properties and petrophysical properties show distinct trend and data cloud on cross-plots (Figures 19 to 23). These trends and data clouds represent distinct lithofacies units defined by characteristic elastic rock physics properties. These lithofacies units are referred to as seismic lithofacies. In Figures 19 and 20 low Vp/Vs ratio and low lambda-rho generally correspond to low gamma ray reading, high porosity, and high mu-rho attributes. The data cloud defined by the pink ellipse in Figure 21 classified as seismic lithfacies-1 represents mudstone and shale. While the data cloud defined by the red ellipse in Figure 21 is classified as seismic lithofacies-2. The seismic lithofacies-2 is indicative of sandstone with high stiffness, high porosity, and hence it has relatively higher Mu-rho which is a measure of gross rock rigidity. The seismic lithofacies-1 is characterised by lower Mu-rho, higher Vp/Vs and Lambda-rho values. In Figure 22, acoustic impedance does not discriminate between shale and sand defined as seismic lithofacies-1 and seismic lithofacies-2 respectively. There is an overlap in acoustic impedance values between the two seismic lithofacies interpreted from the study.

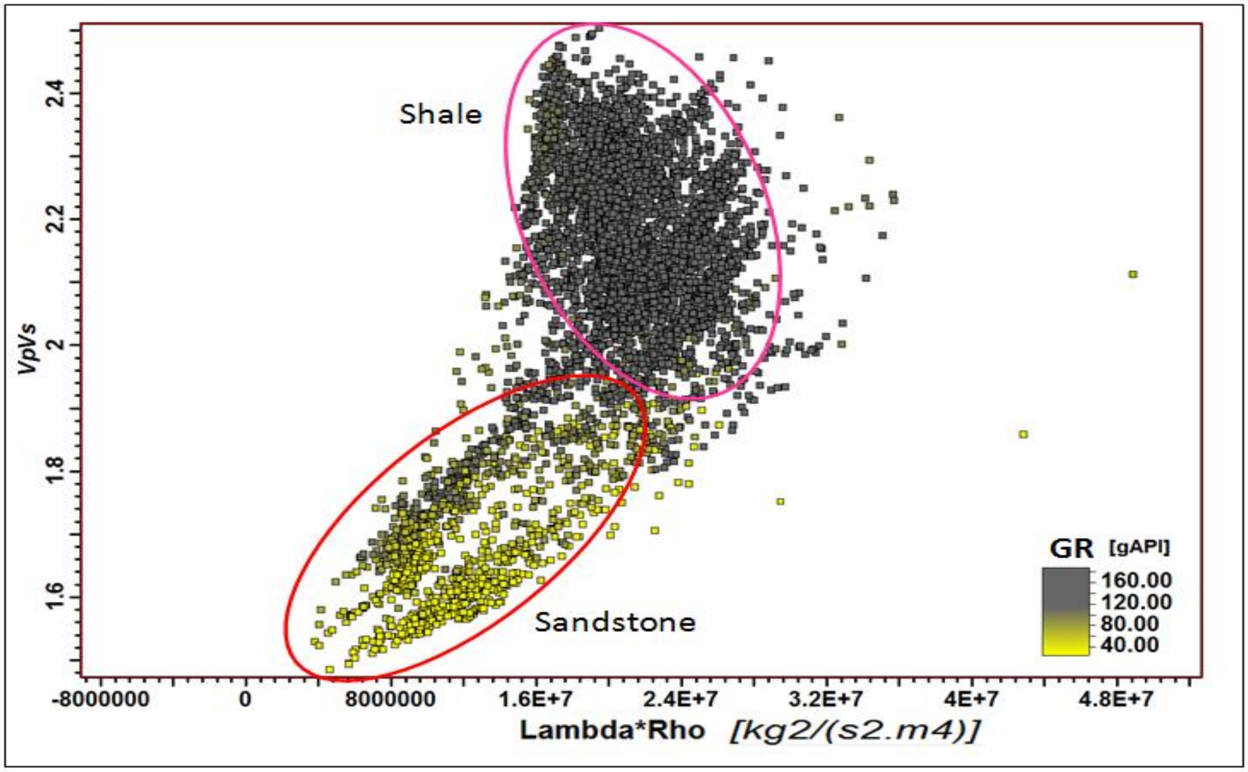

Figure 19: Lambda-Rho-Vp/Vs-Gamma Ray Cross Plot

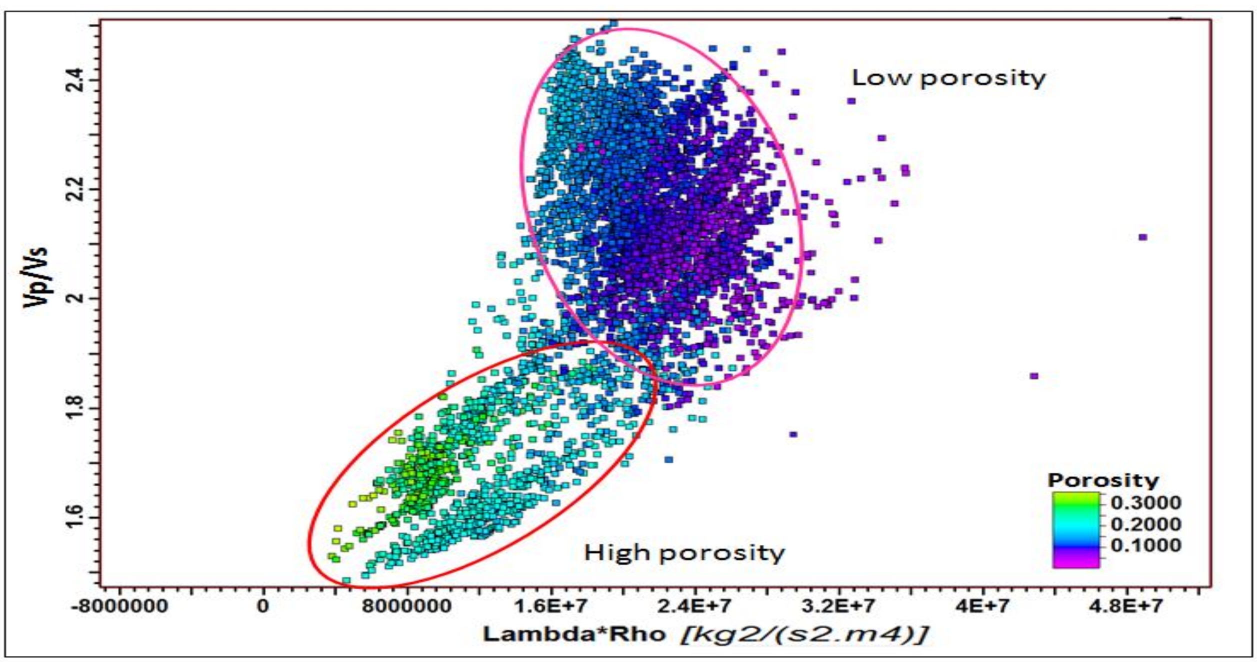

Figure 20: Lambda-Rho-Vp/Vs-Porosity Cross Plot

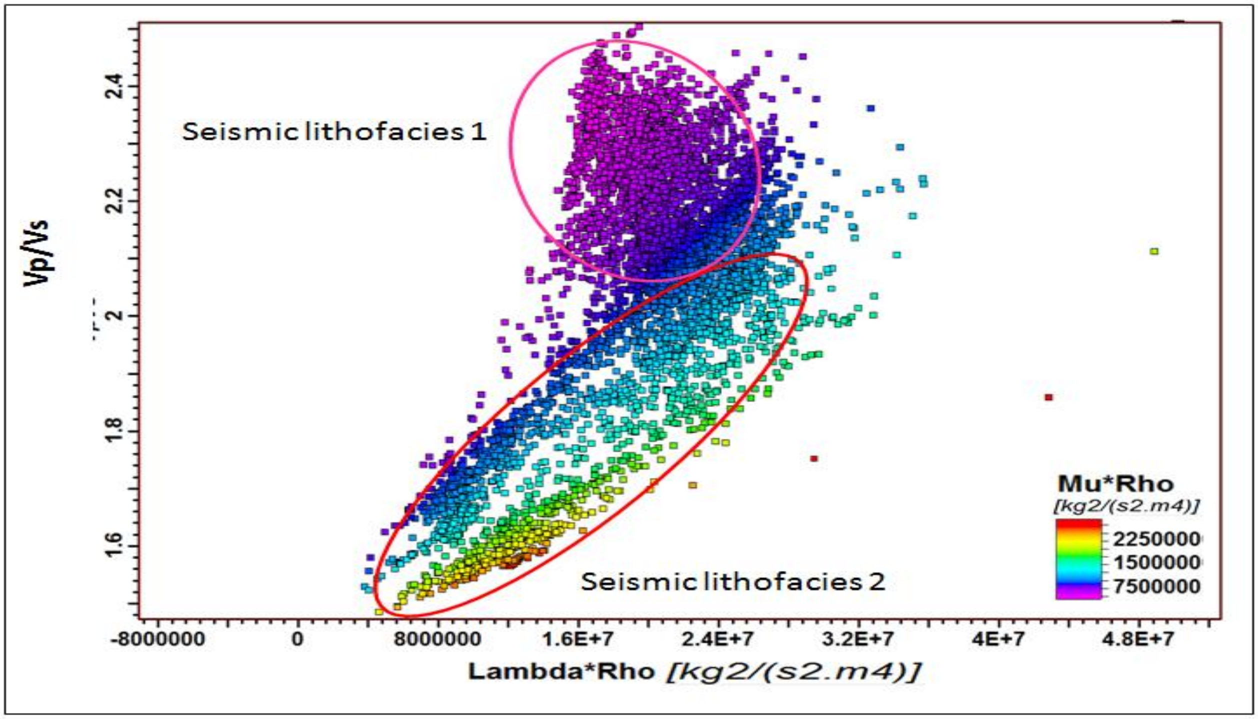

Figure 21: Lambda-Rho-Vp/Vs-Mu-Rho Cross Plot

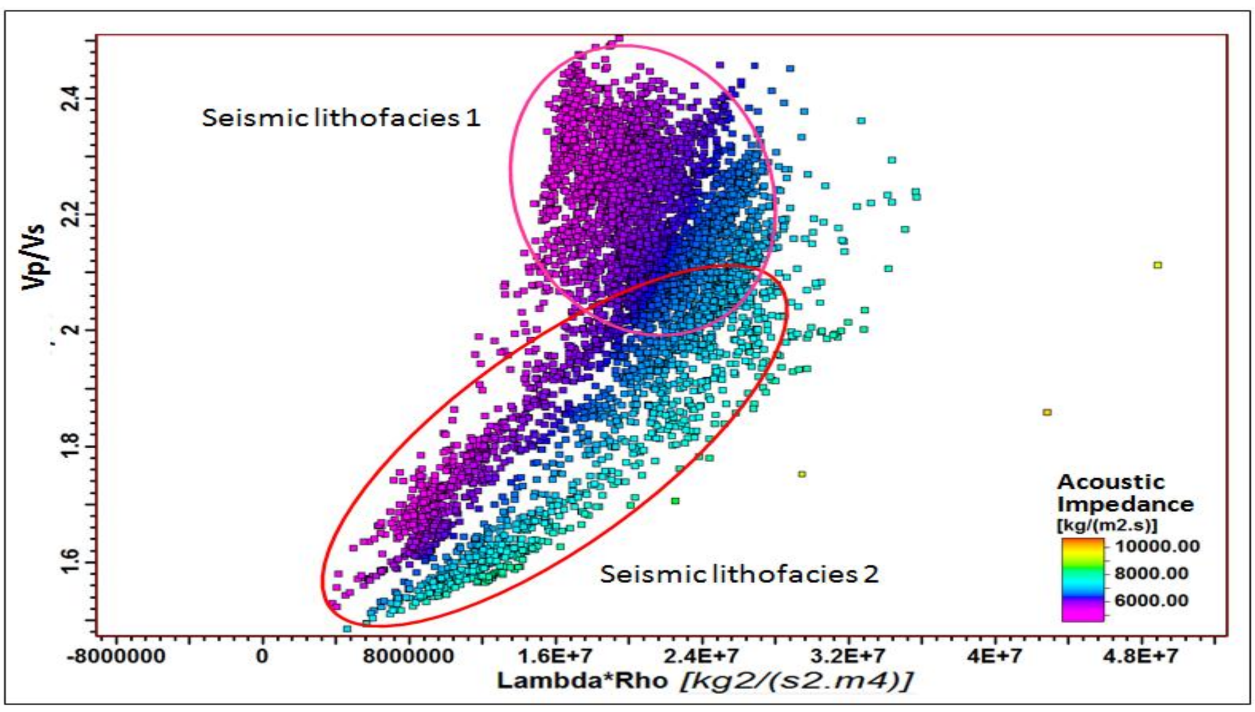

Figure 22: Lambda-Rho-Vp/Vs-Acoustic Impedance Cross Plot

Mu-rho, lambda-rho, Poisson's ratio and closure stress scalar are found to be related to lithology, porosity, pore pressure variation, stiffness and mechanical strength of siliciclastic rock units as shown in Figures 23 to 25. Shale related seismic lithofacies cluster in the lambda-mu-rho rock physics space, corresponds to relatively lower mu-rho, higher closure stress scalar and Poisson's ratio. This is indicative of low stiffness and possible over-pressure in the shale. In contrast, the sandstone lithofacies is characterised by relatively higher mu-rho, lower Poisson's ratio and lower close stress scalar. This implies high rock stiffness and relatively lower rock compressibility.

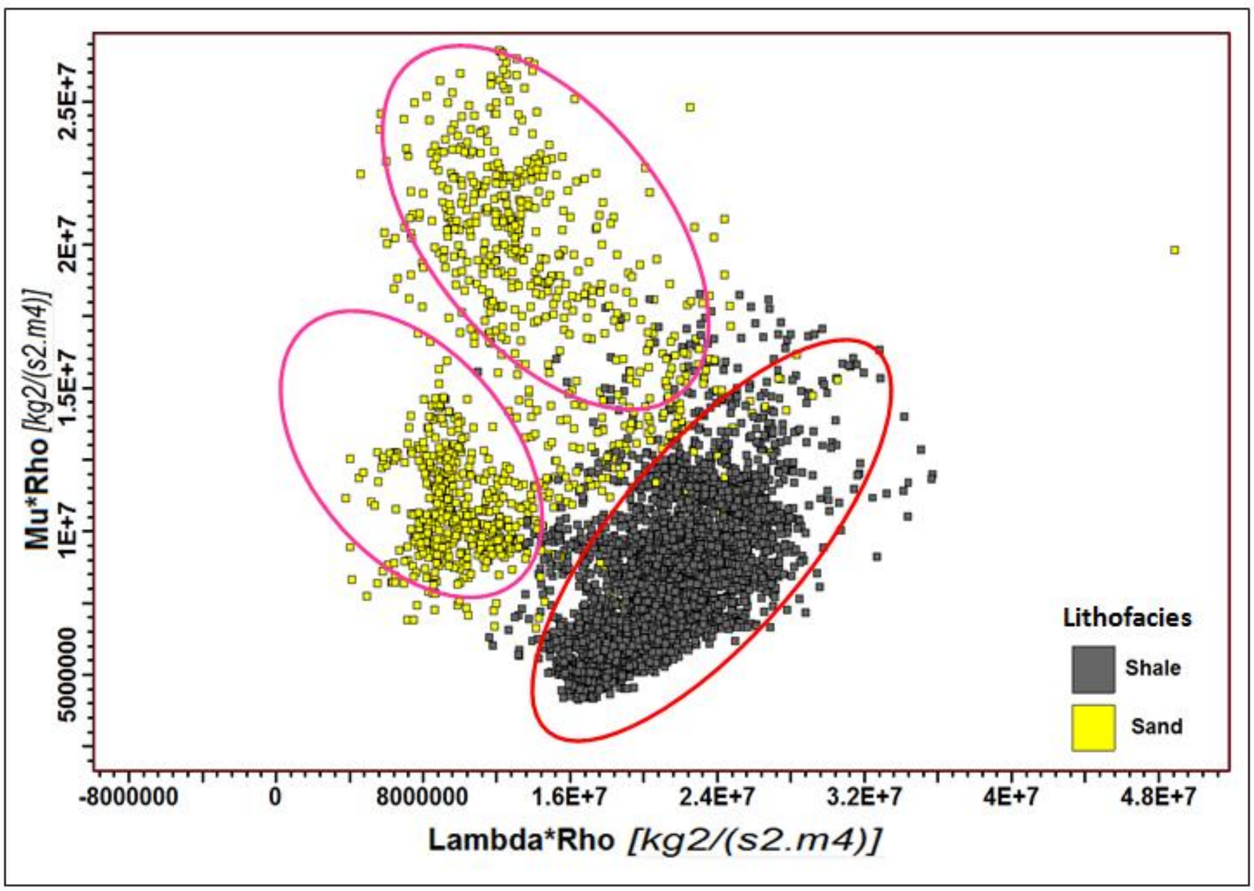

Figure 23: Lambda-Rho-Mu-Rho-Lithofacies Cross Plot

In Figures 24 to 26, there is a direct relationship between Lambda-rho versus Poisson's ratio trend, closure stress scalar, porosity and lithology contrast. The shale units are characterised by relatively high Poisson's ratio and closure stress scalar. The average porosity within the shale is as high as 0.20, which implies under-compaction and possible overpressure. There is an intrinsic overlap of compressional wave velocity between sand and shale in the primary velocity versus porosity and close stress scalar cross plot (Figure 25). However, the closure stress scalar remains anomalously low in the sand cluster and high in the shale cluster. The estimated sandstone porosity ranges between 0.20 and 0.36. Shale units have porosity ranging from 0.05 to 0.20. High Poisson's ratio, high closure stress scalar, relatively low mu-rho and high lambda-rho are indicative of less competent shale lithofacies in the study area, while the reverse is indicative of competent sandstone lithofacies (Figures 24 and 25).

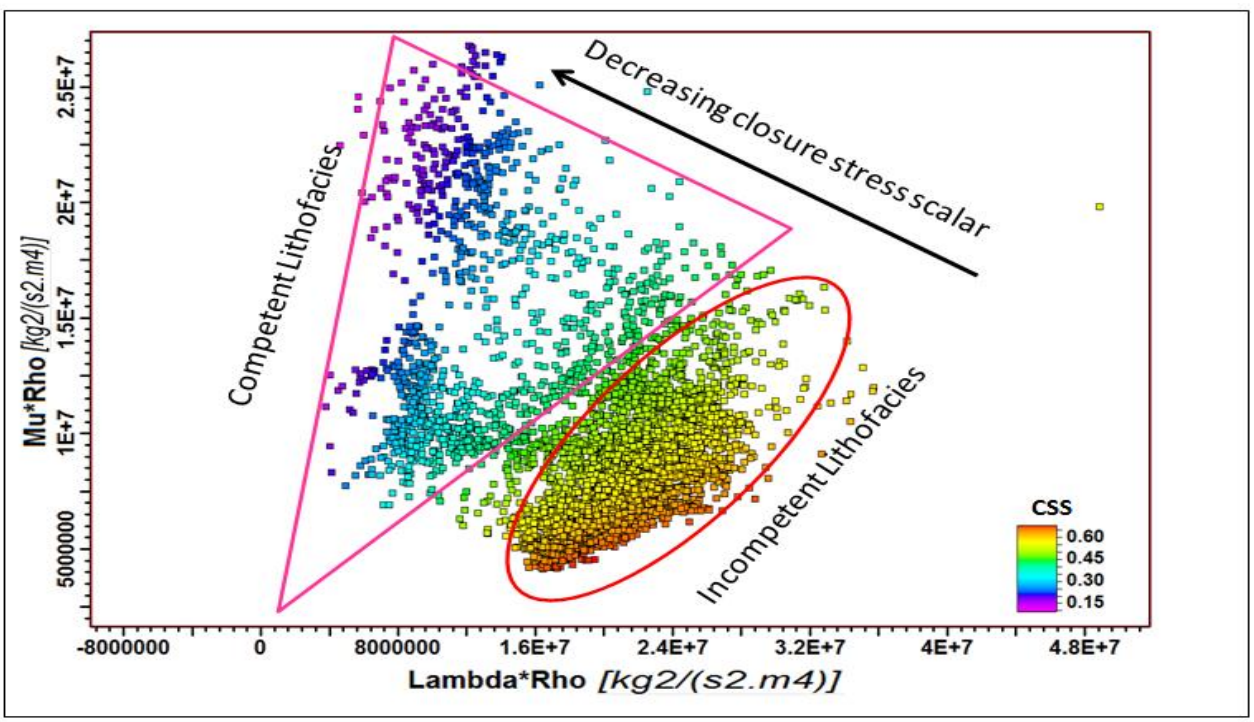

Figure 24: Lambda-Rho-Mu-Rho-Closure stress Scalar (CSS) Cross Plot

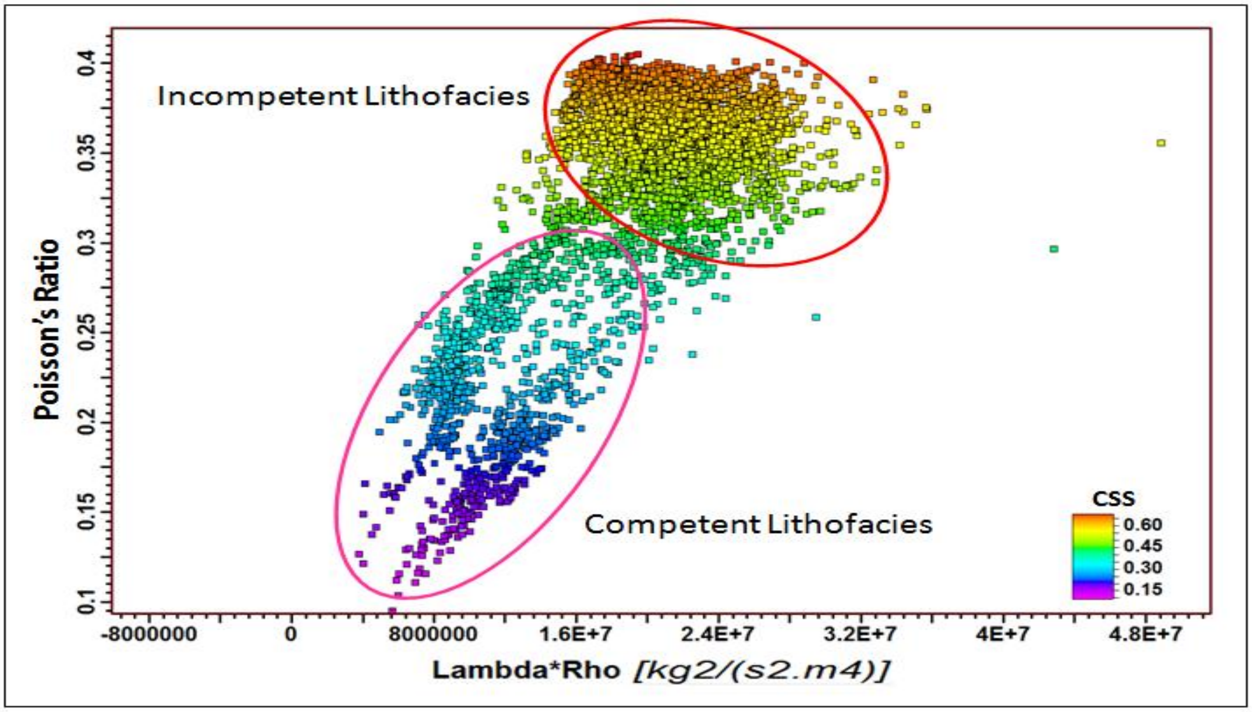

Figure 25: Lambda-Rho-Poisson's Ratio-Closure Stress Scalar (CSS) Cross Plot

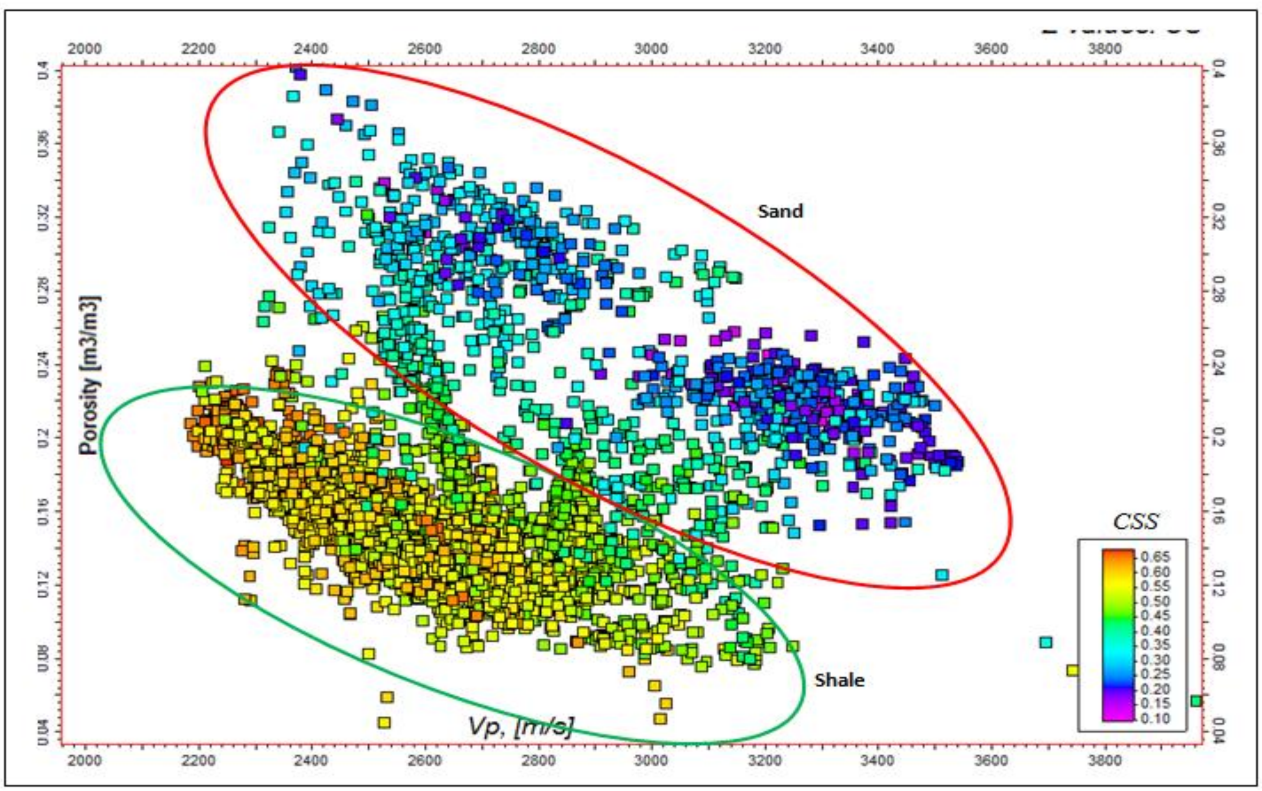

Figure 26: Primary Wave velocity-Porosity-Closure Stress Scalar (CSS) Cross Plot

4.4 Post-Stack Seismic Attribute Data

4.4.1 Seismic Waveform and Spectral Analysis

Seismic waveform and spectral analyses on the seismic data volume between 2.6 and 4.0 seconds time window, reveal the dominant frequency of the seismic as 50 hertz (Figure 27). Using an interval velocity of 3500 m/s estimated from well sonic interval transit time, the dominant wavelength and tuning thickness are given as 70 m and 17.5 m respectively. This implies that a homogeneous sand body less than 17.5 m in thickness will not be resolved fully on the seismic data. However, sandstone units with thickness greater than 9 m can still be detected through seismic attribute analysis. The spectral analysis and tuning thickness give insight to the minimum bed thickness that will be detected on seismic at specific window.

4.4.2 Well Synthetic Versus Seismic Trace Correlation

The synthetic seismogram and surface seismic tracks show good correlation between seismic events for the thicker sand units at depths 3430 m and 3488 m, having gross thickness of 34 m and 45 m respectively (Figure 28). The shallower sand unit at 3332 m with a thickness of 14 m shows very poor synthetic correlation and well-to-seismic tie. The lack of synthetic to seismic correlation observed in the 14 m thick sand can be attributed to destructive interference between the top and base of the thin bed.

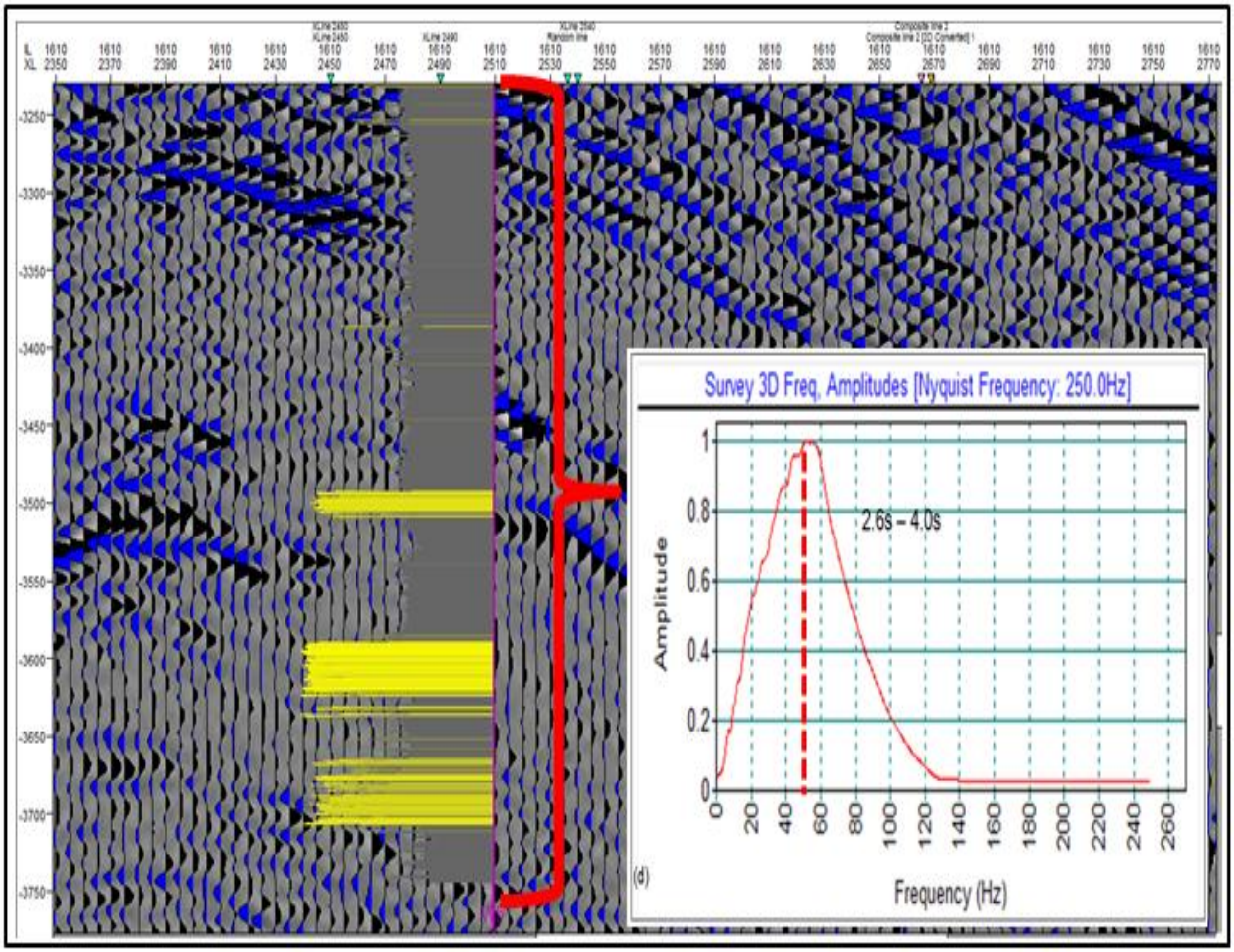

Figure 27: Spectral analysis of seismic data within 2.6 seconds and 4.0 seconds.

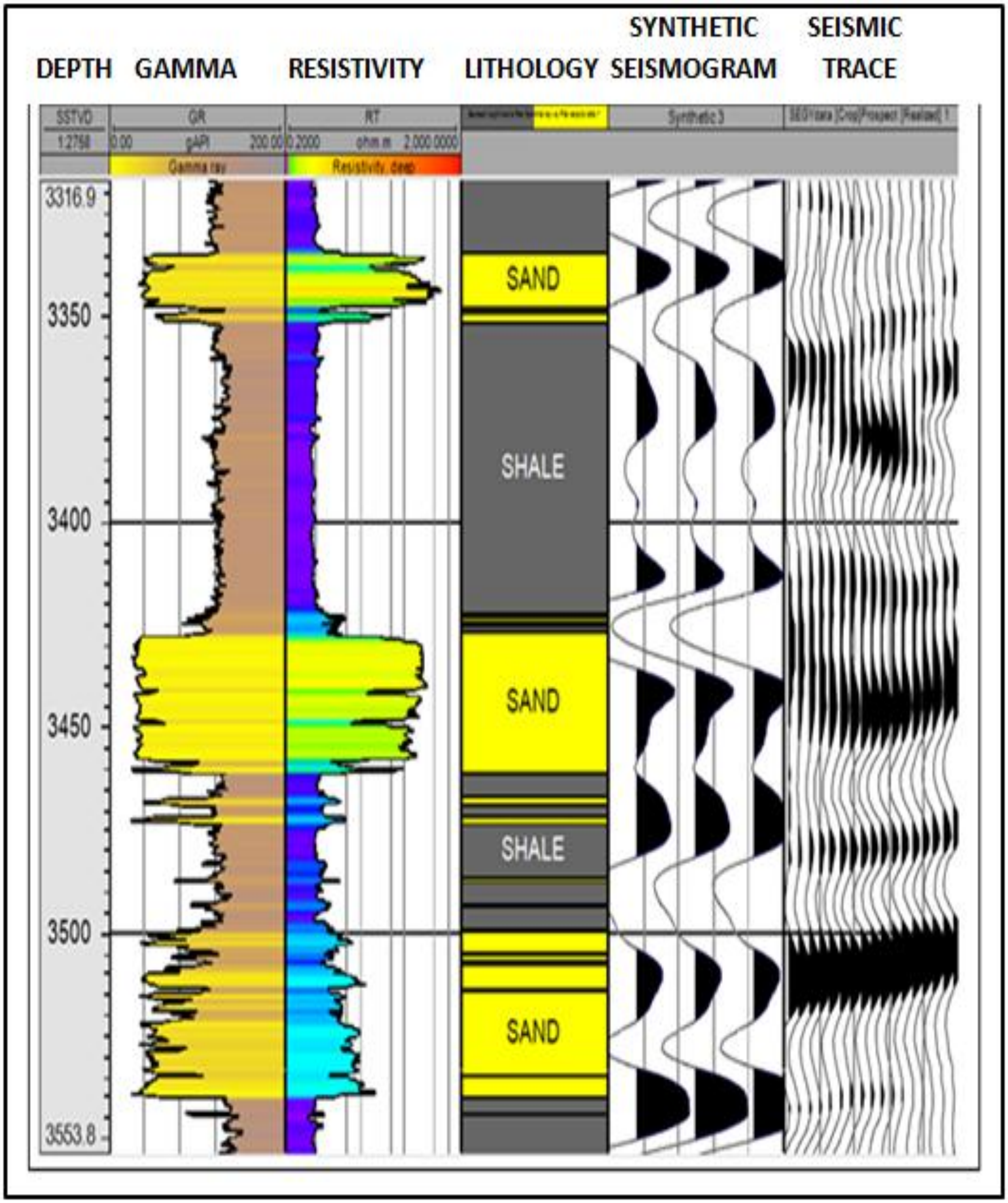

Figure 28: Well synthetic seismogram to seismic tie

4.4.3 Seismo-Structural Interpretation

Three shallow seismic reflectors including the sea bed were interpreted and mapped in the near-surface seismic window across the study area. Figure 29 shows the sea bed map in the study area with water depth ranging between 1300 m to 1700 m. This bathymetric range corresponds to the deepwater belts of the offshore Niger Delta.

Six reflectors were also interpreted across the interval of interest on seismic over the reservoir section.

The interval of interest is chosen based on lithology and petrophysical information from seven wells in the study area (Figure 30). A distinct structural closure is evidence on the vertical seismic sections. Figures 31 and 32 show orthogonal inline and cross line with well developed anticlinal structure. Figure 33 shows the depth structural map for the upper interval of interest with well developed anticlinal closure. The structure is defined by closed contour lines as shown in the depth structural map (Figure 33).

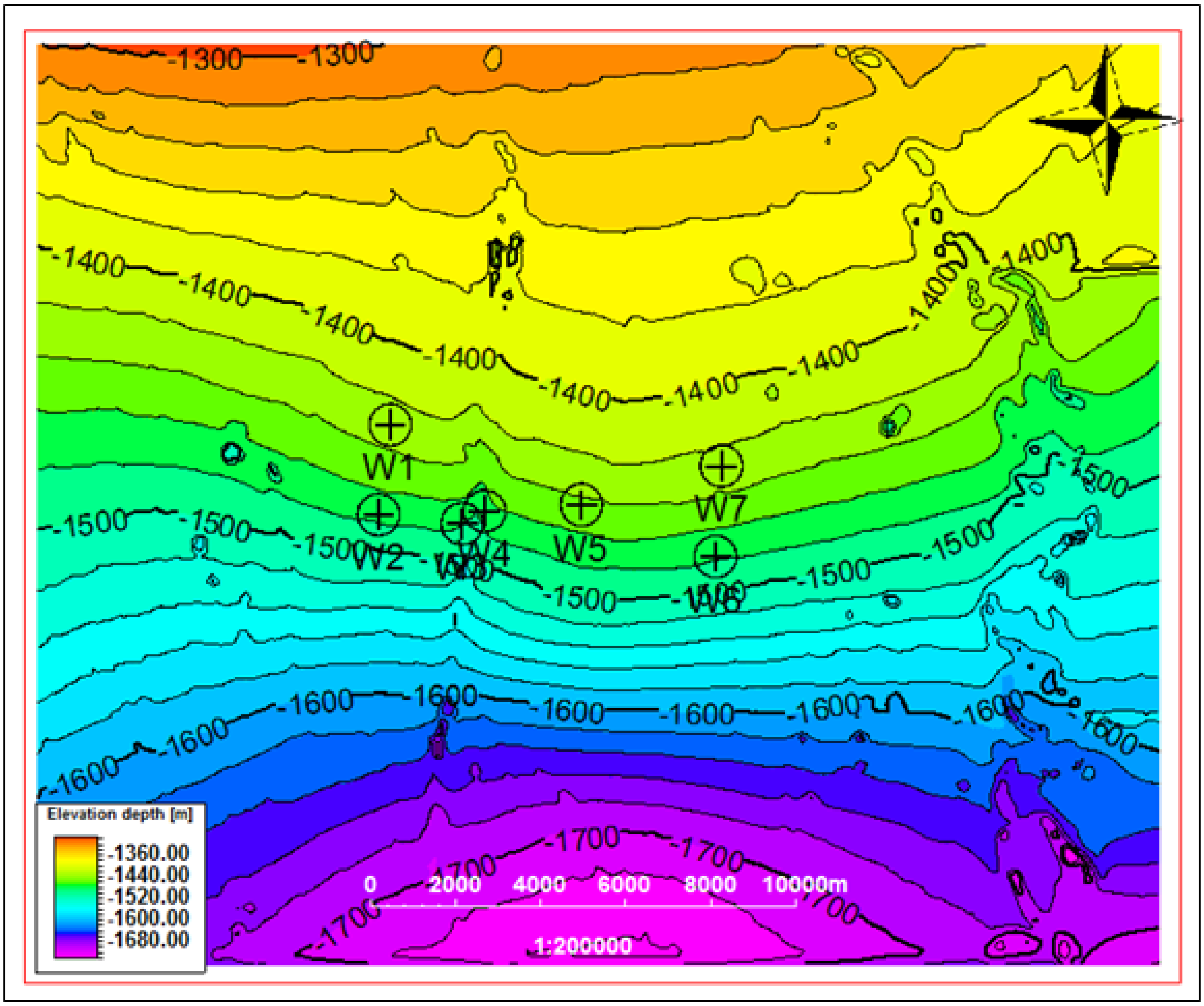

Figure 29: Depth structural map of the sea bed

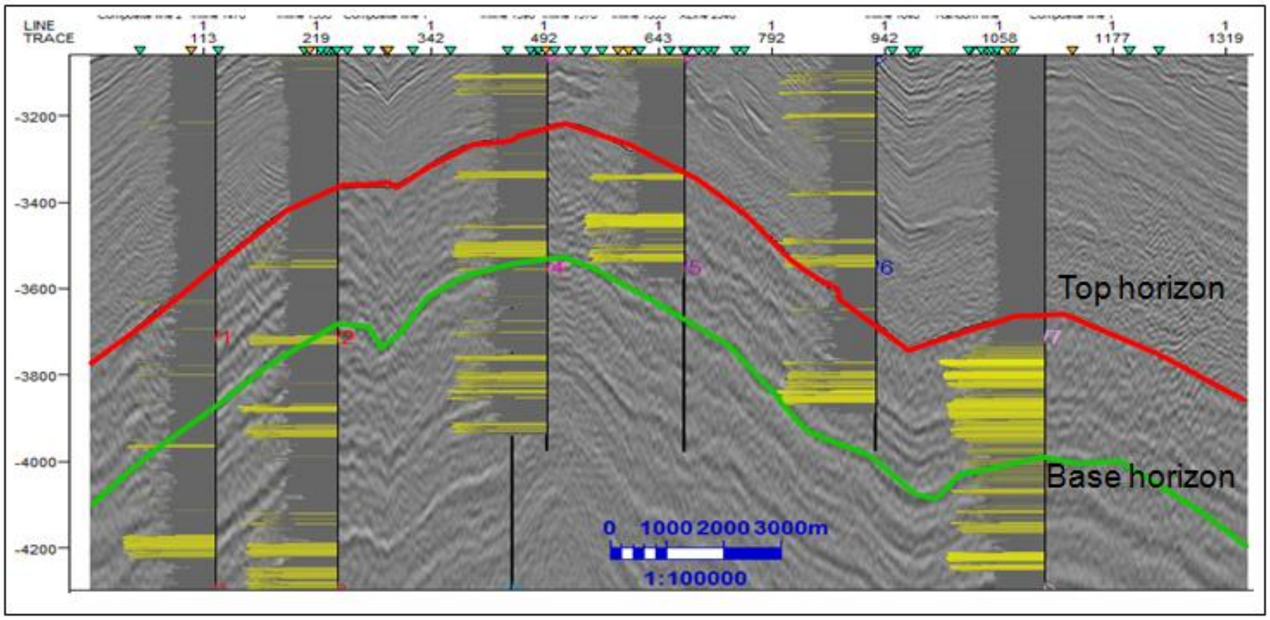

Figure 30: Depth converted arbitrary seismic section across the wells

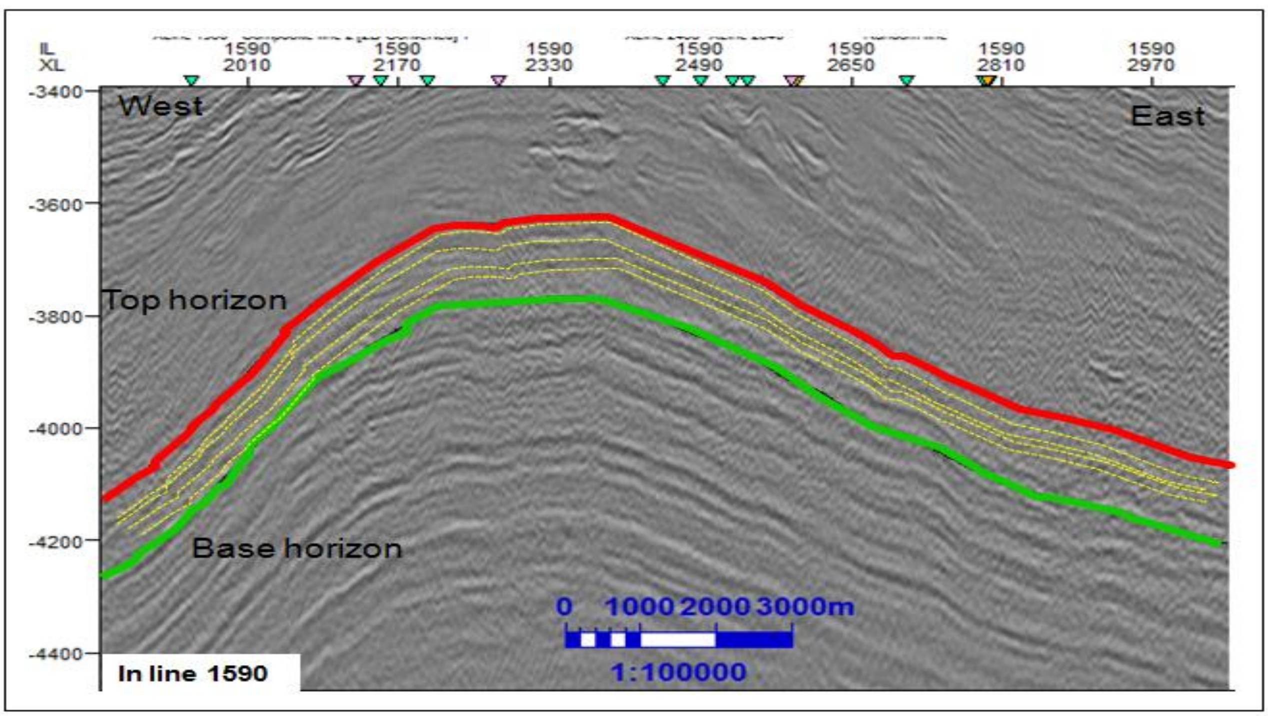

Figure 31: Inline 1590 showing anticlinal high over the reservoir interval of interest

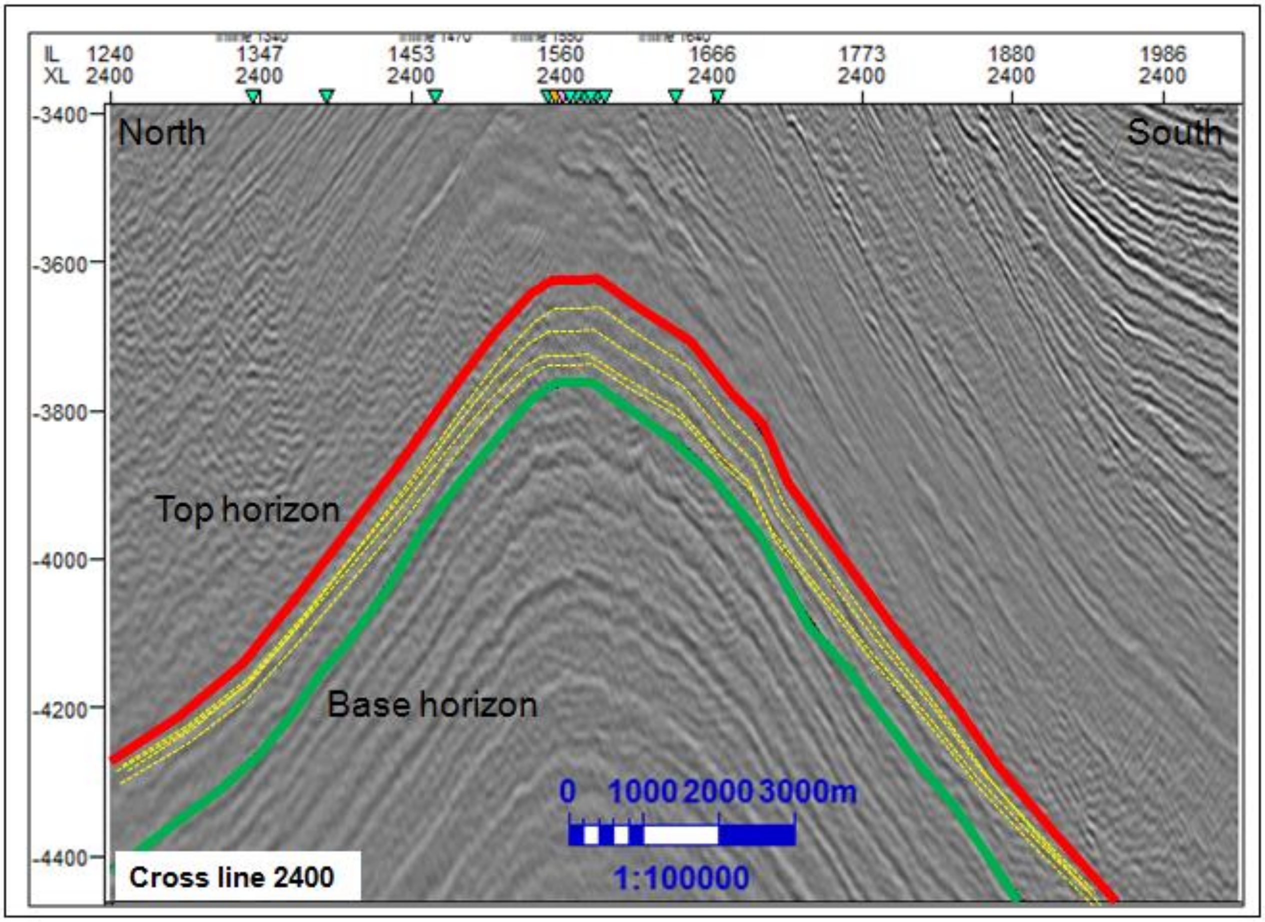

Figure 32: Crossline 2400 showing anticlinal high over the reservoir interval of interest

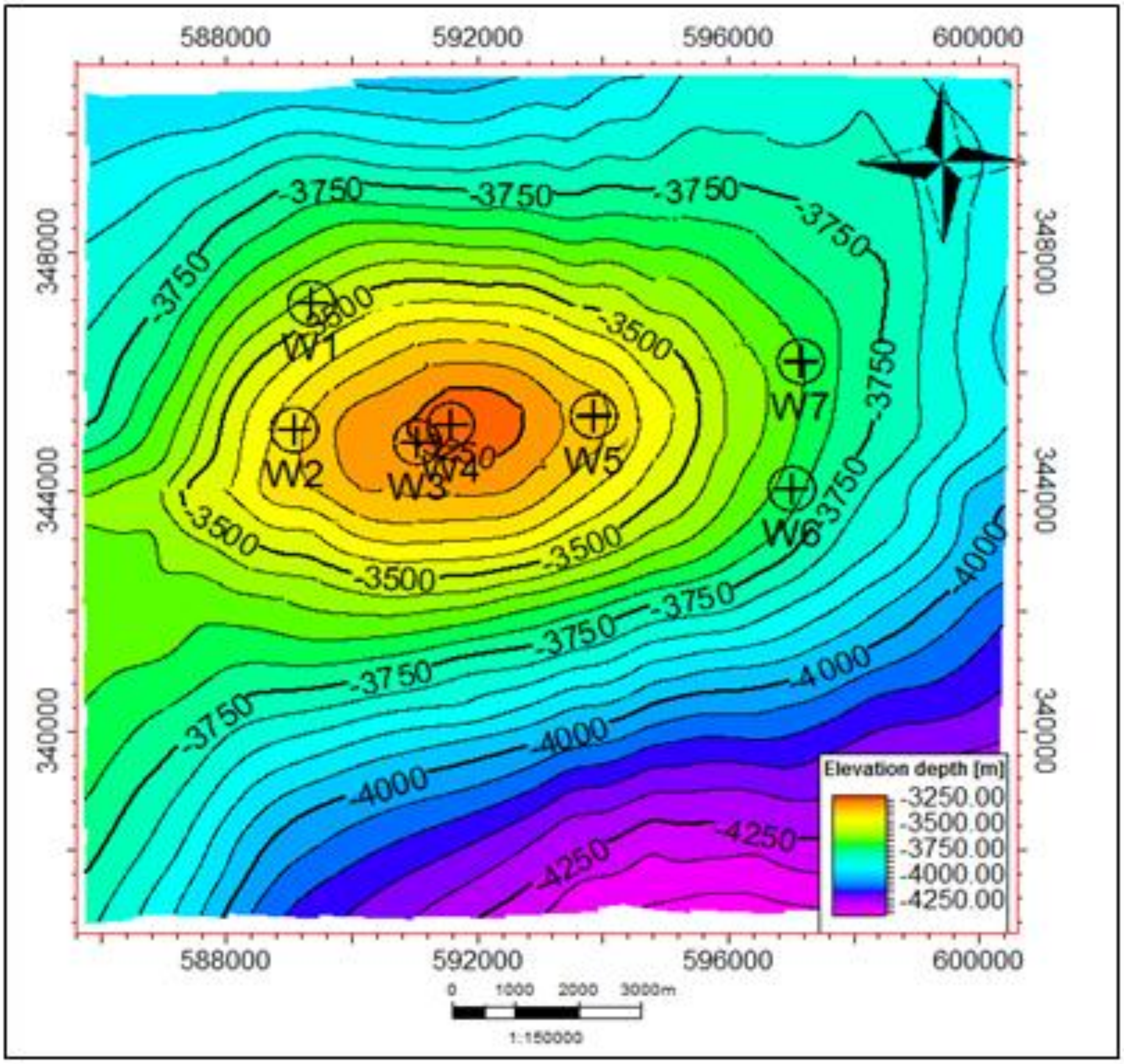

Figure 33: Depth structural map of the top seismic horizon interpreted and used for the 3D structural grid construction.

4.4.4 Seismic Stratigraphic Interpretation

Seismic facies analysis of reflection continuity, frequency, amplitude, and configuration have revealed near surface channels and depositional fan. The imprints of channels and stratigraphic features are evident in vertical seismic sections as well as on variance and RMS amplitude seismic cubes. Channel scours are present in inline 1670 (Figure 34). The seismic facies is predominantly characterised by high frequency parallel internal reflections. The variance attribute slices of the near surface reflectors show sinuous channels, oriented from north to south in the eastern corner of the study area (Figure 35).

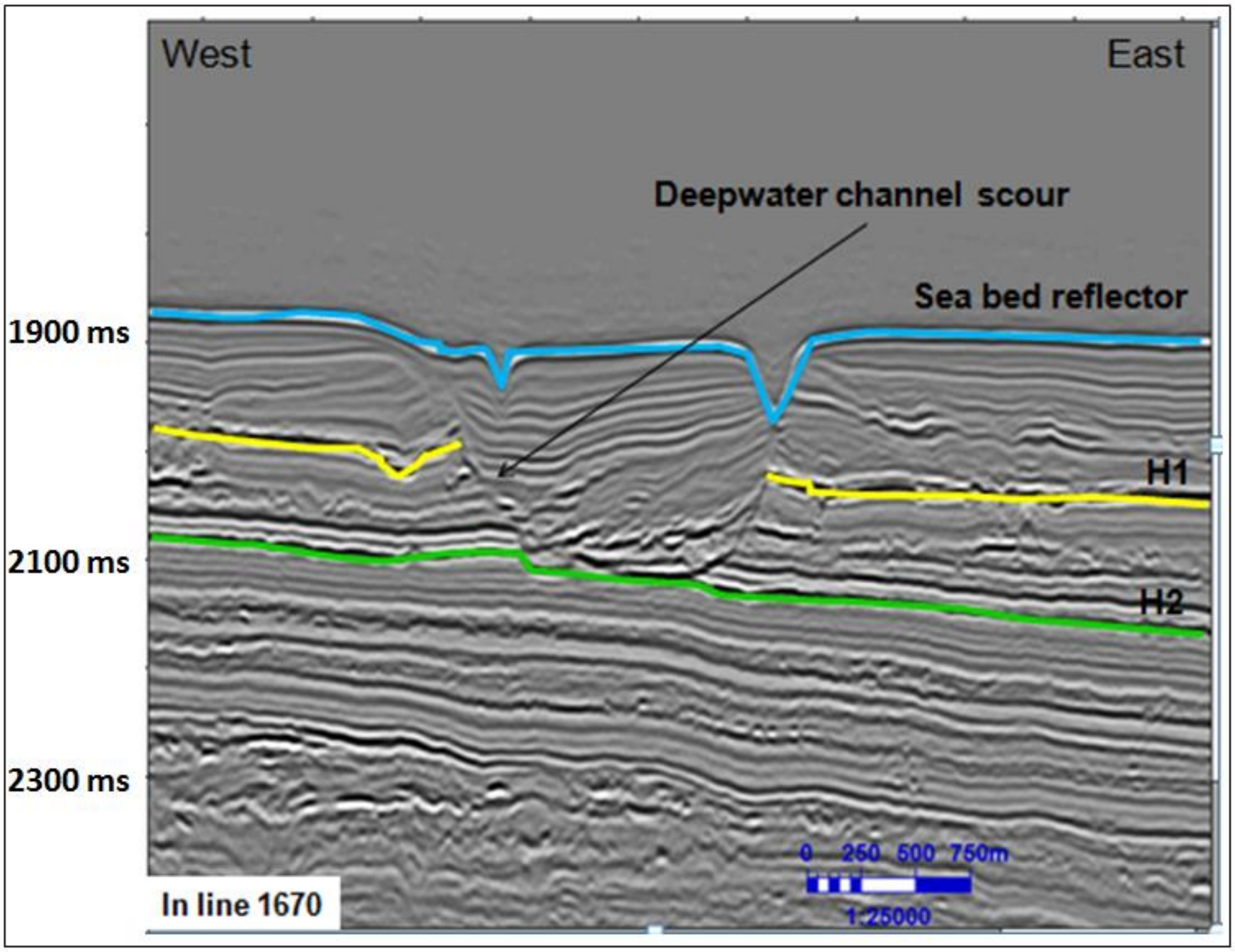

Figure 34: Seismic stratigraphic facies and channel detection on seismic attribute.
Coloured lines represents sea bed and shallow seismic horizons picks

The channel has a near zero orientation in the north-south direction stretching over 18 km basinward. The channel width ranges between 1000 m and 1700 m. The channel amplitude is between 500 m and 900 m, while wavelength is between 2200 m and 2700 m (Figure 35).

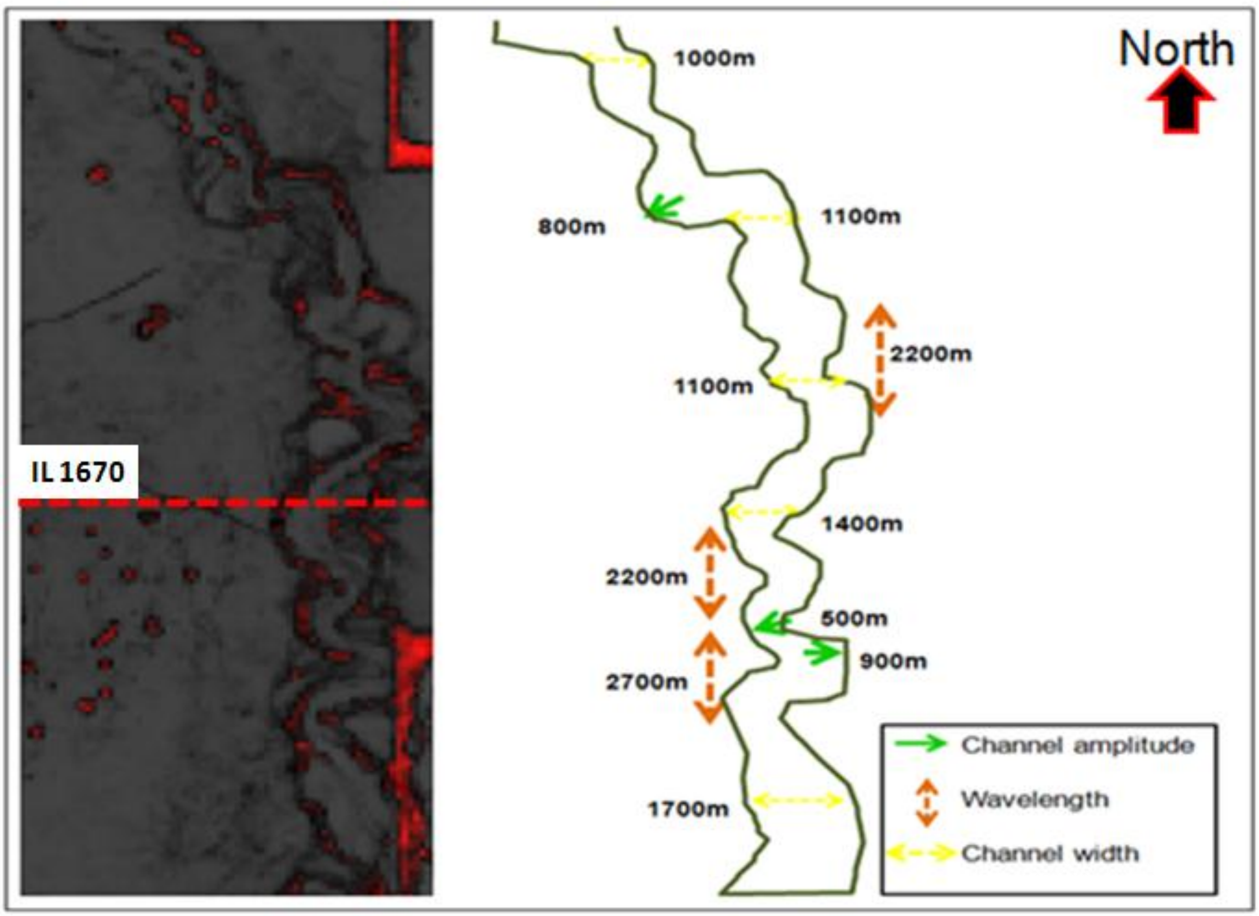

Figure 35: Variance attribute and channel geometry

Inline 2050 in Figure 36 shows low frequency, high amplitude, and mounded reflection package on the seismic sections. Instantaneous amplitude (envelope) strata slice of the sea bed revealed a high amplitude terminal fan lobe (Figure 37). A similar seismic facies architecture is observed using sweetness attribute, reflection intensity and RMS amplitude. However, acoustic impedance attribute, instantaneous frequency, amplitude, dominant frequency, and a host of other seismic attributes are unable to discriminate between the fan architectural morphology and background facies.

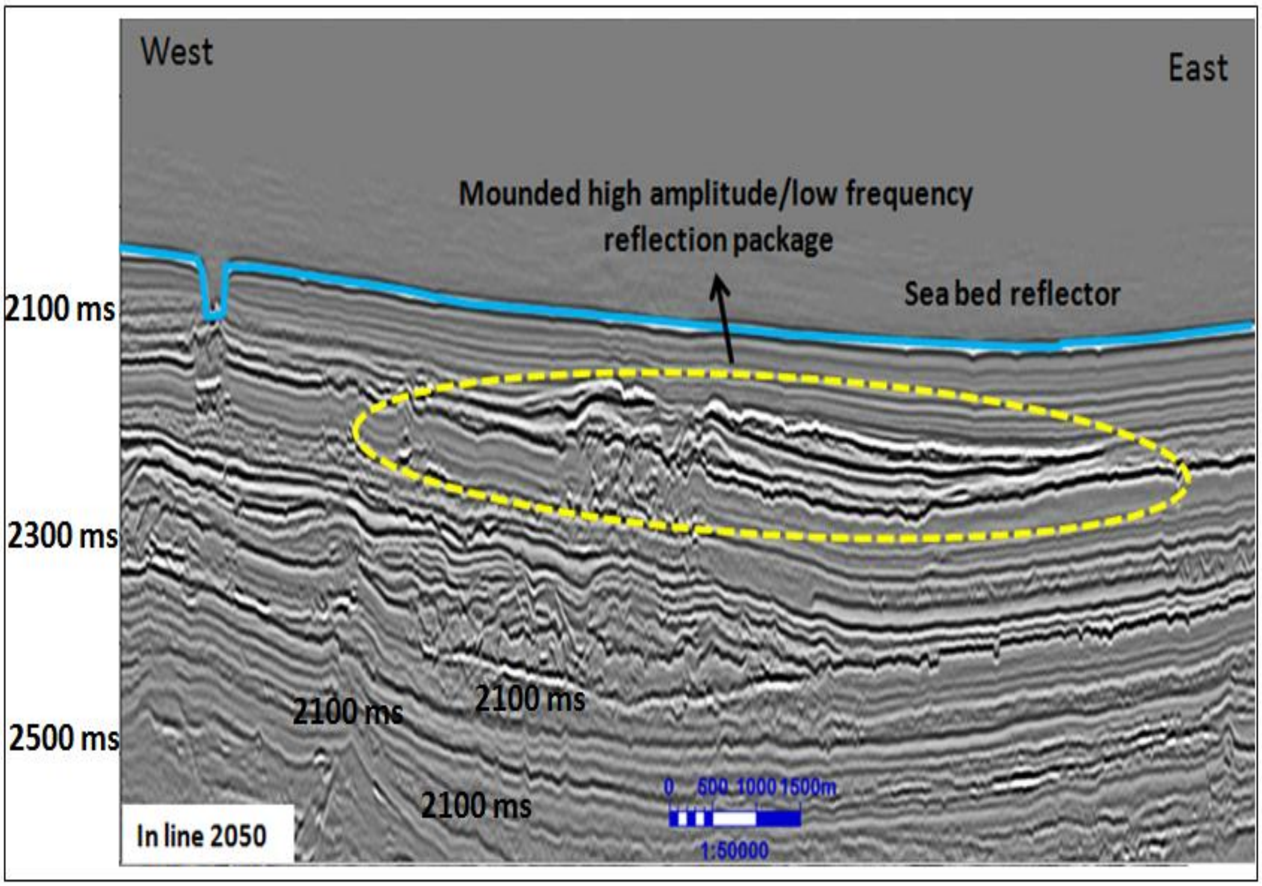

Figure 36: Seismic stratigraphic facies and seismic attribute detection of depositional fan

The architectural fan lobe as shown in Figure 37 consists of laterally amalgamated lobes ranging between 800 m and 3000 m in width. The high amplitude architectural fan is indicative of turbidite fan surrounded by background shale. The shale is characterised by low instantaneous amplitude in the attribute strata cube and high frequency parallel reflection on the seismic sections.

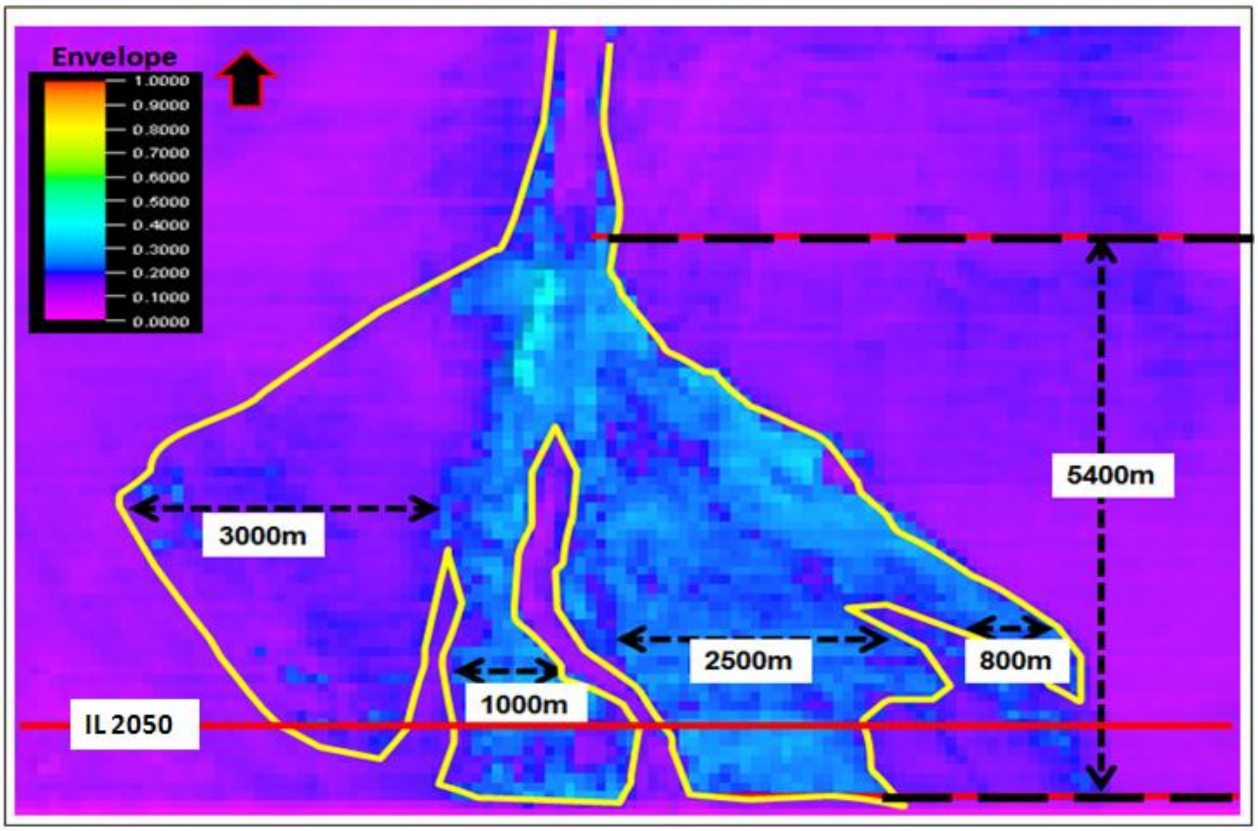

Figure 37: Architectural fan lobe with lateral amalgamation

4.4.5 Multi-Attribute Seismic Interpretation and Correlation

Different volumes of post stack seismic attributes were generated at the interval of interest and calibrated with elastic rock physics properties from well logs (Table 5). Figure 38 shows sweetness versus mu-rho cross plot with shale volume as the third axis. High sweetness corresponds to high mu-rho and low shale volume. This is indicative of quartz-rich sandstone unit. Key post-stack seismic attributes: including amplitude envelope, sweetness, RMS amplitude and reflection intensity, show high correlation coefficient with diagnostic rock physics properties between 0.66 and 0.8 (Table 5). Other seismic attributes including instantaneous frequency, acoustic impedance, give correlation coefficients less than 0.5.

Table 5 Seismic attributes and elastic rock property correlation

Seismic Attribute Versus Rock Properties cross plots	Clean Sand (Correlation Coefficient)	Shaly Sand (Correlation Coefficient)
Reflection intensity- Young's modulus	0.8	0.52
Reflection intensity- Mu-rho	0.8	0.6
Reflection intensity- Lambda-rho	-0.72	-0.29
Reflection intensity- Vp/Vs	-0.77	-0.54
Reflection intensity - Poisson's ratio	-0.79	-0.51
Sweetness- Young's modulus	0.76	0.63
Sweetness- Mu-rho	0.76	0.69
Sweetness- Lambda-rho	-0.68	-0.46
Sweetness - Vp/Vs	-0.73	-0.65
Sweetness - Poisson's ratio	-0.76	-0.64
RMS amplitude- Young's modulus	0.77	0.53
RMS amplitude- Mu-rho	0.78	0.6
RMS amplitude- Lambda-rho	-0.7	-0.31
RMS amplitude- Vp/Vs	-0.75	-0.55
RMS amplitude- Poisson's ratio	-0.77	-0.52
Envelope- Young's modulus	0.74	0.5
Envelope- Mu-rho	0.74	0.57
Envelope- Lambda-rho	-0.66	-0.27
Envelope- Vp/Vs	-0.7	-0.51
Envelope - Poisson's ratio	-0.73	-0.48
Instantaneous frequency- Young's modulus	-0.32	-0.19
Instantaneous frequency- Mu-rho	-0.28	-0.22
Instantaneous frequency- Lambda-rho	0.47	0.12
Instantaneous frequency - Vp/Vs	0.34	0.22
Instantaneous frequency - Poisson's ratio	0.37	0.2
Acoustic impedance- Young's modulus	0.42	0.29
Acoustic impedance- Mu-rho	0.45	0.4
Acoustic impedance- Lambda-rho	-0.36	-0.25
Acoustic impedance- Vp/Vs	-0.46	-0.45
Acoustic impedance - Poisson's ratio	-0.45	-0.37

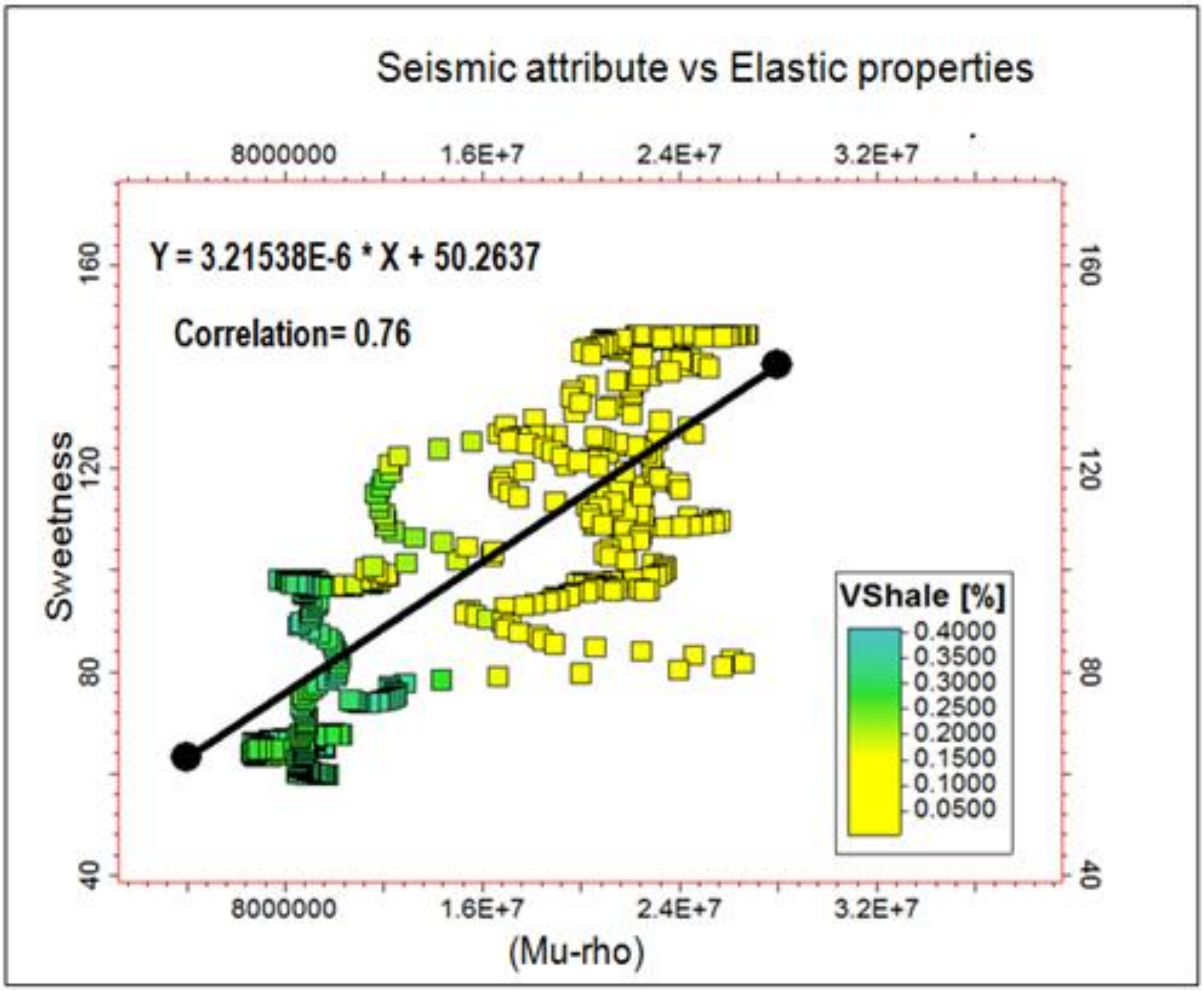

Figure 38: Sweetness attribute versus Mu-rho cross plot

.

Figure 39 shows filtered seismic attribute property slices in the vertical and horizontal direction respectively. The various seismic attributes are characterised by three dimensional facies contrast and distinct architectural facies pattern in plan view (Figure 40). Based on the calibrated elastic rock properties, petrophysical and lithological properties; the contrasting seismic facies are diagnostic of sand prone and shale prone lithofacies respectively.

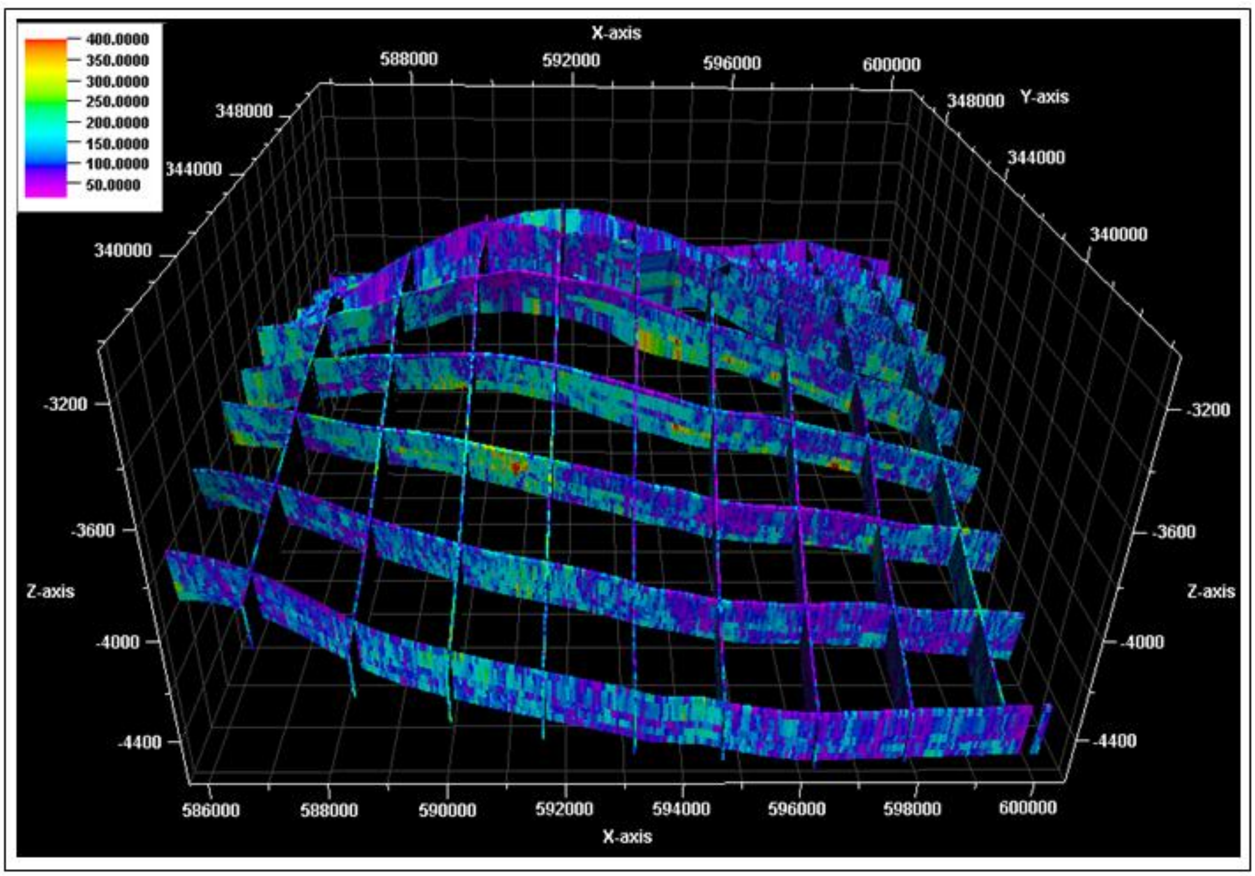

Figure 39: A typical seismic attribute (Sweetness) grid filtered to show seismic facies contrast in three dimension

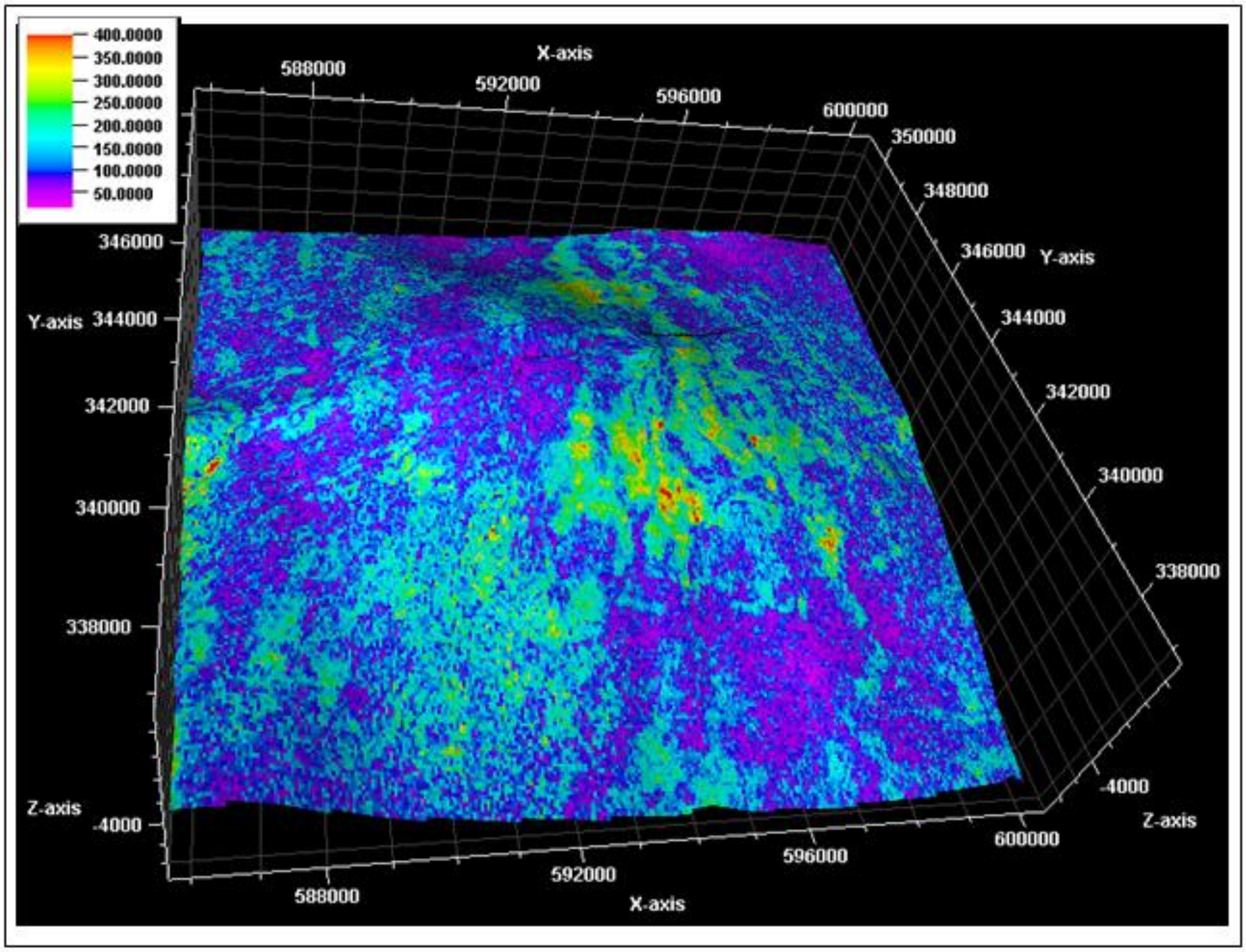

Figure 40: A typical seismic attribute (Sweetness) property layer along the vertical direction

Figure 41 represents empirically derived porosity volume estimated from a set of Benayol seismic porosity equations in the study area. The equations are stated as linear functions of interpreted seismic attributes including: reflection intensity, sweetness, RMS amplitude, and envelope.

- Porosity = 0.6*Reflection intensity + 0.05
- Porosity = 0.0007*Sweetness + 0.047
- Porosity = 0.00015*RMS amplitude + 0.05
- Porosity = 0.00015*Envelope + 0.057

The seismic derived porosity compares very well with the modeled log porosity distribution (Figure 42). The porosity values ranges between 0.04 to 0.36. Higher porosity values between 0.2 and 0.36 are indicative of sand prone facies while the porosity values less than 0.2 are characteristic of shales.

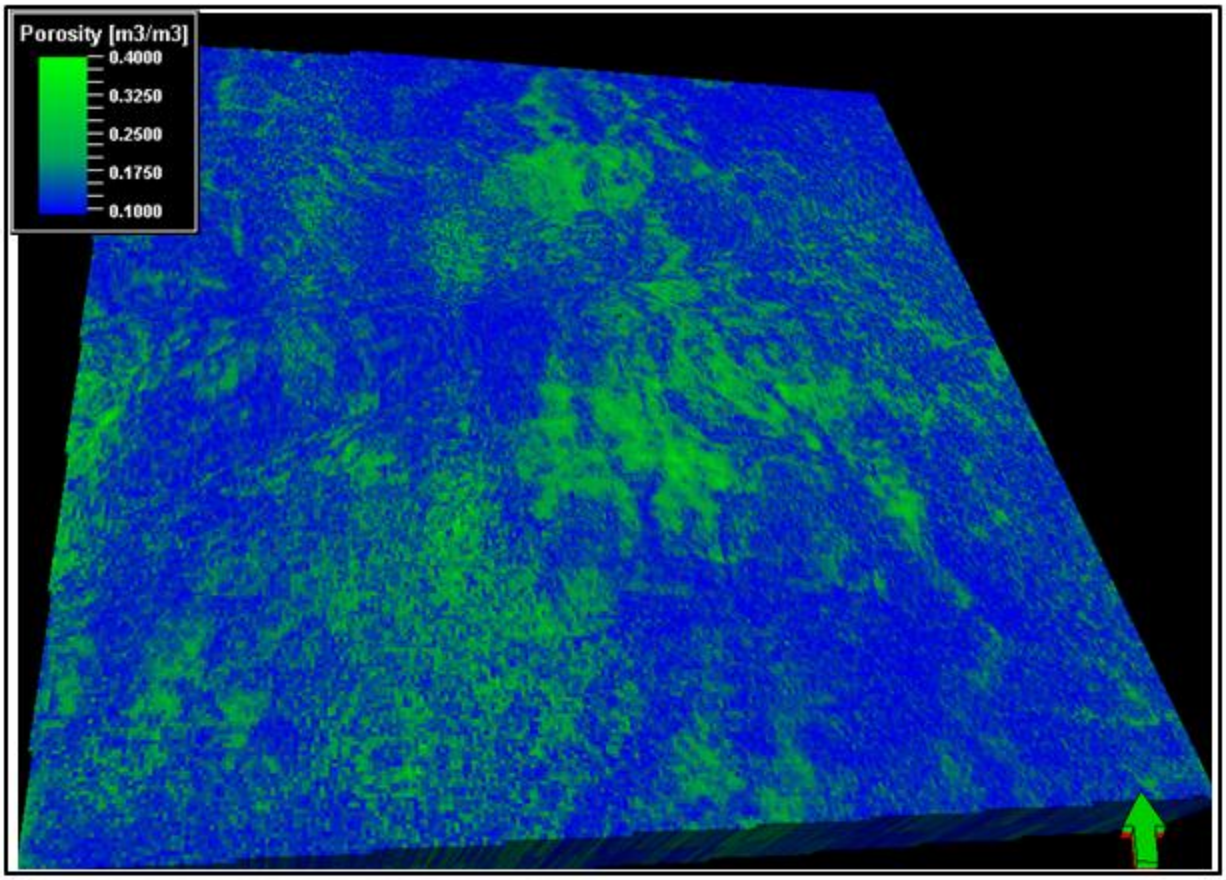

Figure 41: Seismic attribute inverted porosity grid

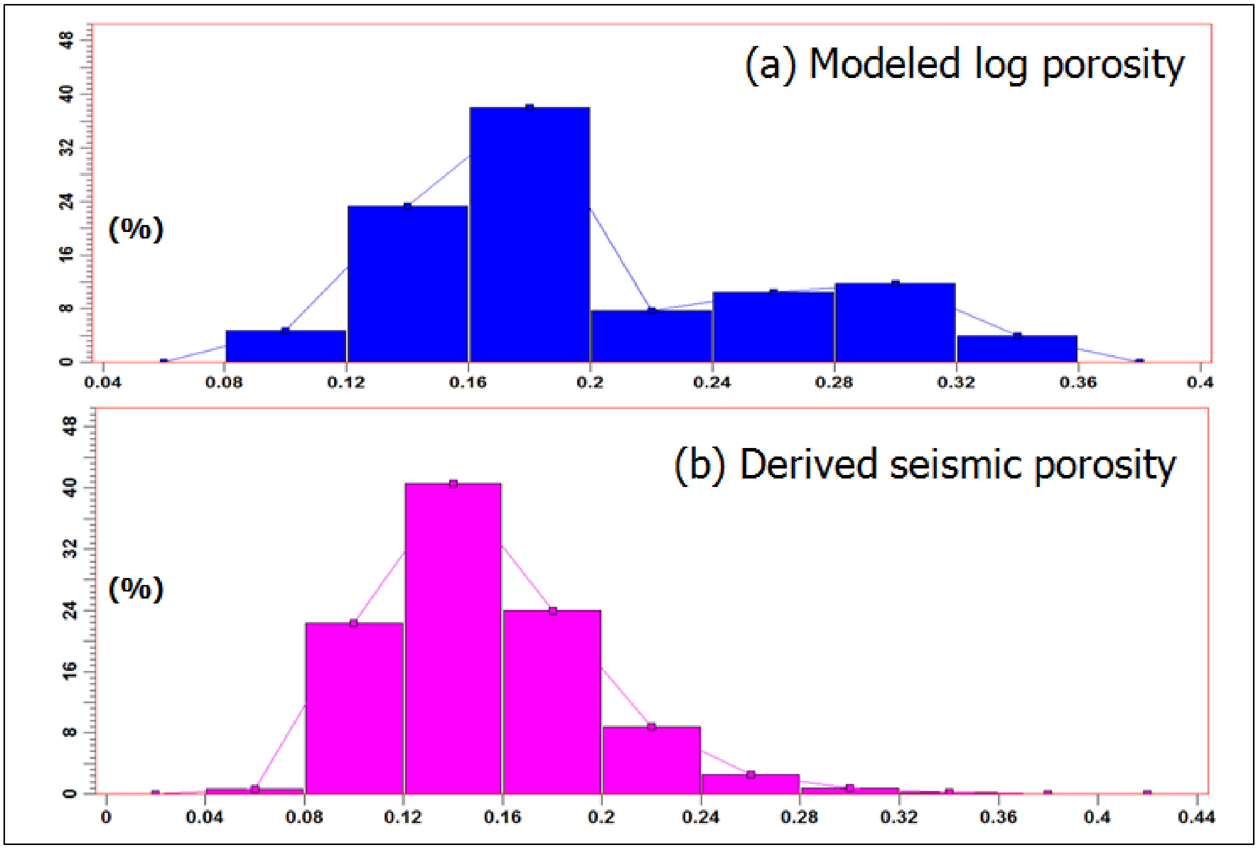

Figure 42: Porosity histograms for (a) Modeled log porosity and (b) Seismic derived porosity

4.4.6 Seismic Attributes Facies Characterisation

Tables 6 and 7 show the results of principal component and correlation analysis used in selecting diagnostic seismic attributes for neural network classification of seismic facies. Sweetness, reflection intensity, RMS amplitude, and envelope generally have high correlation values. However, out of the six principal components identified in Table 6, only three have significant percentage contribution and Eigen values in the matrix cluster. Hence three discrete classes were chosen in the unsupervised classification of the seismic attributes.

Table 6: Typical results of the principal component analysis for discrete facies classification of seismic attributes in the study area

	Principal Components (PC)					
Correlation Coefficient / Seismic Attributes	**PC1**	**PC2**	**PC3**	**PC4**	**PC5**	**PC6**
Sweetness	0.9951	0.0021	0.0184	0.0967	0.0045	0.0045
Reflection intensity	0.9921	-0.0103	0.0189	-0.1121	0.0528	0.0000
RMS amplitude	0.9944	-0.0103	0.0245	-0.0816	-0.0617	0.0000
Quadrature	0.0768	0.5279	-0.8458	-0.0017	-0.0004	0.0000
Original amplitude	0.0285	-0.8502	-0.5256	0.0017	-0.0001	0.0000
Envelope	0.9951	0.0021	0.0184	0.0967	0.0045	-0.0045
Eigen value	3.9602	1.0018	0.9933	0.0379	0.0066	0.0000
Contribution (%)	66.00	16.70	16.56	0.63	0.11	0.00
Cumulative contribution (%)	66.00	82.70	99.26	99.89	100.00	100.00

Table 7: A typical correlation analysis for the discrete facies classification of seismic attributes

Correlation Analysis	Sweetness	Reflection Intensity	RMS Amplitude	Quadrature	Original Amplitude	Envelope
Sweetness	1.0000	0.9769	0.9818	0.0617	0.0170	1.0000
Reflection Intensity	0.9769	1.0000	0.9930	0.0549	0.0269	0.9770
RMS Amplitude	0.9818	0.9930	1.0000	0.0503	0.0241	0.9818
Quadrature	0.0617	0.0549	0.0503	1.0000	0.0021	0.0617
Original Amplitude	0.0170	0.0269	0.0241	0.0021	1.0000	0.0170
Envelope	1.0000	0.9770	0.9818	0.0617	0.0170	1.000

Figures 43 and 44 show discrete facies classes and facies probability of fan lobe for the near sea bed interval in the study area. The three discrete facies classes with code 0, 1, and 2 represent sinuous channel edge, background facies in, and fan shape lobate facies.

Similarly, Figures 45 and 46 show discrete facies classes and facies probability defined for the reservoir zone of interest. The two facies classes represent lobate fan deposits surrounded by a background facies.

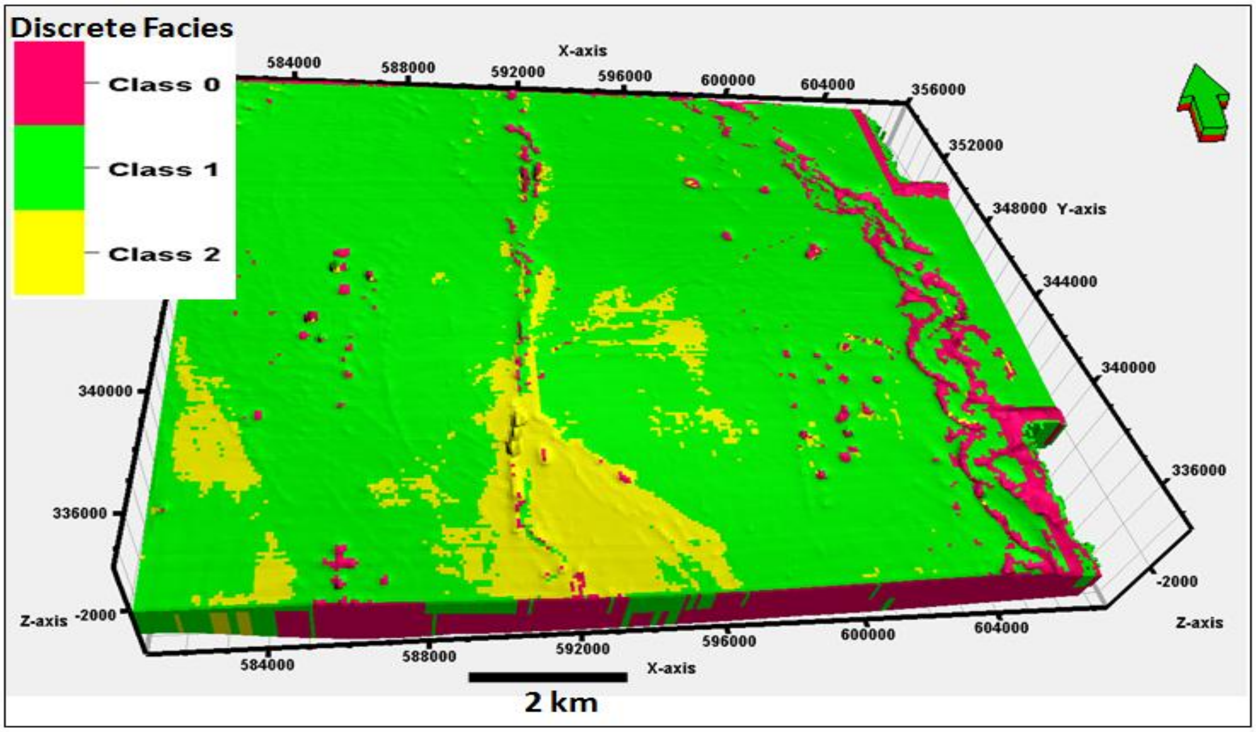

Figure 43: Near Sea Bed Discrete facies classes showing lobate fan architecture and sinuous channel

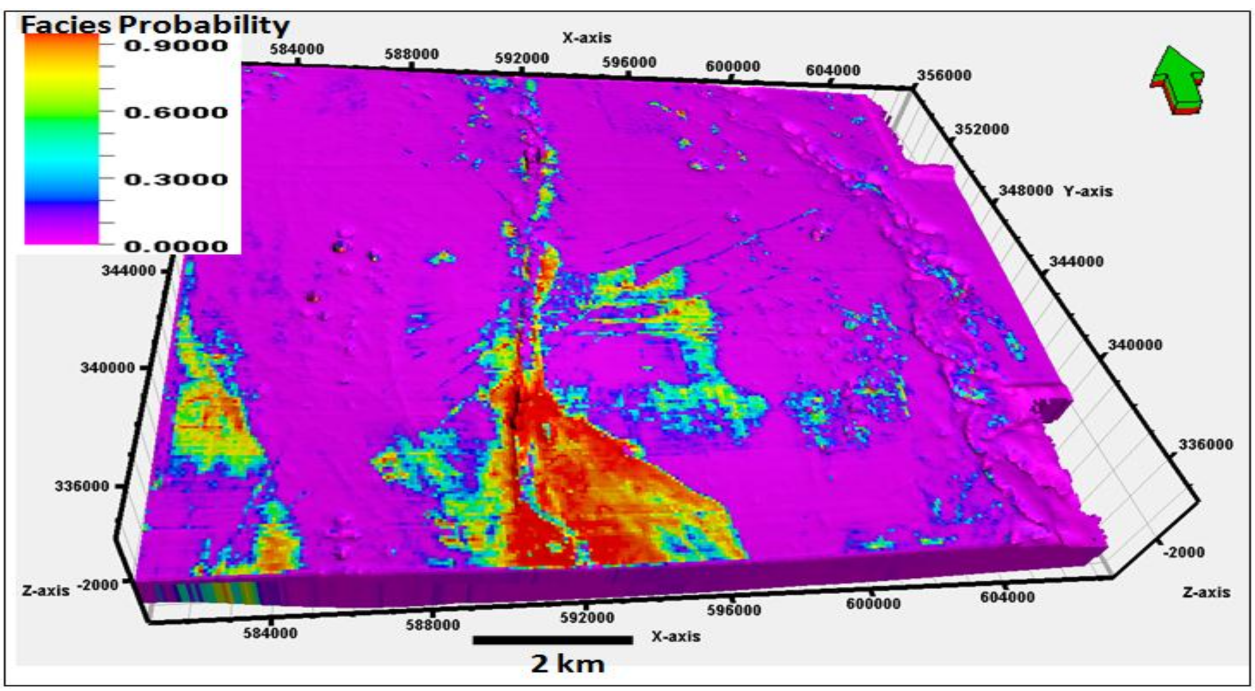

Figure 44: Near Sea Bed Seismic facies probability volume for Class 2

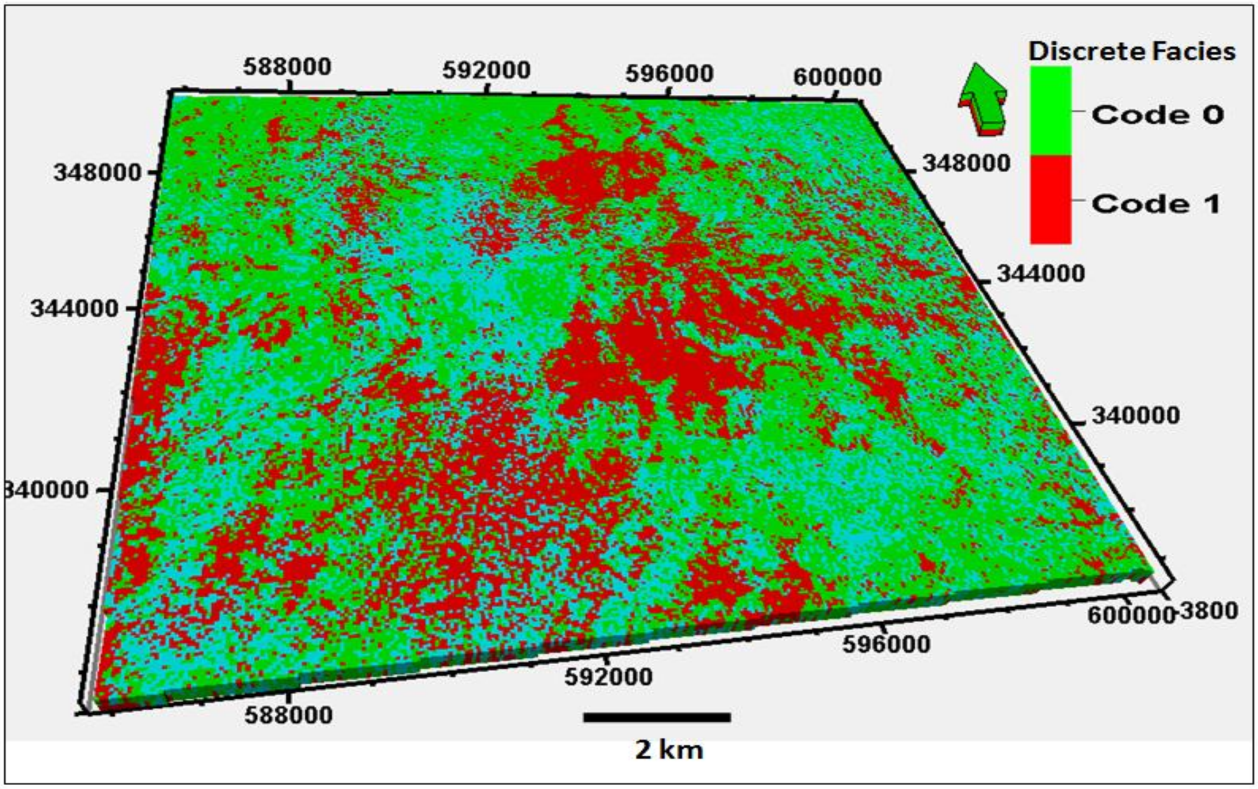

Figure 45: Discrete facies class showing lobate fan architecture in RED and background facies in GREEN within the reservoir interval

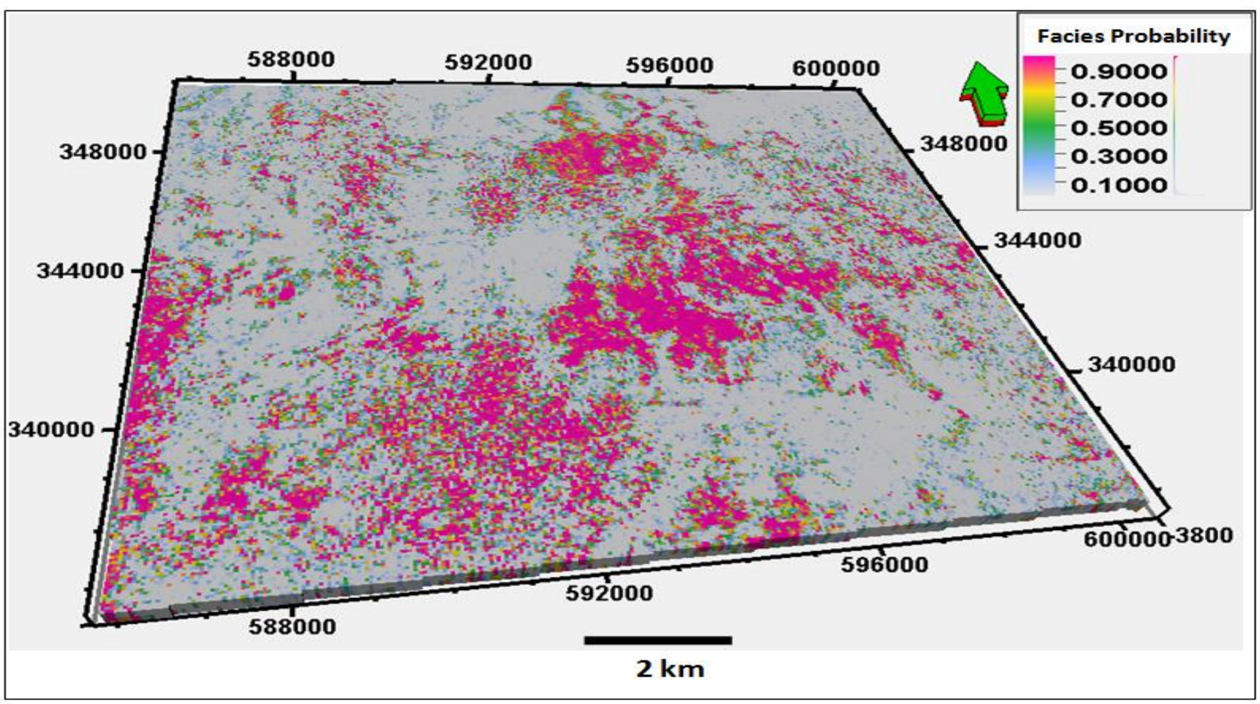

Figure 46: Seismic facies probability volumes at reservoir interval for lobate fan

4.5 Core and Sedimentological Facies Results

4.5.1 Sedimentological Core Description

Core photographs of shale and sandstone units between 3330 m and 3346.3 m depth subsea in well W-5 reveal diagnostic sedimentary structures and depositional facies (Appendix D, Figures 47 to 52). The cored section shows a fining upward sedimentary sequence of sand units overlain by siltstone and mudstone. The siltstone and mudstone show faint normal grading and parallel laminations. There are also evidence of floating mud clasts in sandstone as well as sand injectite in the shale between 3332 m and 3334 m depths (Figures 47 and 48). The lithofacies types are mainly shale and sandstone with minor siltstone fraction. The shale show evidence of lamination, lenticular bedding and mud clast.

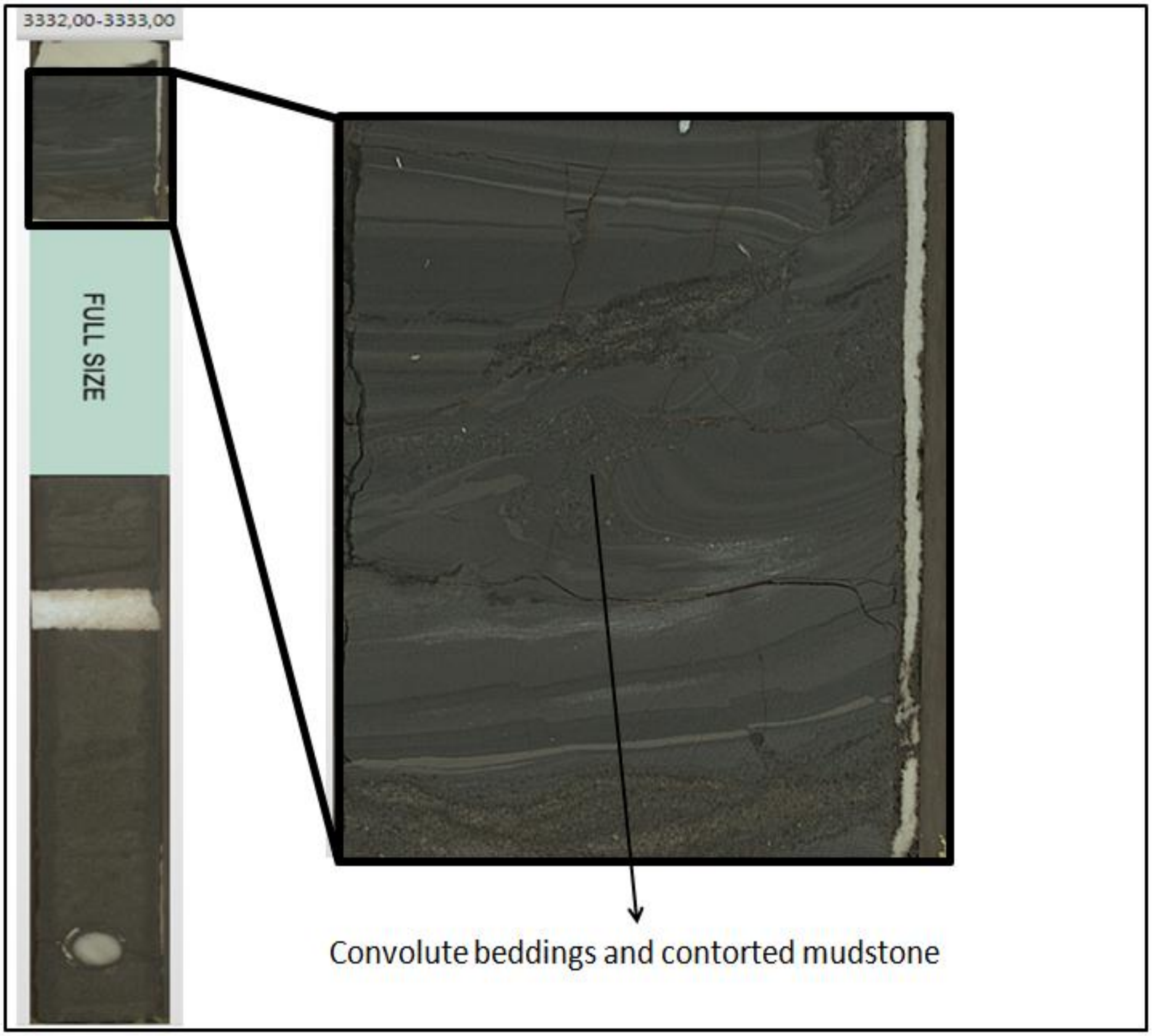

Figure 47: Core section showing deformed shale and mudstone overlying fine grain sandstone unit

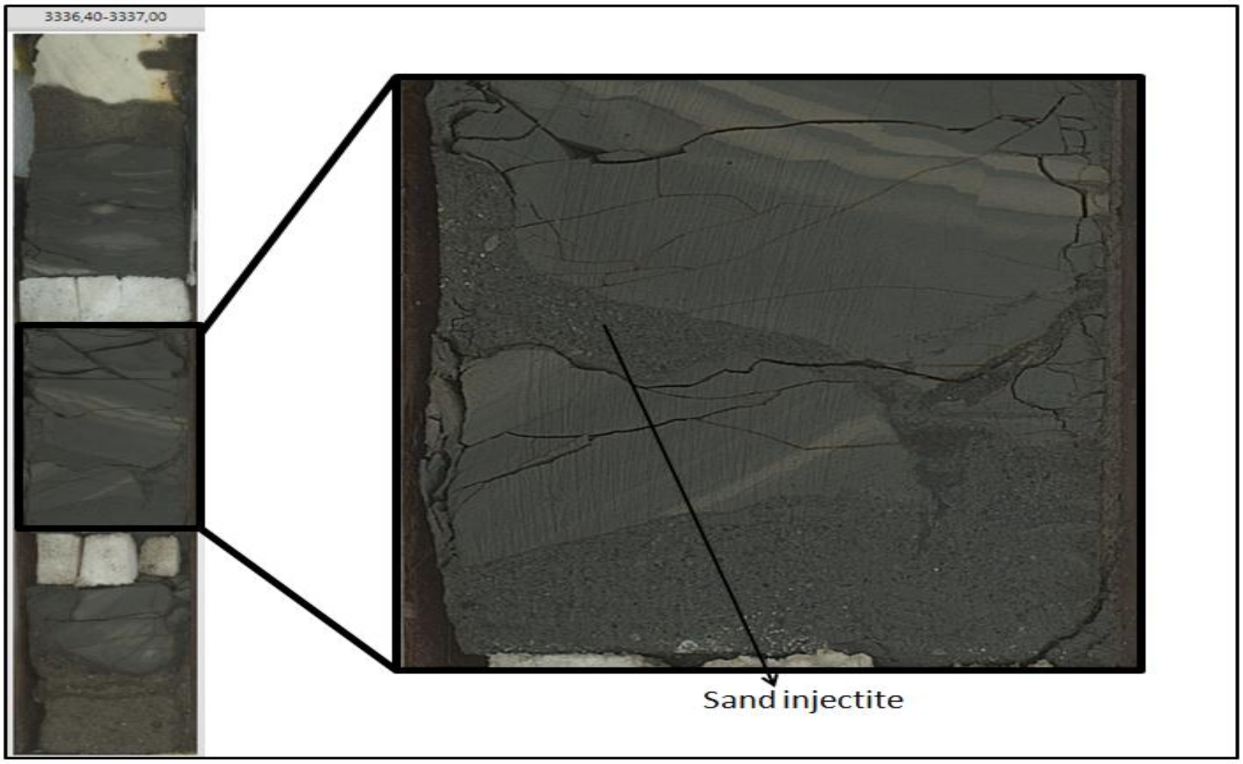

Figure 48: Cored shale interval with evidence of sand injectite

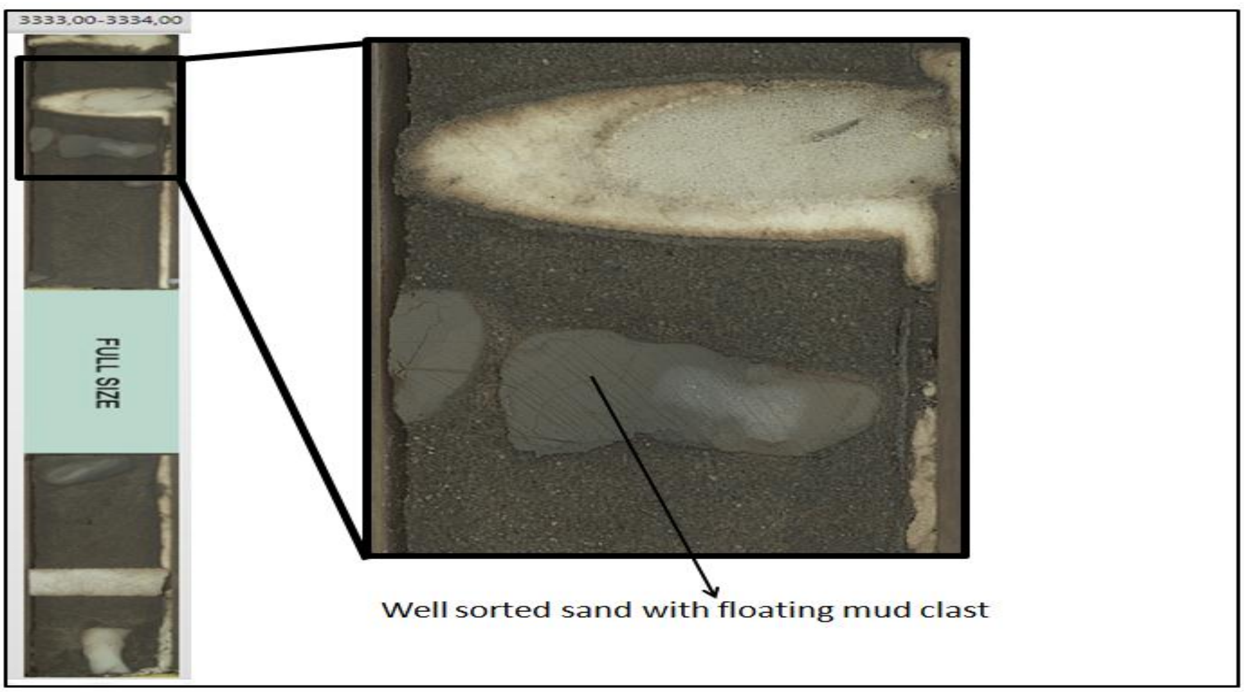

Figure 49: Cored sandstone section with floating mudclast

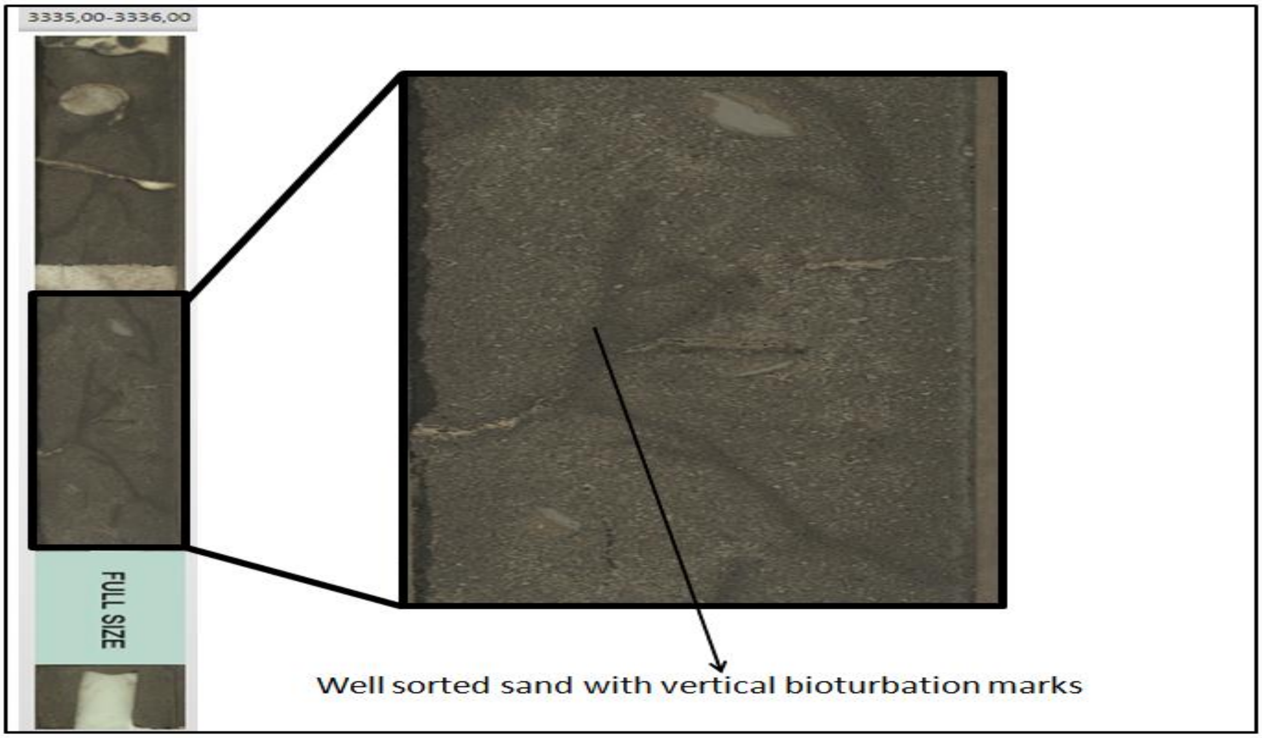

Figure 50: Cored fine grain sandstone with vertical burrows

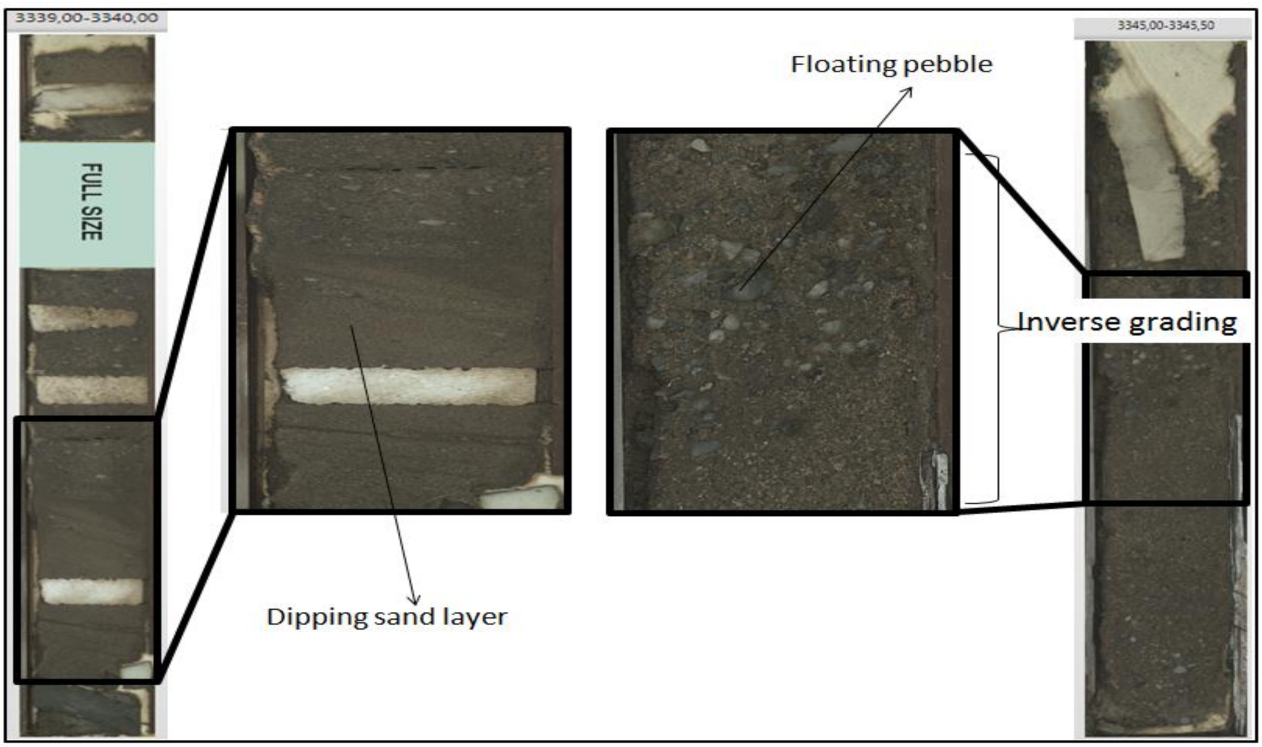

Figure 51: Cored sandstone intervals with inverse graded bedding and floating pebbles

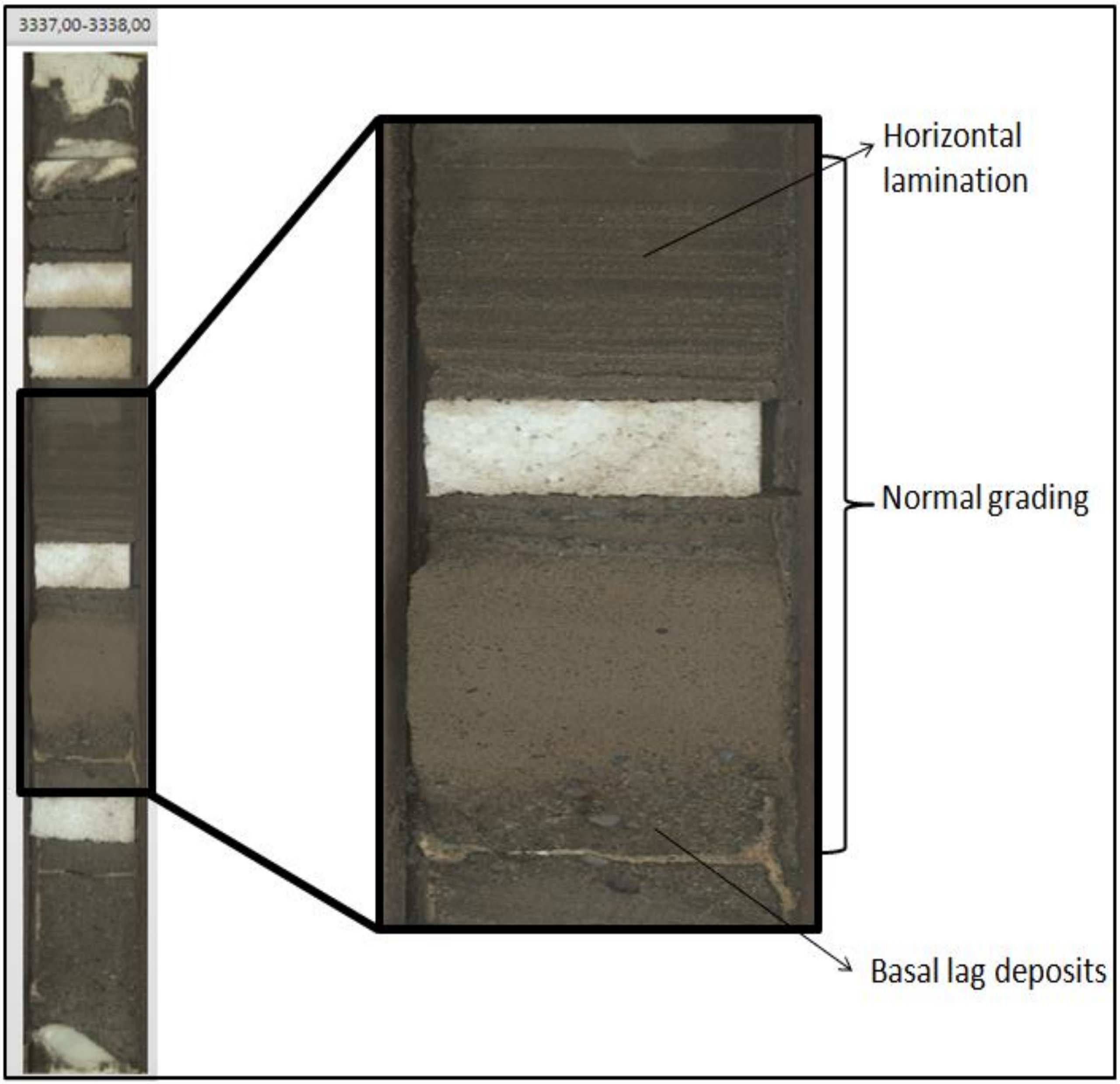

Figure 52: Cored sandstone interval showing normal grading with horizontal lamination and lag deposits.

Figure 53 shows the sedimentological log for 5.3 m cored gross sand interval and the accompanied textural description, sedimentary description, depositional facies and gamma ray log motif. The sand unit comprises of several cycles of centimeter scale deposits of sandy slumps, slides, debris flow and turbidity current channel facies as evident on the observed sedimentary structures. The sand units are moderately sorted and characterised by fine to coarse grained particle sizes, with normal and inverse grading. The fine and medium grained intervals show evidence of vertical burrows and bioturbation marks.

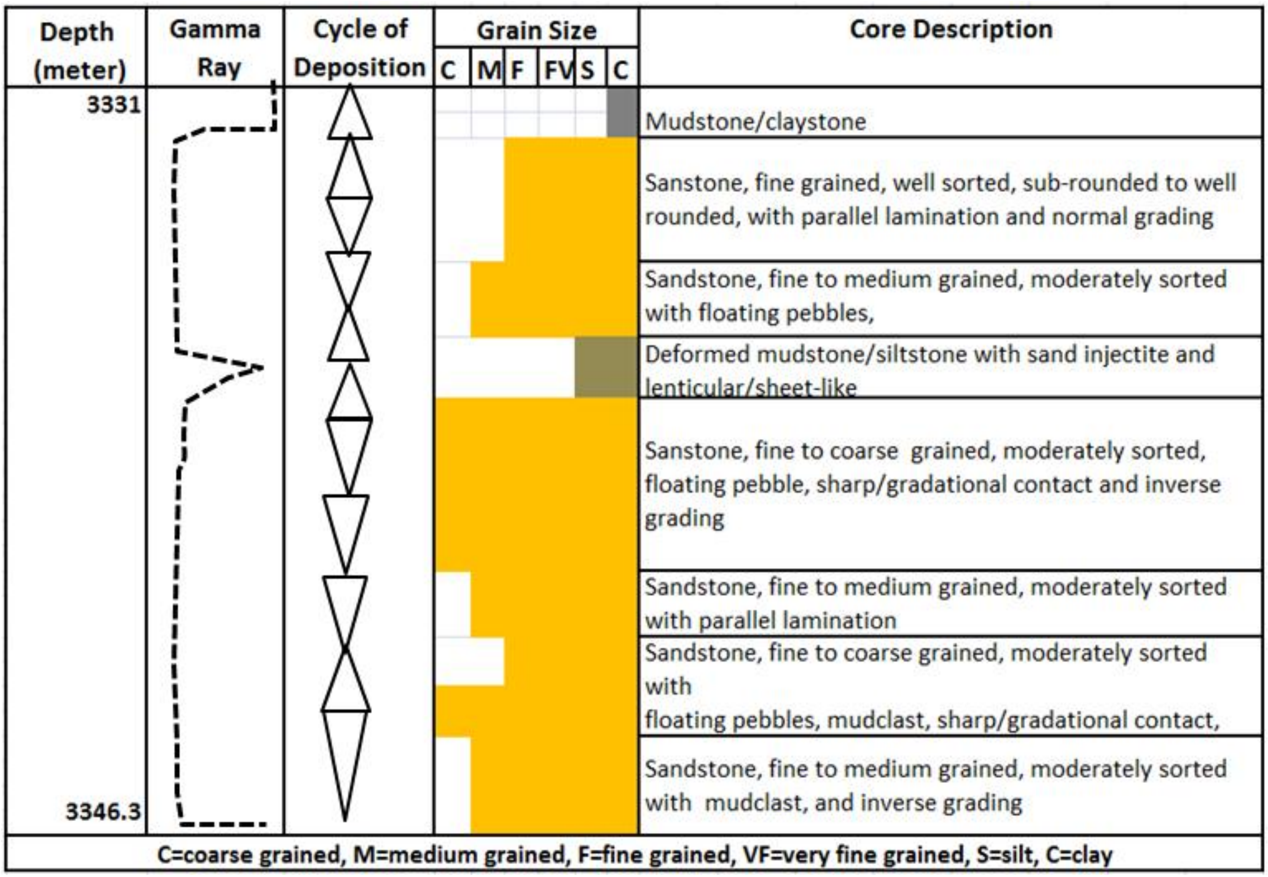

Figure 53: Core sedimentological log, textural description and sedimentary features. The triangular symbols represents centimeter scale cycles of sedimentation

4.6 Geostatistical Facies Modeling

4.6.1 Upscaled Lithofacies and Petrophysical Data

Upscaled seismic lithofacies from seven wells show the global facies proportion for shale and sand as 79% and 21% respectively in the study area. Figures 54 to 57 show the global facies proportion in the study area, histograms of porosity and volume of shale respectively. Table 8 shows the zonal facies proportion for sand and shale in the upscaled wells.

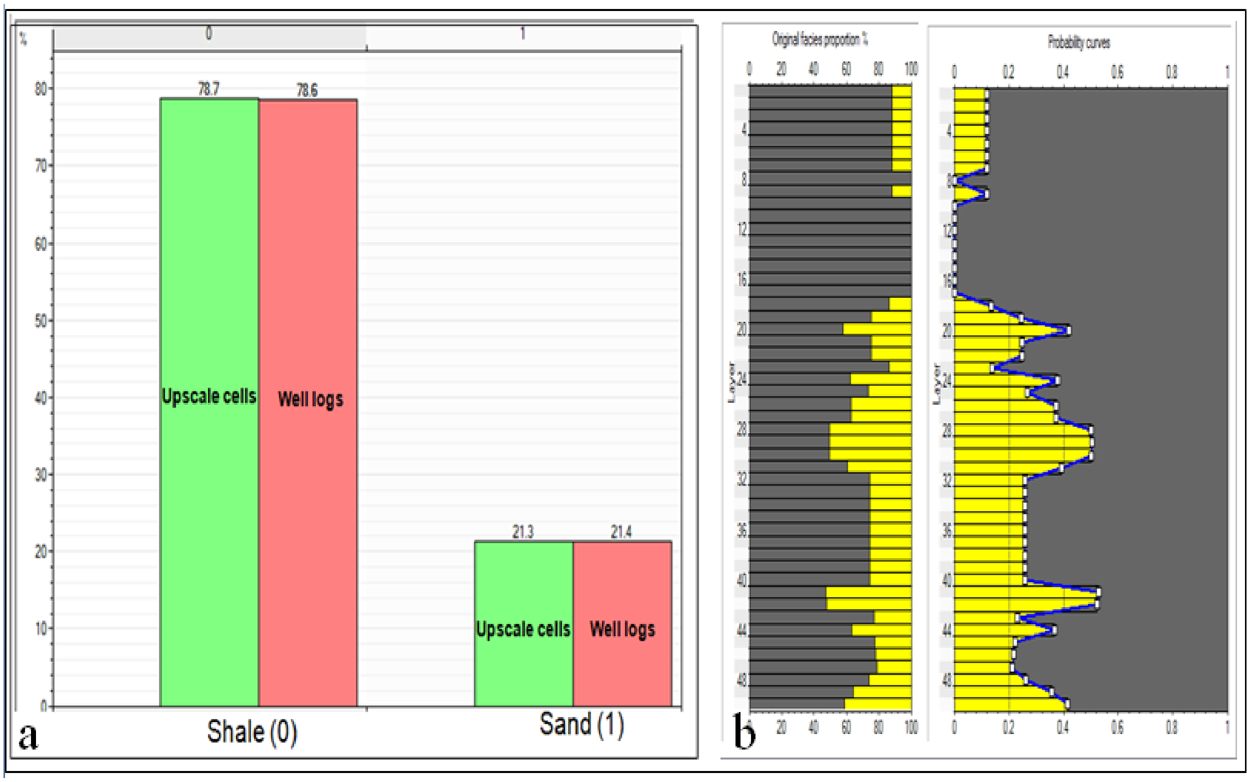

Figure 54: Global lithofacies histogram and facies proportion curve.

Table 8: Zone by zone lithofacies proportion for sand and shale from log

Zonation / Facies Proportion	Zone 1	Zone 2	Zone 3	Zone 4	Zone 5
Sand	9.46	7.99	35.31	27.11	33.68
Shale	90.54	92.01	64.69	72.89	66.32

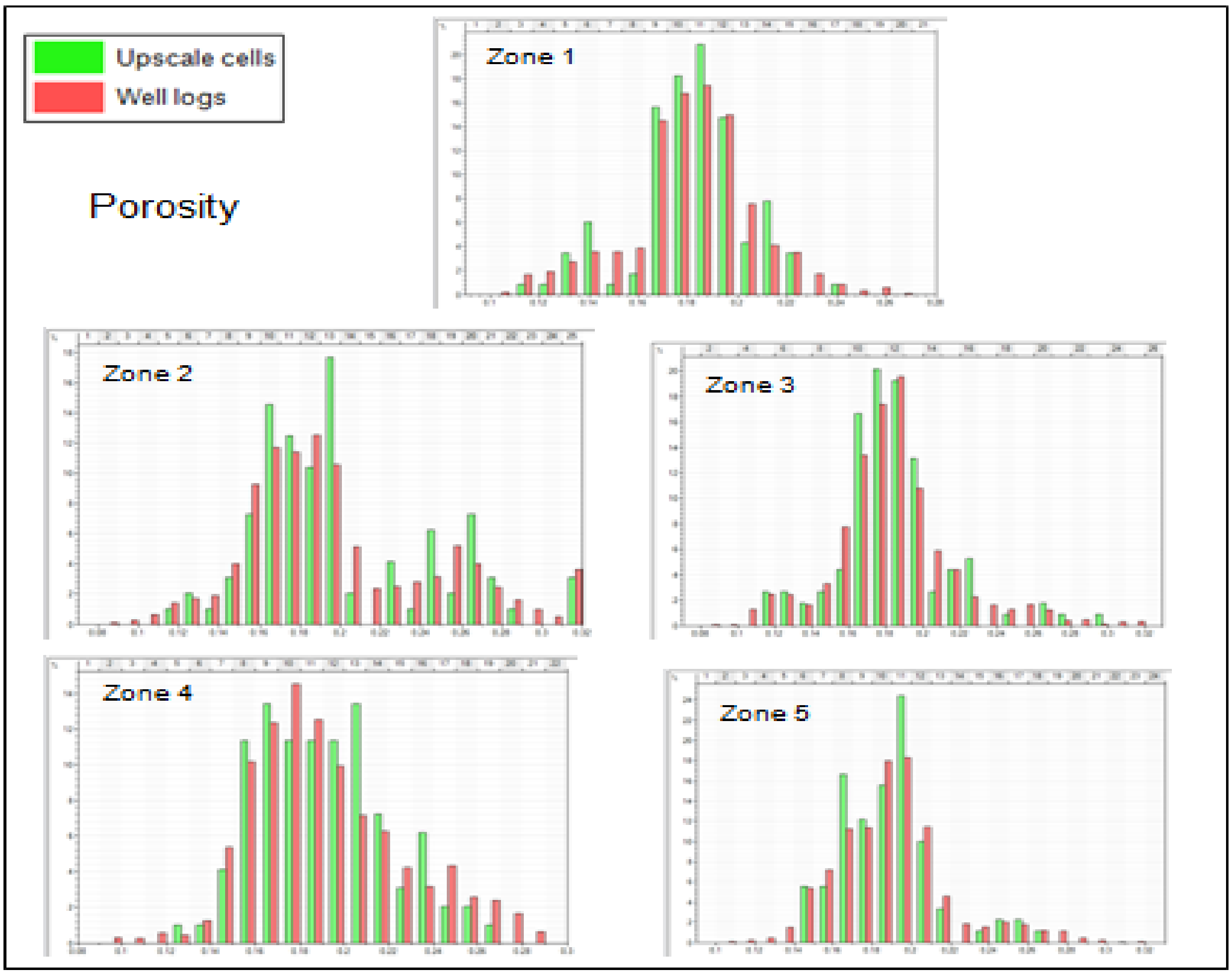

Figure 55: Zone by zone porosity histogram from well log

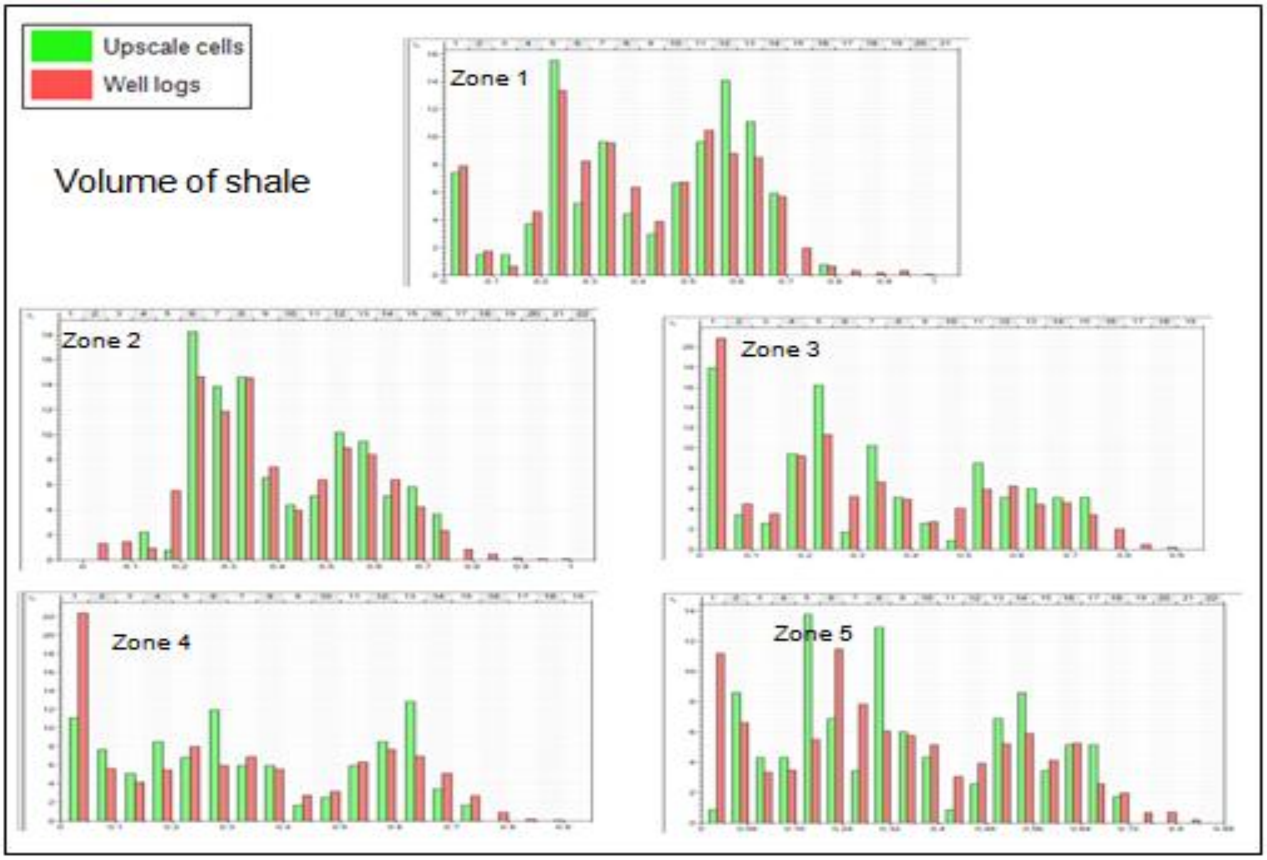

Figure 56: Zone by zone volume of shale histogram from well log

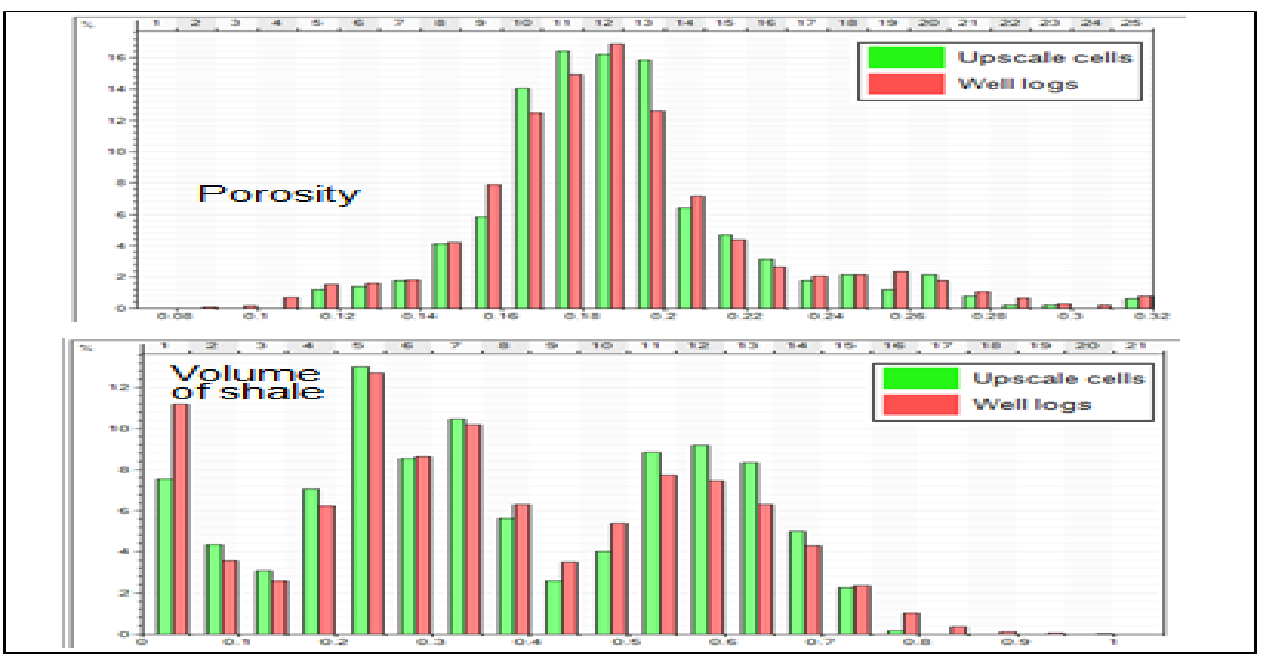

Figure 57: Global porosity and volume of shale histogram from well log

4.6.2 Indicator Kriging and Lithofacies Model

Figures 58 and 59 show the results of geostatistical facies model using indicator kriging algorithm.

The lithofacies model consists of sandstone lenses interspersed in background shale.

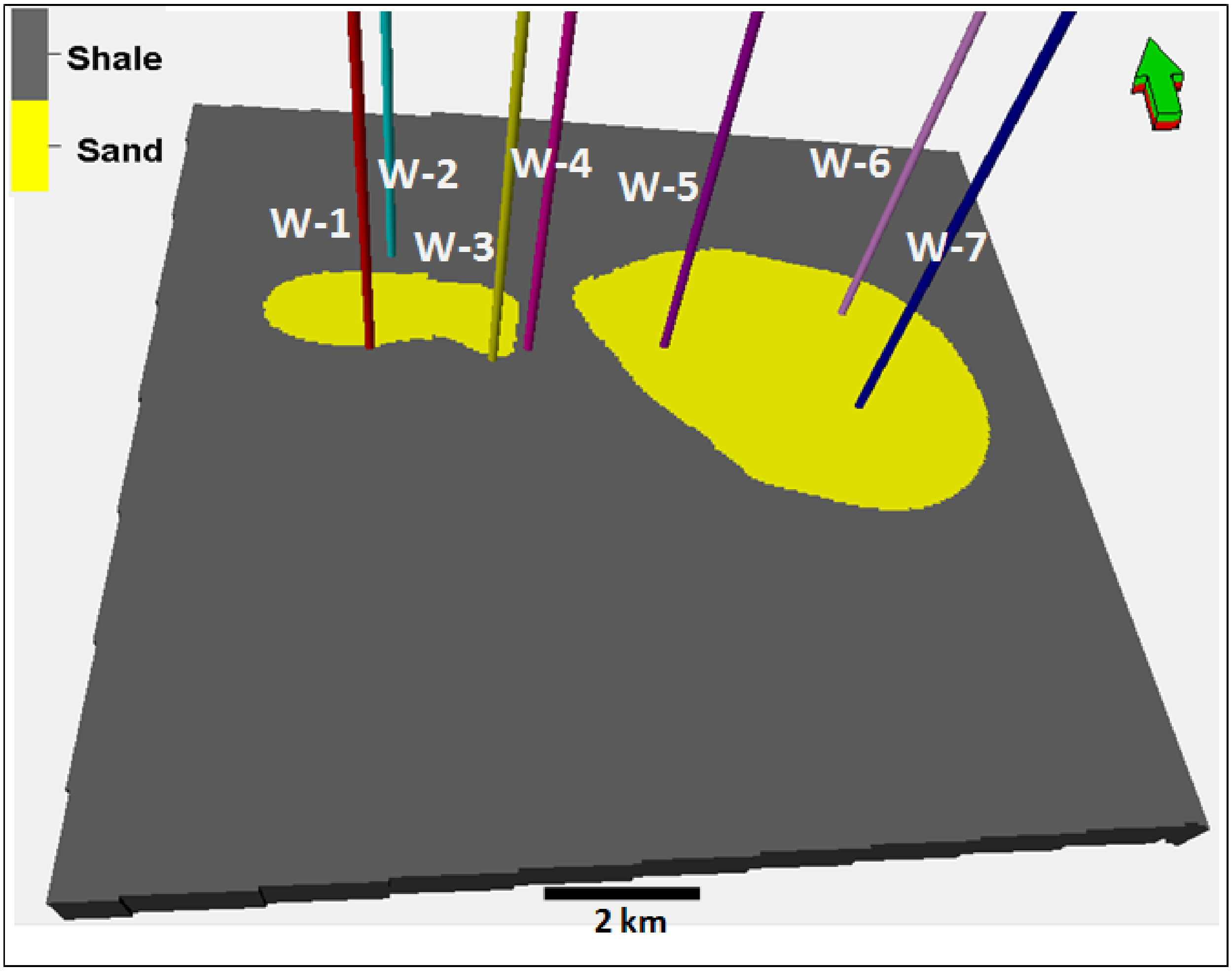

Figure 58: Zone 1 lithofacies model using indicator kriging algorithm

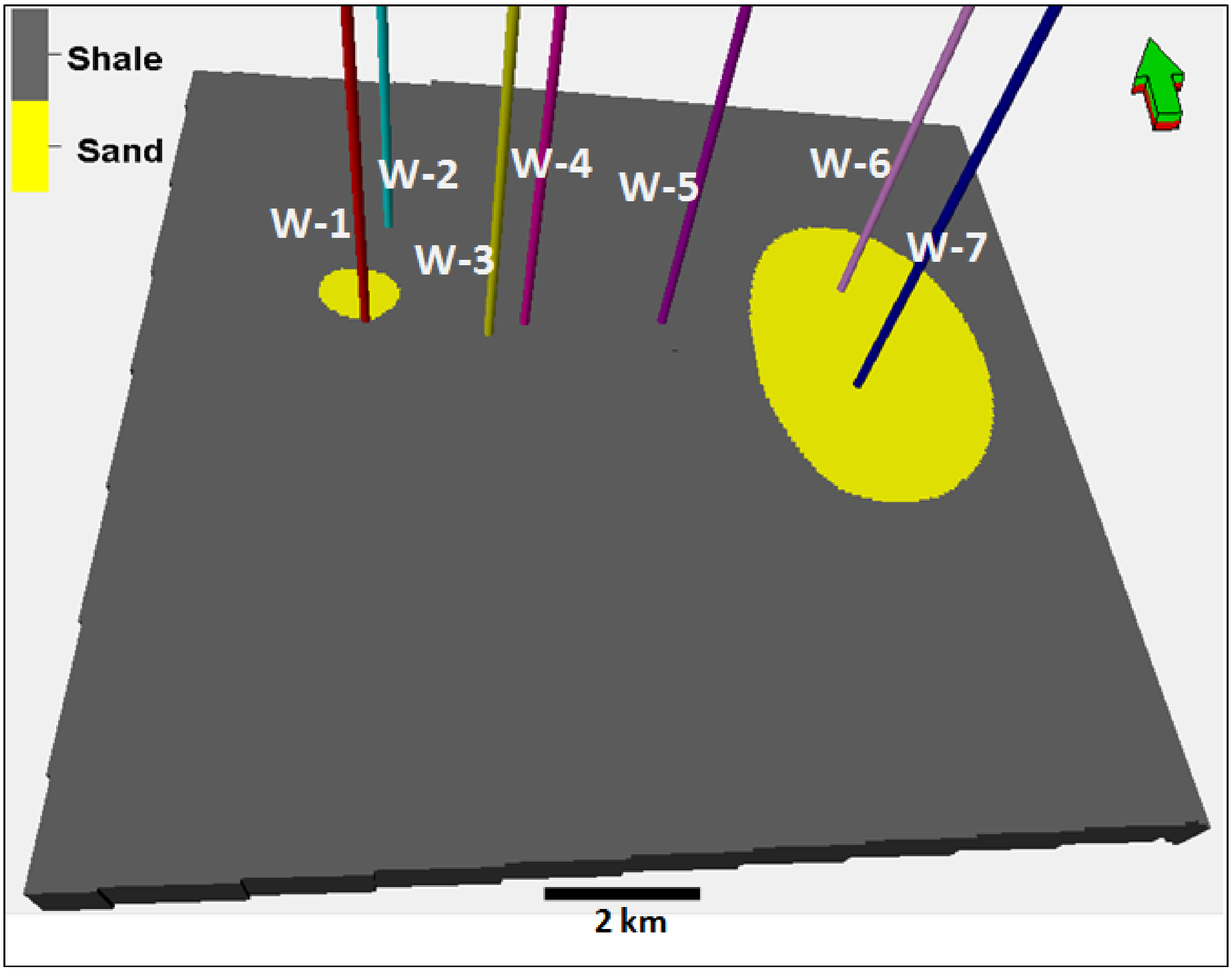

Figure 59: Zone 2 lithofacies model using indicator kriging algorithm

4.6.3 Sequential Indicator Simulation and Lithofacies Model

Figures 60 to 62 show the lithofacies models using sequential indicator simulation. Each facies realization result differs in facies distribution and architecture for every zone. This implies a high uncertainty in facies prediction outside the sampled well locations.

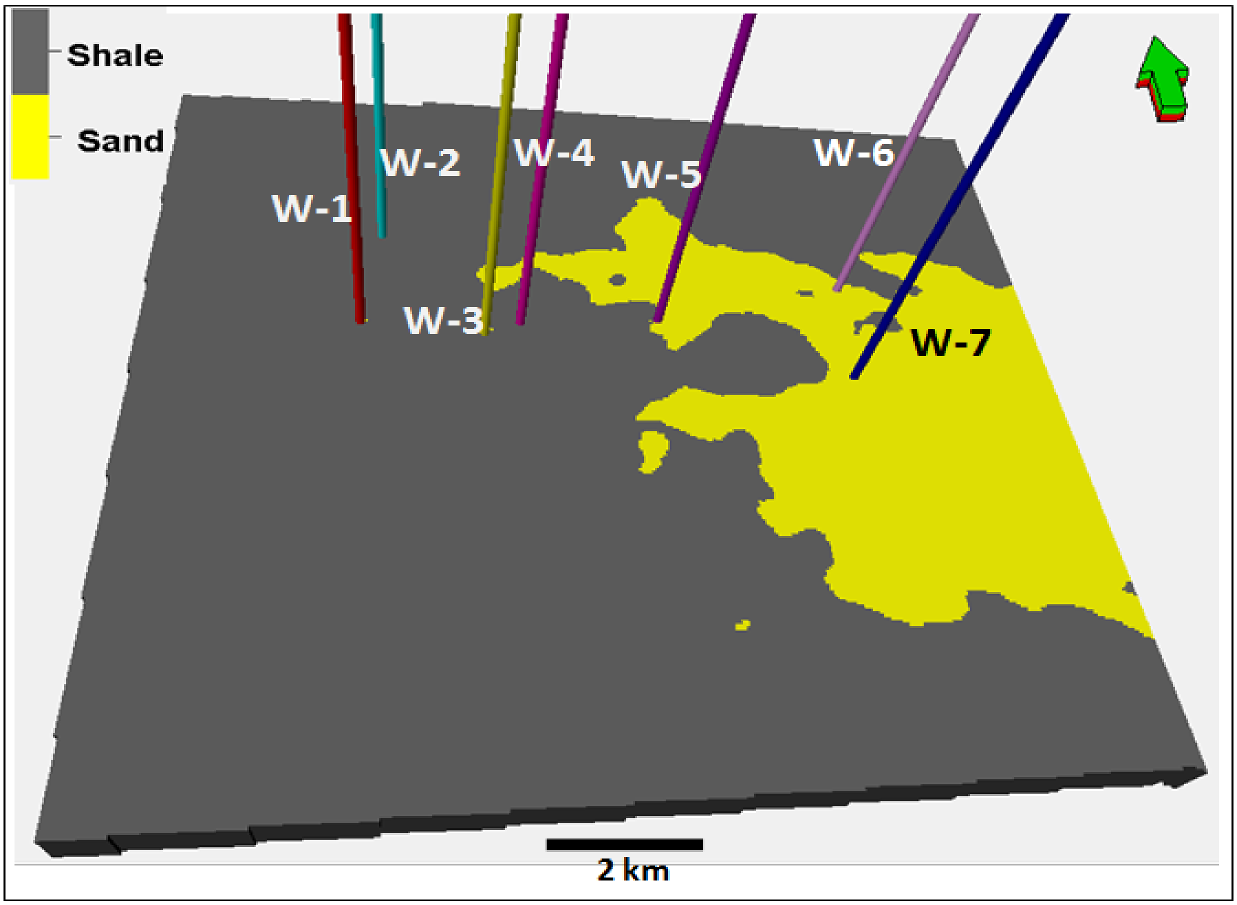

Figure 60: First realization of lithofacies model using SIS

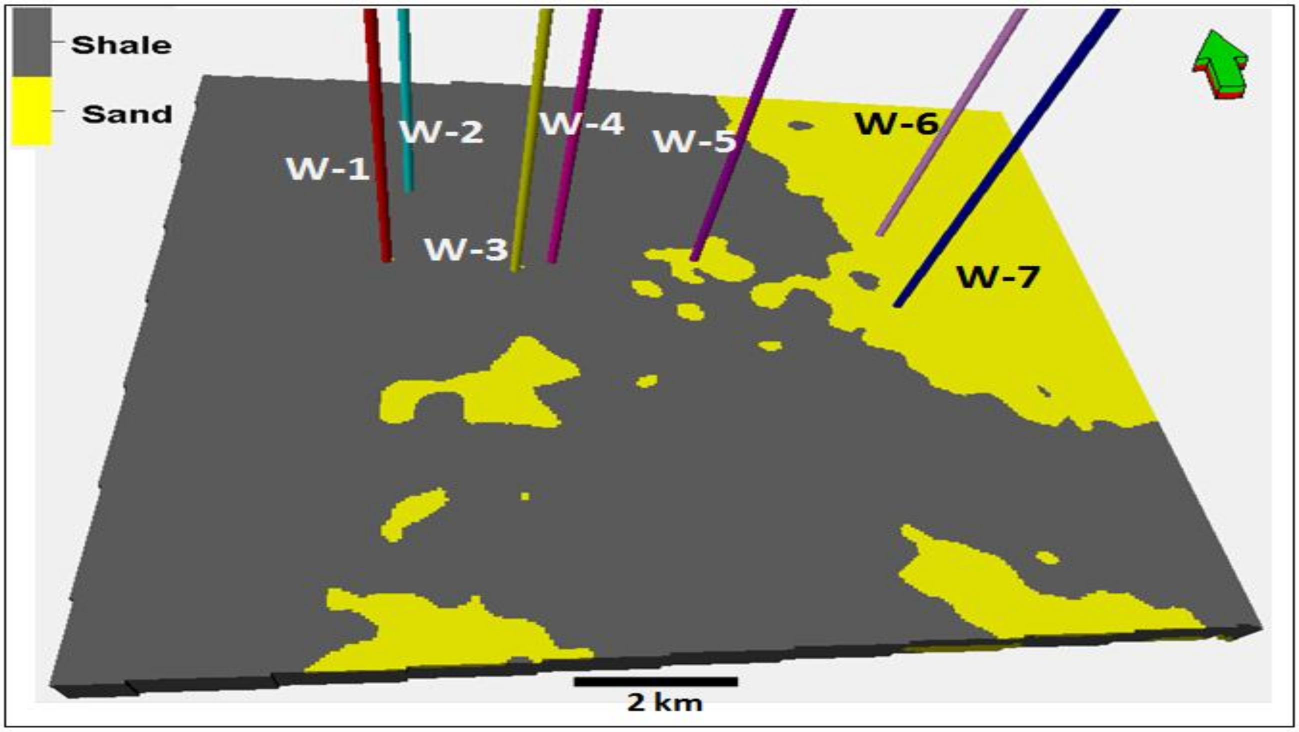

Figure 61: Second realization of lithofacies model using SIS

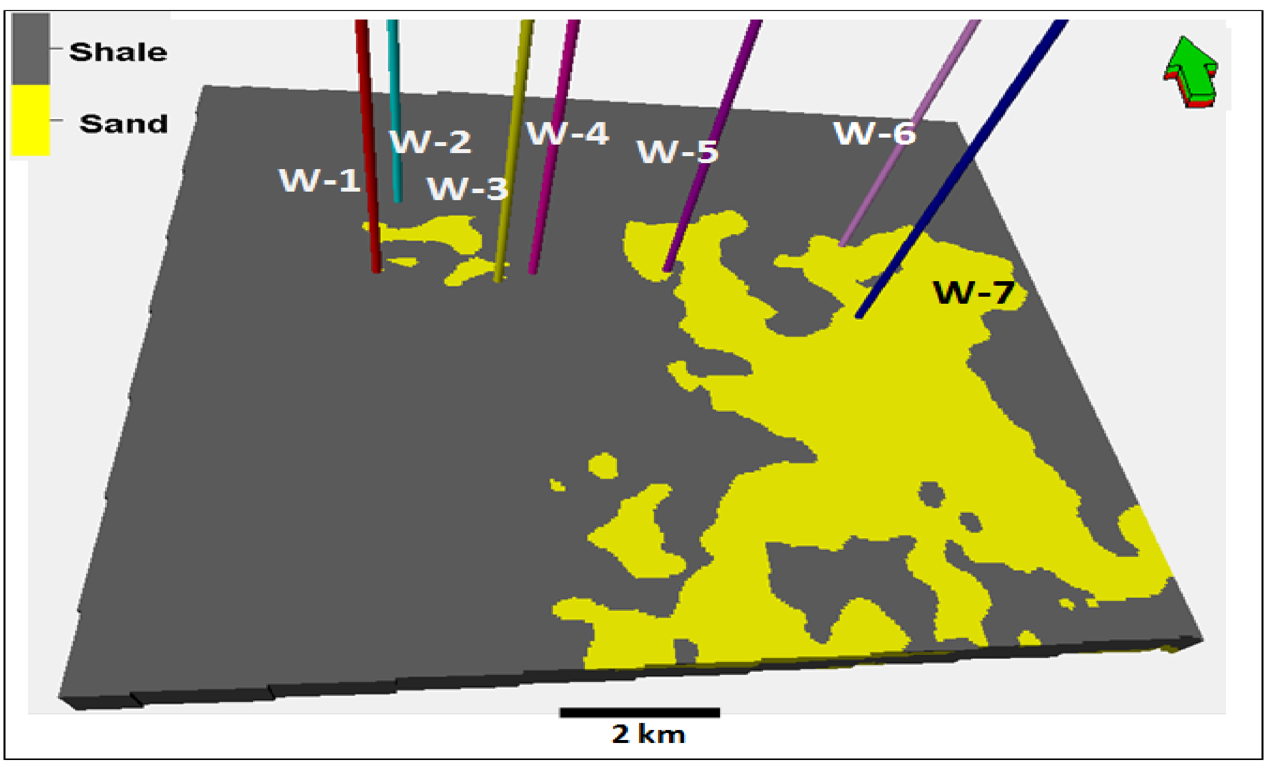

Figure 62: Third realization of lithofacies model using SIS

4.6.4 Truncated Gaussian Simulation and Lithofacies Model

The lithofacies models for truncated Gaussian simulation with trend and without trend are shown in Figures 63 and 64. The facies are characterised by smooth transition from sand to shale laterally. The facies model honours the well data but produce unrealistic morphological pattern. The algorithms used give different facies distribution and architecture for every realization, resulting to non-unique geobodies in the study area.

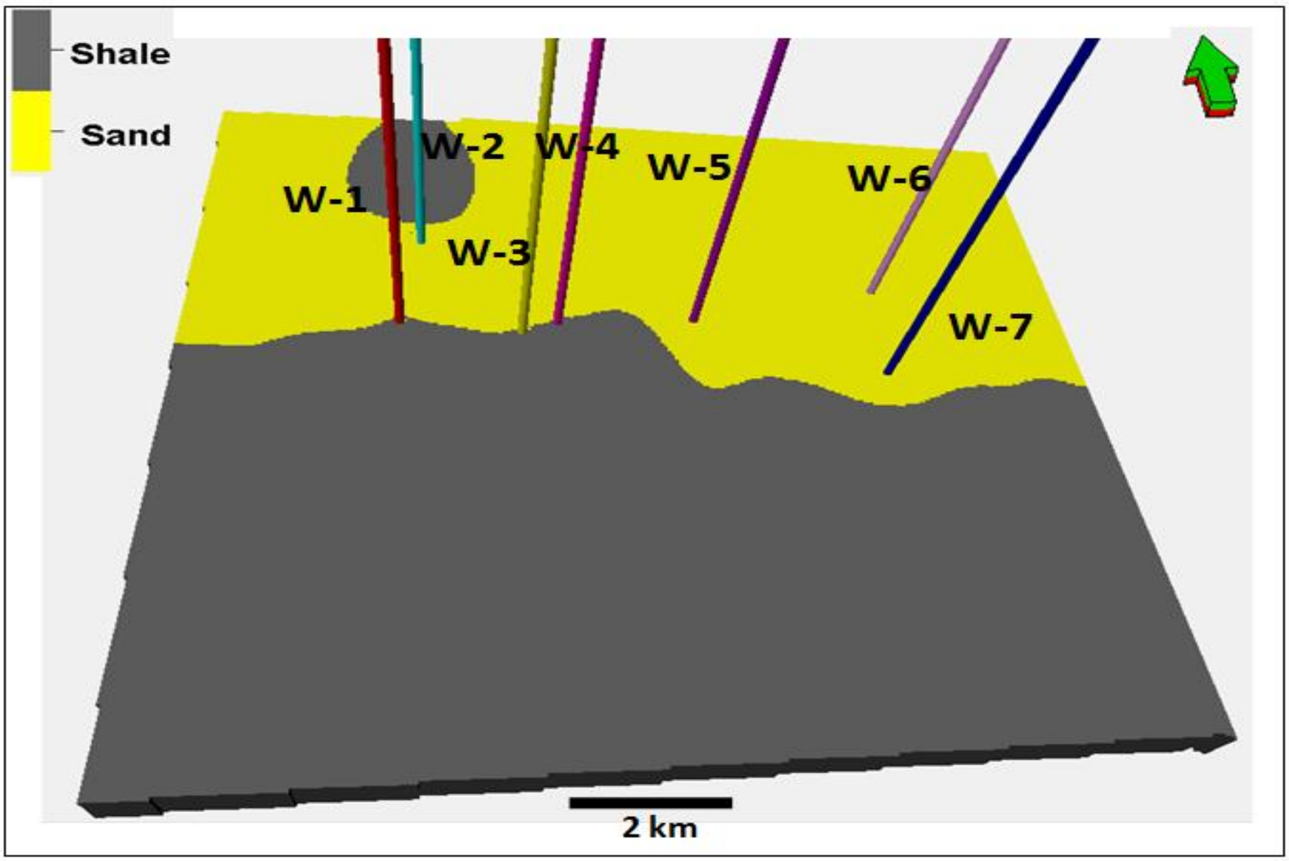

Figure 63: Lithofacies model using truncated Gaussian simulation with trend

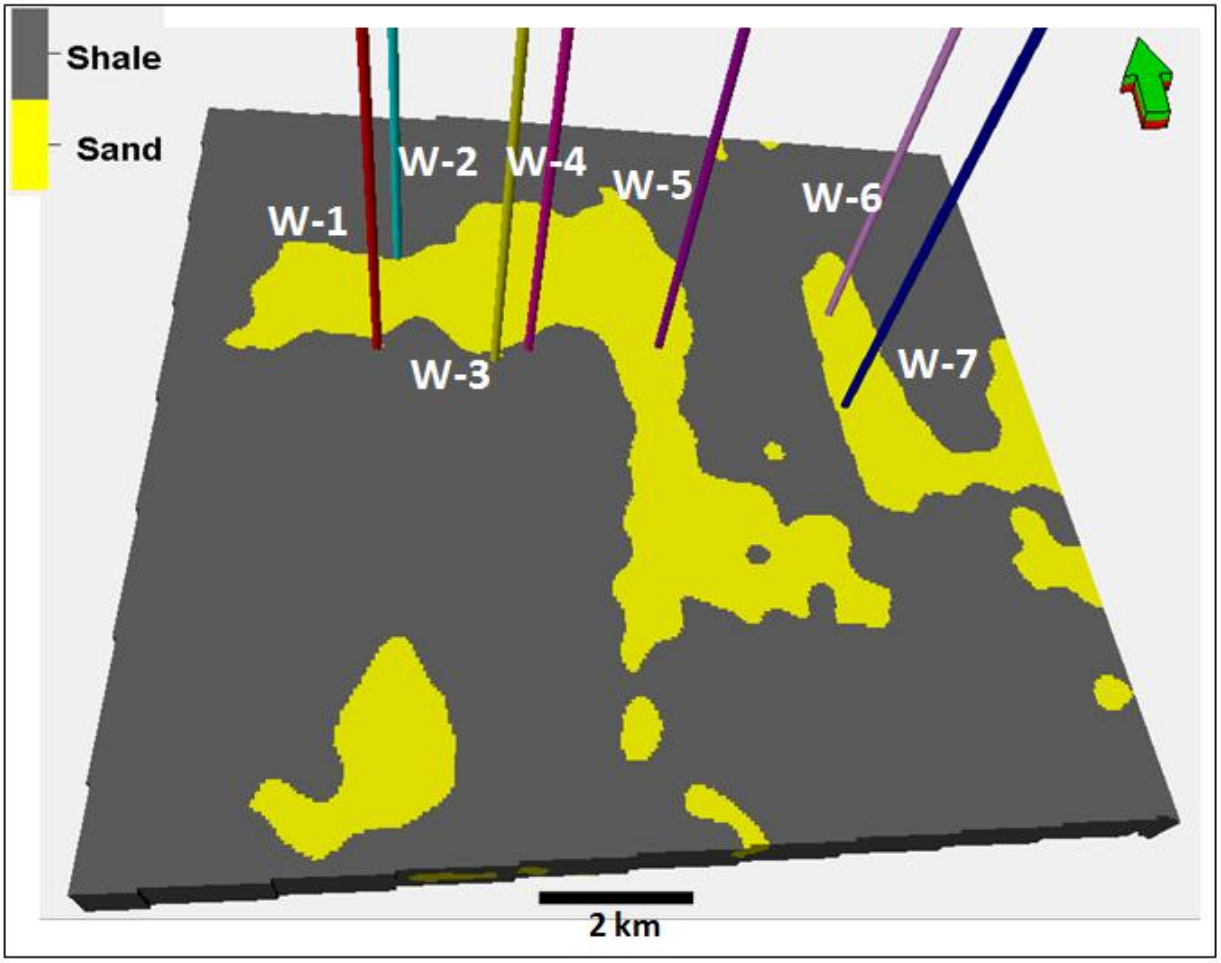

Figure 64: Lithofacies model using truncated Gaussian simulation without trend

4.6.5 Object-Based Lithofacies Model

Table 9 shows the geometrical parameters used for the object-based facies modeling in the study area. These parameters were adapted from the near sea floor channel geometry in Figure 35, page 85.

The object-based facies modeling techniques resulted in four set of north-south trending sand-fill sinuous channels as shown in Figures 65 and 66. The morphology and architectural geometry of the channel sands differ slightly for each simulation run (Figure 66). With slight changes in the geometrical parameters in Table 9, significant variability in facies geometry was observed.

Table 9: Zonal object-based modeling geometrical measurements

Statistic / Parameter	Minimum	Mean	Maximum
Orientation (^{0})	0	0	0
Amplitude (m)	500	700	900
Wavelength(m)	2200	2500	2700
Channel width (m)	500	1000	1700

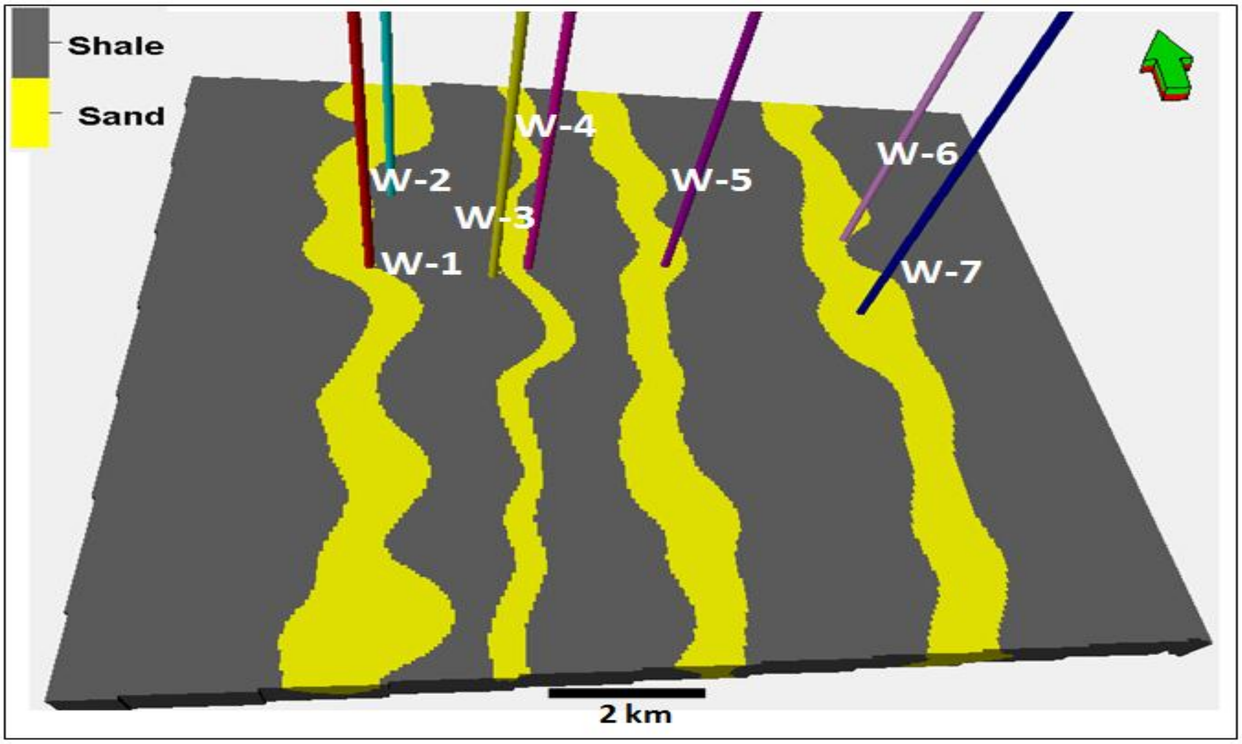

Figure 65: First realization of Channel-sand facies distribution and morphology

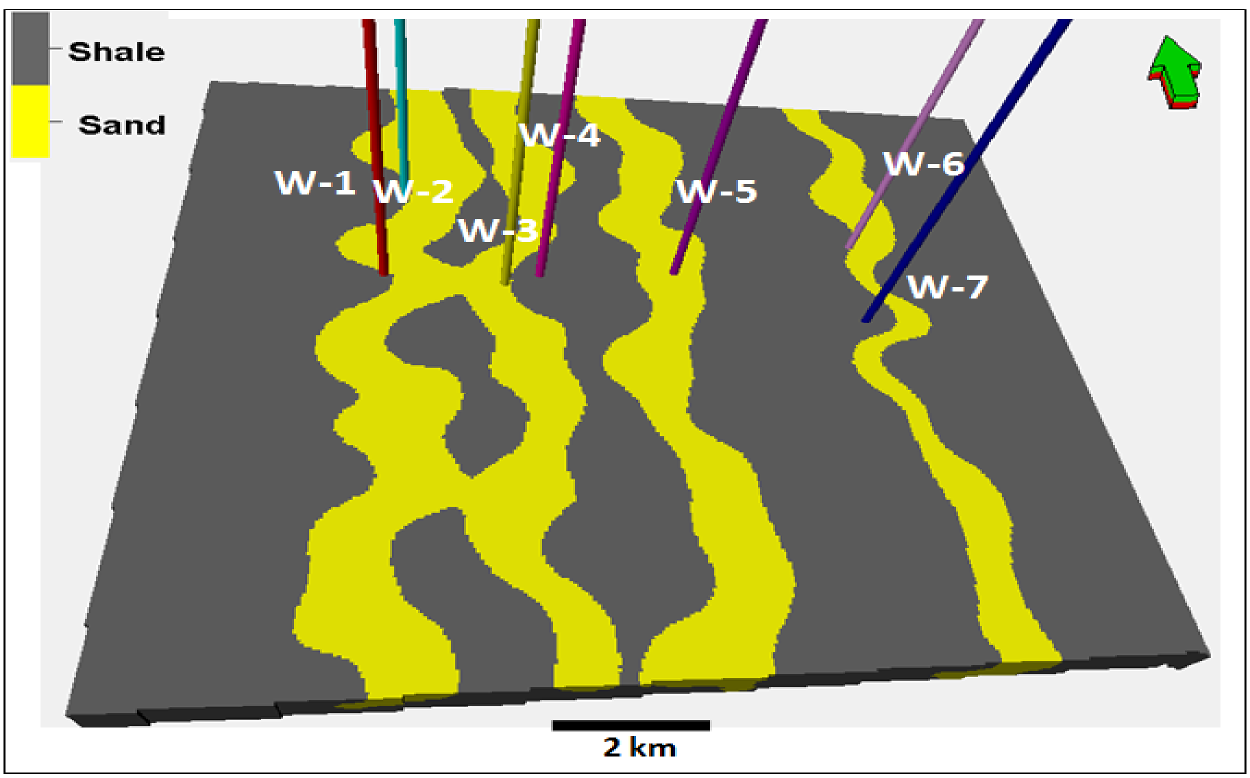

Figure 66: Second realization of Channel-sand facies distribution and morphology

4.6.6 Seismic Attributes and Multiple-Point Geostatistical Facies Model

Figures 67a, 67b and 67d show discrete seismic facies classes and facies probability respectively. The high seismic facies probability corresponds to facies code (1) with lobate architectural elements. Facies code (0) represents the background facies and was used with facies code (1) as training image for the multiple-point facies modeling of sand and shale lithofacies in this study. Figure 68 reveals sand lobes interspersed in background shale.

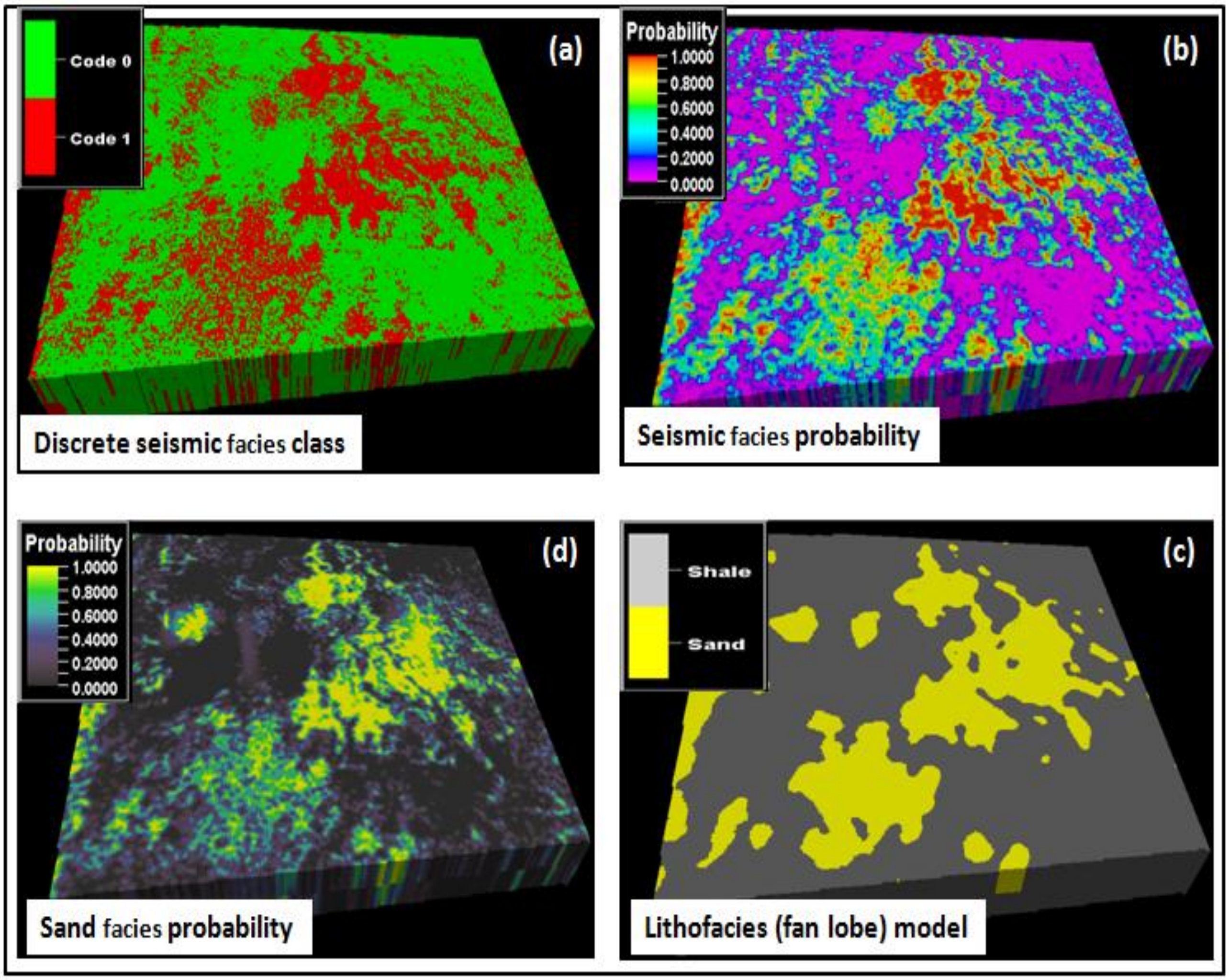

Figure 67: Seismic facies classes and facies probability as training image for multiple point geostatistical facies modeling

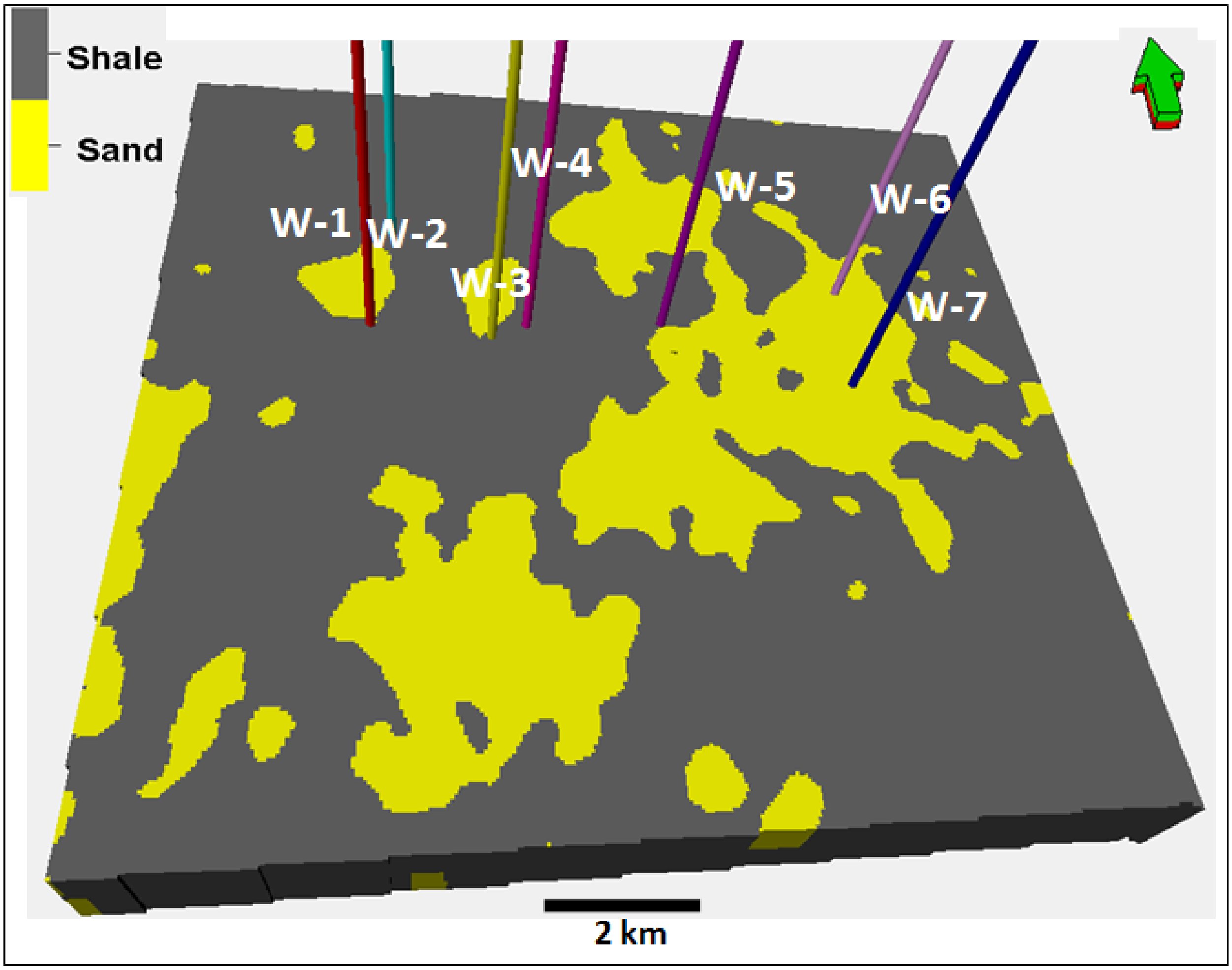

Figure 68: Deepwater fan sand model using seismic attributes as training image for multiple point geostatistical technique.

Figure 69 shows seismic derived sand probability used as training image for the multiple point geostatistical modeling of the reservoir interval. The resultant lithofacies model is characterised by lobate and curvilinear sand bodies distributed as isolated geobodies within background shale (Figure 70). The geobodies are modeled as lobes and sinuous channel sands.

Figures 71 and 72 show porosity and shale volume property models biased to the lithofacies model by assigning upscaled petrophysical properties to the sand probability through trend modeling. The volume of shale within the model ranges between 0.05 and 0.2 in the isolated sandstone facies. The background shale generally have volume of shale greater than 0.2. The distributed porosity ranges between 0.20 and 0.36 in the sand bodies, while the background shale is characterised by porosity values between 0.08 and 0.20.

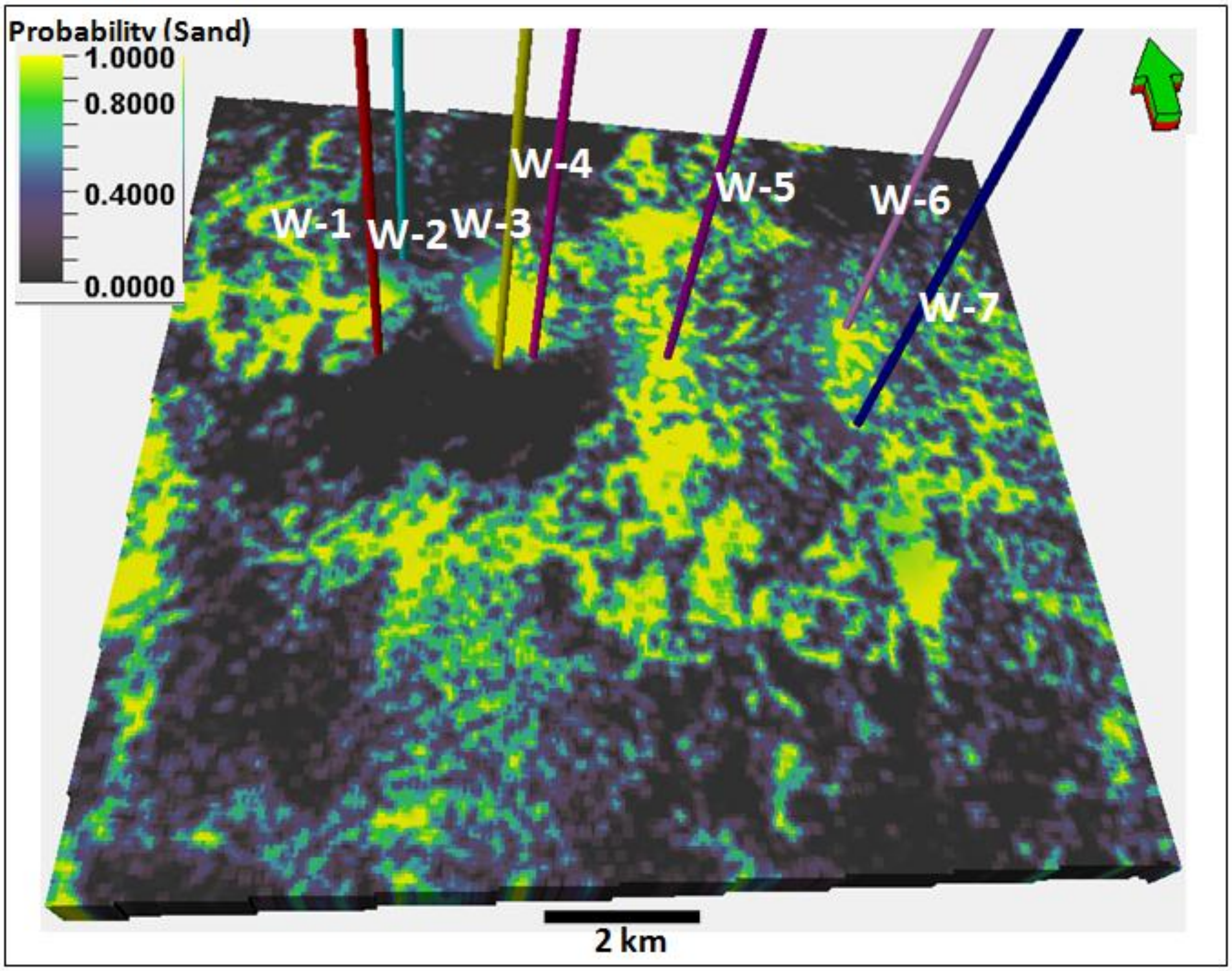

Figure 69: Sand facies probability property grid

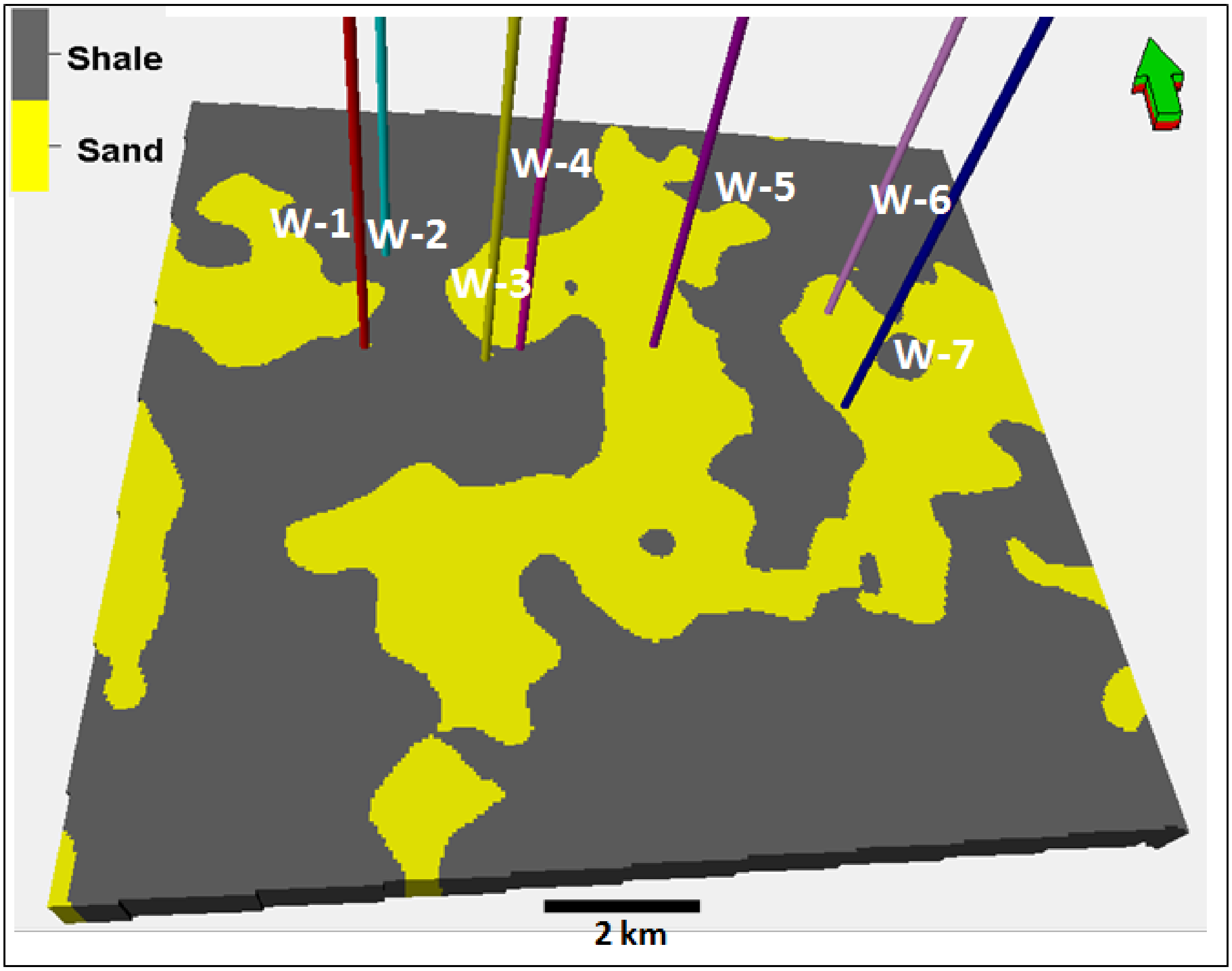

Figure 70: Deepwater channel lithofacies models

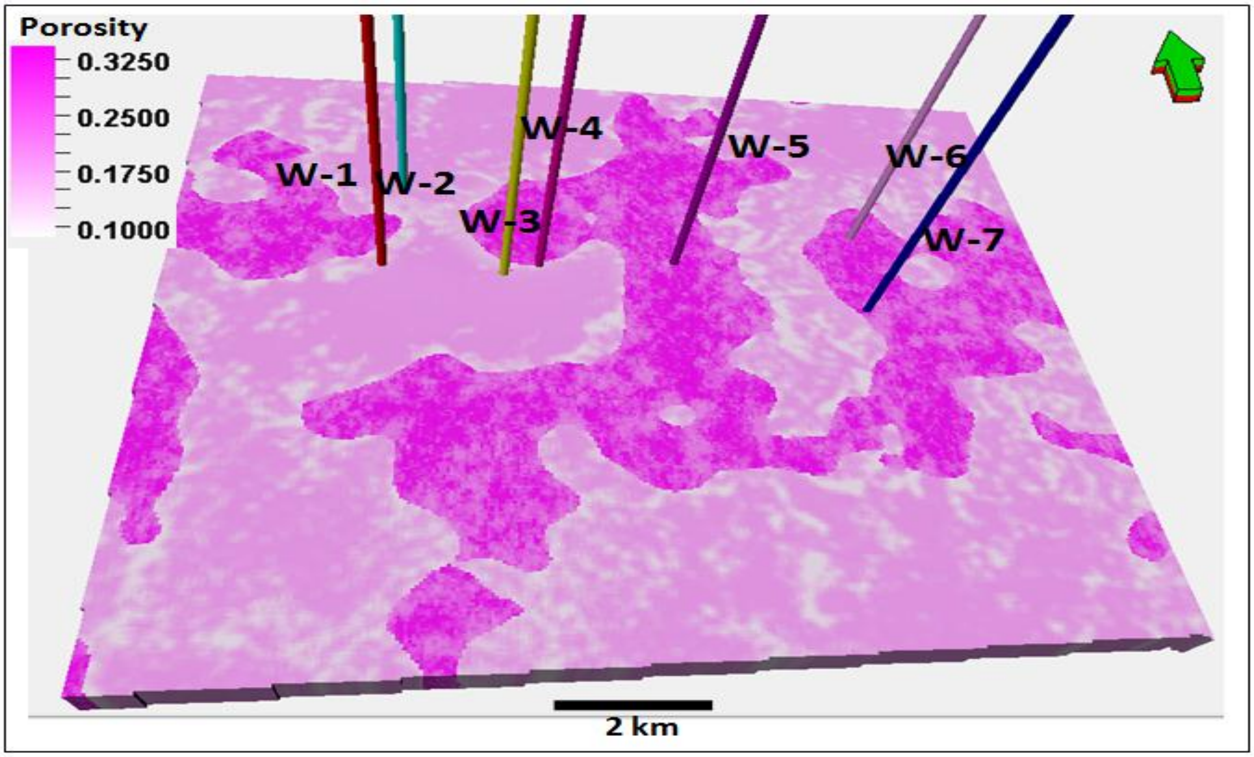

Figure 71: Seismic attribute constrained Porosity models

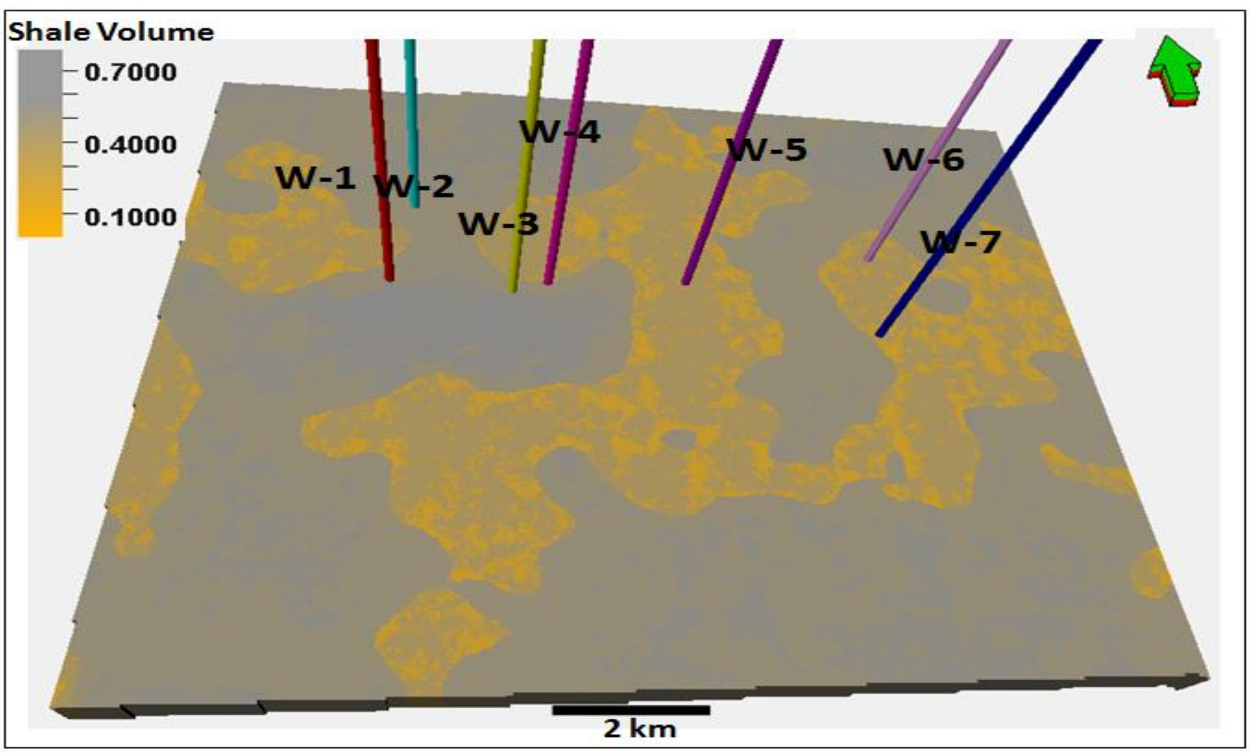

Figure 72: Seismic attribute constrained Volume of shale models

4.7 DISCUSSION OF RESULTS

4.7.1 Well Log and Petrophysical Properties

Qualitative analysis of the available suite of wireline logs as shown in Figure 13 revealed two main lithofacies types which are interpreted as sandstone and shale respectively. The relatively low readings and log separation between the primary and shear sonic pair is indicative of under-compaction due to rapid deposition of overlying sand units. This result agrees with the phenomena of rapid sedimentation of clastics on over-pressured Akata Formation as earlier proposed by Avbovbo, *et al.* (1978).

The sandstone lithofacies characterised by cylindrical and fining upward gamma ray log motifs, are interpreted to represent amalgamated deepwater channel-lobe systems. The inferred depositional systems corresponds to Rider (1996) interpretation of deepwater channel sands. The cylindrical log motifs represents amalgamated channel systems where the finer channel deposits have been eroded following each cycle of clastic deposition. While the fining upward log motif represents the classical Bouma sequence (turbidite) with coarser lag deposits at the base and finer grain sediments on top. The similarity in the gamma ray log motifs across the field as shown in Figure 14 is indicative of identical depositional facies in typical deepwater environment.

The sandstone facies are interpreted as good quality reservoirs with porosities values between 20% and 36%. The reservoir quality is similar to other deepwater Eocene to Pliocene reservoir systems reported by Shanmugam *et al.* (2006), in the Edop Field of Nigeria, Zafiro Field of Equatorial Guinea, the Grypton Field in the North Sea, Gannet Field in the North Sea, the Ewing Bank Field in Gulf of Mexico, and also in the Cenomanian-Turonian sandstone reservoirs in the Enchova and Bonito Fields in the deepwater Campos Basin of Brazil.

4.7.2 Elastic Rock Physics Properties and Seismic Lithofacies

A comparison of existing shear wave velocity equations and the empirically derived Benayol shear wave velocity equation as shown in Table 4, implies that the empirical shear wave velocity equations are basin and field specific. The Benayol equation is far more accurate in shear velocity prediction for the study area with relatively low uncertainty between -34 m/s and 80 m/s. However, the existing shear wave velocity equations by Castanga *et al.* (1985); Han *et al.* (1986) and Castagna *et al*. (1993) result in under estimation of shear wave velocities in the study area with 50% uncertainty and variance of range of -500 m/s and -1100 m/s. As shown in Figures 21 and 22, the cluster analysis of the elastic rock properties, basic reservoir properties, and petrophysical properties show distinct trend and data cloud on cross plots. Each of the data clouds represents distinct seismic lithofacies types. Mu-rho, lambda-rho, Poisson's ratio and closure stress scalar are found to be related to lithology, porosity, pore pressure variation, stiffness and mechanical strength of siliciclastic rock units as shown in Figures 23 to 26. The shale related seismic lithofacies cluster in the lambda-mu-rho rock physics space, corresponds to relatively lower mu-rho, higher closure stress scalar and Poisson's ratio. This is indicative of low stiffness and possible over-pressure in the shale. In contrast, the sandstone lithofacies is characterised by relatively higher mu-rho, lower Poisson's ratio and lower close stress scalar. This implies high rock stiffness and relatively lower rock compressibility. In Figure 18, there is a direct relationship between lambda-mu-rho trend, close stress scalar, sonic compaction trend, porosity and lithology contrast. The shale units are characterised by relatively high sonic interval transit-time at depth which corresponds to higher closure stress scalar and lambda-rho response respectively. This is interpreted as under-compacted and over-pressured shale which is supported by having porosity as high as 20%. There is an intrinsic overlap of compressional wave velocity between sand and shale in the primary velocity versus porosity versus close stress scalar cross plot in Figure 22. Hence, sandstone and shale lithofacies exhibit similar acoustic impedance values in the study area. This means acoustic impedance is not discriminatory of lithofacies in the study area. This is validated by the low correlation coefficients of acoustic impedance versus elastic rock properties in Table 5.

4.7.3 Spectral Analysis and Well-to-Seismic Correlation

The dominant frequency of 50 hertz and tuning thickness of 17 m estimated between 2.6 and 4.0 seconds as shown in Figure 26, implies that sand bodies in the analyzed interval with bed thickness less than 17 m will not be properly resolved on the available seismic data. Below the dominant frequency of 50 Hertz as seen in the seismic amplitude spectrum (Appendix C), there is the possibility of destructive interference from sand interbeds and their boundary layers. Destructive interference is the condition where the signal reflections from interbedded units cancel each other. This phenomenon is very critical in the prediction of thin bedded heterolithic sheet sand deposits in deepwater environments. This is important as some hydrocarbon sands in the deepwater environments, 5 m to 10 m thick can stretch over large lateral extent (Shanmugam, 1998). Figure 28 shows a poor synthetic-to-seismic correlation between 3330 m and 3350 m depth interval where the sand is below the tuning thickness of the seismic data. The inability to detect thin beds on seismic amplitude sections can be attributed to different factors including: sedimentary bed thickness, sand-shale ratio, burial depth, seismic acquisition and processing parameters, and seismic data quality (Avseth *et a*l., 2005). Hence, seismic attributes strata classification have been employed to capture reservoir units within the detection limits of the seismic data below 10 m thickness.

4.7.4 Seismo-structural and Seismic Stratigraphic Interpretation

The preliminary mapping and seismic attribute analysis of the sea bed and near-surface reflectors as shown in Figure 34 and 35 reveal sinuous channel systems and depositional fan architecture. Figure 29 shows the sea bed map with bathymetric range between 1300 m and 1700 m. This bathymetric depth range coincides with the mud diapir, inner fold and thrust belts of the deepwater Niger Delta, subdivided by Corredor *et al*. (2005). The observed sea bed features and near-surface geobodies represent a continuous evolution of deepwater channel and fan systems dispersed in background mud in the recent time. These recent deposits and sea floor features constitute excellent analog for the analysis and prediction of deepwater facies on seismic at deeper subsurface intervals. Generally as seen in Figures 35 and 37, the channel and fan lobe architecture indicate possible lateral accretion on the variance and envelope attribute volumes respectively.

At the deeper reservoir sections, the vertical seismic sections and structural maps as shown in Figures 30 to 33 are indicative of a massive anticlinal structure with closed contours on the depth maps. This anticlinal feature is interpreted to represent massive shale diapir of the over-pressured and under-compacted Akata Formation in the Niger Delta deep offshore belts. This means that the structural evolution of the mud-prone deepwater belts is different from the onshore and shallow offshore depobelts, where the rapid deposition of sands within the parallic Agbada sequence triggers growth faulting (Evamy *et al*., 1978). Hence, the integration of rock physics and multi-attribute seismic analysis is critical for the identification of stratigraphic features and traps in the study area, while targeting massive anticlinal structures for drilling.

4.7.5 Seismic Attributes and Lithofacies Prediction

The diagnostic seismic attributes identified for lithofacies prediction, from the multi-attribute analysis of the study area as shown in Tables 5, 6 and 7 which include: envelope, reflection intensity, sweetness and RMS amplitude are characterised by lobate and curvilinear architectural facies patterns. These attributes also give high correlation between 0.66 to 0.8 when cross plotted with elastic rock properties as shown in Table 5. Sand-prone lithofacies are generally associated with high attribute values. Other seismic attributes such as instantaneous frequency and acoustic impedance gives relatively low correlation with elastic rock properties, and are unable to capture realistic architectural facies pattern. The inability of acoustic impedance to discriminate lithofacies in the study area can be attributed to the crossover of acoustic impedance between sandstone and under-compacted shale of the Akata Formation. The minimal acoustic impedance contrast between the rapidly deposited unconsolidated sands and under-compacted shale units, will result in the overlap of acoustic impedance between lithofacies on the original amplitude seismic data. This interpretation agrees with Engelmark (2000).

4.7.6 Core-based Sedimentology and Depositional Model

The presence of faint normal grading and parallel laminations in Figure 51, is indicative of possible pelagic and hemipelagic deposits. Floating mudclast and sand injectite in Figures 47 to 49 are diagnostic of mud diapirism and overpressure, typical of rapid sedimentation and slumping in deepwater environments. Laminated and contorted bedding seen in Figure 47 are interpreted as products of gravity-driven clastic re-sedimentation and rapid burial in the deepwater channel environment. The sedimentary features shown in Figures 47 to 51 are diagnostic of a range of deepwater facies, ranging from sandy debrite and slump, mass flow complexes and turbidites, typical of deepwater submarine fan and channel environments. The presence of both normal grading and inverse grading as well as mudclast and floating pebbles observed in core implies that turbidity current, debris flow, and sandy slumps contribute to the process of clastic sedimentation in the study area. Hence, the conceptual depositional model is characterised by the interplay of deepwater submarine fan and Non-fan environments (Figure 73). While the submarine fan result predominantly from turbidity current, the Non-fan environment is associated with lamina debris flow and sandy slumps. Non-fan debris tongue and lobes models were reported in the Edop Field of eastern Niger Delta, Zafiro Field of Equatorial Guinea, Norwegian-Barent Sea continental Margin, offshore North Africa, and the Gulf of Mexico (Shanmugam, 2006).

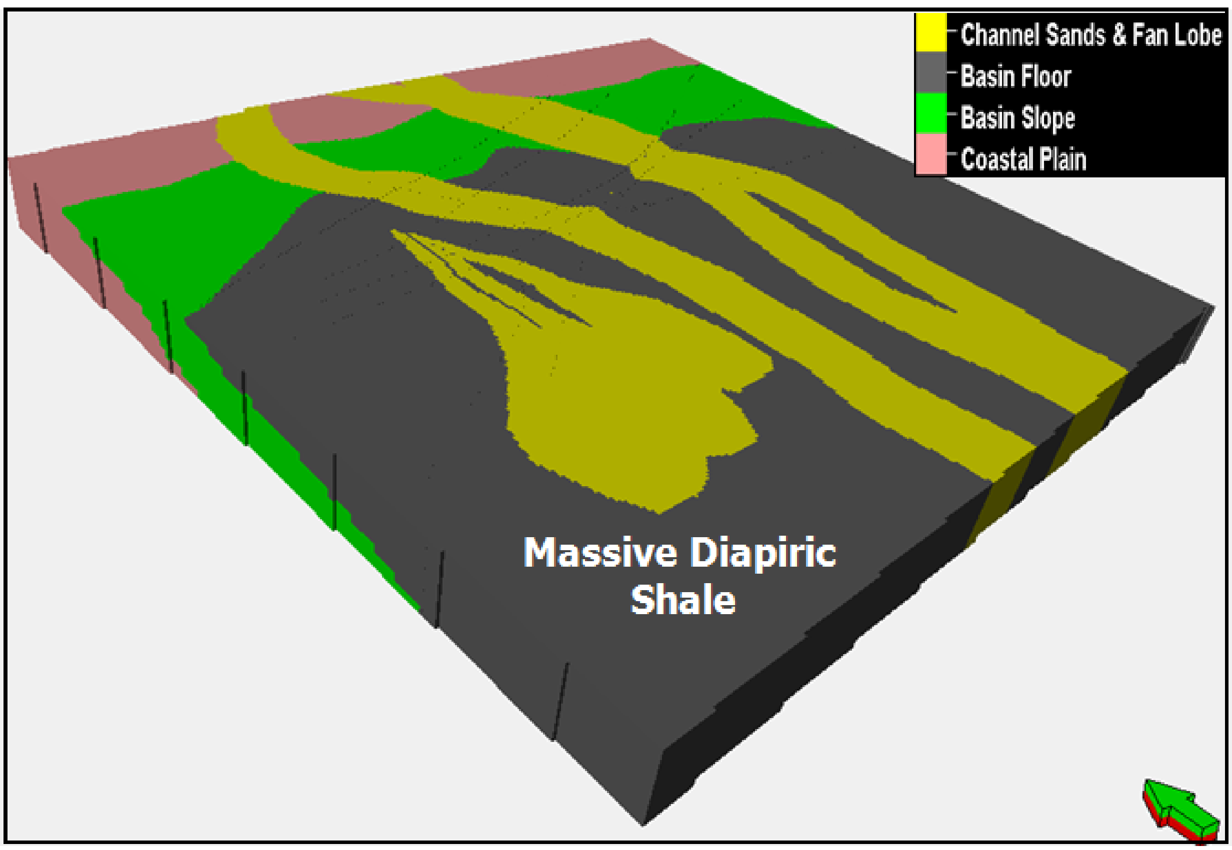

Figure 73: Mixed Deepwater fan and Non-fan conceptual depositional model in the study area

4.7.7 Geostatistical Facies Modeling Results

Geostatistical data analysis and histogram of the seven wells in Figure 53 give the lithofacies proportion of shale and sand as 79% and 21% respectively in the study area. This implies that the study area is shale-prone with isolated sandstone deposition, which corresponds with the previously published lithofacies proportion for the deepwater Niger Delta by Graue (2000). Visual inspection of modeled facies architecture between the different geostatistical algorithms including, indicator kriging, SIS, TGS and seismic attribute-based multiple geostatistical techniques (Figures 56 to 70), has revealed the use of 3D seismic attributes as most realistic in reproducing geologic pattern in geometrically complex depositional environments such as the study area. The application of 3D seismic attribute as training image for facies modeling, is more efficient than variogram and object-based facies modeling in the study area. However, this study has shown that the use of 3D seismic attribute as training image for geostatistical facies modeling depend on seismic data quality and resolvable sand thickness (Appendix C). Hence, multiple-point geostatistical facies modeling can be combined with other geostatistical methods as hybrid in order to capture sub-seismic sand thickness in well data.

CHAPTER FIVE

5.0 CONCLUSION AND RECOMMENDATION

5.1 Summary of Findings

OBJECTIVES OF STUDY	SUMMARY OF FINDINGS
1. To investigate mechanisms of deepwater sedimentation in the deepwater setting, offshore Niger Delta.	• Slumping, sliding, debris flow, turbidity current flow, pelagic and hemipelagic settling constitute mechanism of deposition in the deepwater setting of Niger Delta.
2. To characterise and identify the depositional model for sand distribution in the study area.	• The study area is characterised by a mixed depositional model comprised of turbidity current and debris flow models There is interplay of turbidite fan, debris flow tongue/lobes and sinuous channel sands
3. To identify deepwater reservoirs and discriminate their elastic rock physics properties.	• Deepwater reservoirs in the study area include, turbidite sands, channel sands and debrite lobe and tongues. The reservoirs have relatively high stiffness, high rigidity modulus, low Poisson's ratio and low closure stress scalar.
4. To determine the most appropriate post-stack seismic attributes for reservoir characterisation.	• The most appropriate post-stack seismic attributes for reservoir characterization in the study area are envelope, sweetness, reflection intensity and RMS amplitude.
5. To compare results of seismic attribute-based mutiple-point geostatistics with two-point variogram and object-based geostatistical techniques.	• Use of seismic attributes captured realistic fan shape, lobes and curvilinear geometry of channel sands • Variogram and object-based techniques are unable to define the architecture of turbidite , lobes and channel sands • Multiple-point geostatistics using seismic attributes offers the best solution to deepwater facies modeling in the study

5.2 Contributions to Knowledge

1. The results of this study have shown that the deepwater Niger Delta has a mixed depositional environment of turbidity current and debris flow; and not a predominant turbidity current fan or hyperpycnal models as previously reported by early workers.
2. This study has shown that the use of seismic attribute as training image for multiple-point geostatistical facies prediction is far more effective than variogram and object-based geostatistical methods in geometrically complex depositional environment like the deepwater Niger Delta.
3. Base on this study, a Niger Delta Basin specific and more accurate empirical Benayol shear velocity equation ($V_s = 0.919V_p - 1.140$ km/s) have been derived for the Nigerian offshore belts. This implies that empirical shear wave velocity equations are basin specific and respond to the associated sedimentation processes.
4. Benayol seismic porosity equations have been derived to estimate porosity from seismic data.
    a. **Porosity = 0.18*Reflection intensity+0.14,**
    b. **Porosity = 0.0007*Sweetness+0.047,**
    c. **Porosity =0.00015*RMSAmplitude+0.05,**
    d. **Porosity = 0.00015*Envelope+0.057**

5.3 Conclusions

1. The mechanism of deepwater deposition include gravity-driven sediment slumping, sliding, debris flow, turbidity current flow and pelagic/hemipelagic settling.
2. The depositional facies in the study area include: amalgamated turbidites and channel sands bodies deposited within background pelagic and hemipelagic shale. The sandstone deposits are underlain by local masses of diapiric shale of the Akata Formation. Sandstone and shale facies proportion in the study area are interpreted as 21% and 79% respectively. The depositional model correspond to a mixed turbidite fan and Non-fan environment.
3. The estimated reservoir and elastic rock properties indicate good quality channel-lobe sand and shale lithofacies. The correlated sands are of similar depositional facies. These include isolated fan, multiple lobes, and channel sands encased in background shale. The sandstone reservoirs have low mu-rho, Vp/Vs and Poisson's ratio, high Lambda-rho; shale volume <20% and porosity from 20 to 36%. Also, a linear relationship exist between reservoir properties and elastic rock physics properties. However, this study has shown that shear velocity estimation from empirical equations are field and basin specific. The empirical equations by Castagna *et al*. (1985); Han, *et al*. (1986); and Castagna *et al*. (1993) results in high uncertainty in shear velocity estimation in the study area.
4. Envelope, RMS amplitude, sweetness, and reflection intensity constitute the most reliable seismic attributes for facies prediction and reservoir characterisation in the study area. Porous sandstones units are associated with high seismic attributes responses as well as sinuous channel and lobate architectures. This study shows that acoustic impedance attribute is not suitable for sandstone and shale facies discrimination in the study area.

5. Among the geostatistical methods used in the study, the multiple-point geostatistical technique with seismic attributes as training image produces the best facies architecture and sand body geometry for turbidite, multiple lobes and channel sand in the study area. The other variogram and object-based modeling techniques such as SIS, TGS and the object-based model introduced unrealistic artifacts and architecture into the lithofacies model. This has resulted in inconsistent stochastic facies prediction away from well location with the traditional geostatistical methods.

5.4 Recommendations

1. High resolution broad band 3D seismic data should be used in further study of the deepwater Niger Delta to illuminate subtle channel and turbidite sand bodies.

2. Prestack seismic inversion and amplitude variation with offset (AVO) analysis should be used to compliment post stack seismic attribute studies in order to detect thin sand beds of economic importance in the study area.

3. Ocean bottom imaging should be carried in the deepwater Niger Delta belts for better understanding of the sedimentology and architectural facies pattern of recent submarine channel deposits.

References

Abreu, V., Sulivan, M., Pirmez, C., Mohrig, D. (2003). Lateral accretion package (LAPs):an important reservoir element in deepwater sinuous channels. *Marine and Petroleum Geology*, 20, 631-648.

Adeogba, A. A., McHargue, T. R. and Graham, S. A. (2005). Transient fan architecture and depositional controls from near-surface 3-D seismic data, Niger Delta continental slope: *AAPG* Bulletin, 89, 627–638.

Allen, J. R. L. (1965). Coastal geomorphology of eastern Nigeria: beach-ridge barrier islands and vegetated tidal flats: *Geologie en Mijnbouw*, 44, 1– 21.

Allen, J. R. L. (1963). Sedimentation in the modern delta of the River Niger, *West Africa: 6th Internal. Conf. Sedimentologists Proc*, 26-34.

Avbovbo, A. A. (1978). Tertiary lithostratigraphy of Niger Delta: *AAPG* Bulletin, 62, 295-300.

Avseth, P., Dvorkin, J., Marko, G., and Rykkje. (2000). Rock physics diagnostic of North Sea s ands: Link between microstructure and seismic properties. *Geophys*. Re. Lett., 27, 2761 - 2764.

Avseth, P., Mavko, G., Dvorkin, J., and Mukerji, T. (2001). Rock physics and seismic properties of sand and shales as function of burial depth. *SEG* 71st Annual meeting, Expanded Abstract.

Avseth, P., and Mukerji F. (2002). Seismic lithofacies classification from well logs using statistical rock physics. *Petrophysics*, 43, 70-81.

Avseth, P., Dvorkin, J., and Mavko, G. (2005). Quantitative seismic interpretation: Applying rock physics tools to reduce interpretation risk. Cambridge University Press. 359.

Bakke, k., Kane, I.A., Martinsen, O. J., Petersen, S. A., Johanson, T. A., Hustoff, S., Jacobson, F. H., and Groth A. (2013). Seismic modeling in the analysis of deepwater sandstone termination style. *AAPG* Bulletin, 97 (9),1395-1419.

Bjorlykke, K. (2010). From sedimentary environments to rock physics. Springer Berlin Heidelberg, 508.

Bilotti, F. and Shaw, J.H. (2005). Deep-water Niger Delta fold and thrust belt modeled as a critical taper wedge: The influence of elevated basinal fluid on structural styles. *AAPG* Bulletin, 89, (11), 1475-1491.

Burke, K. (1972). Longshore drift, submarine canyons, and submarine fans in development of Niger Delta: *AAPG* Bulletin, 56, 1975-1983.

Bustin, R. M. (1988). Sedimentology and characteristics of dispersed organic matterTertiary Niger Delta: origin of source rocks in a deltaic environment: *AAPG* Bulletin, 72, 277-298

Caers, J, Avseth P, and Mukerji T. (2001). Geostatistical integration of rock physics, seismic amplitudes, and geologic models in North Sea turbidite systems:*The Leading Edge*, 308-312.

Castangna, J.P ., Batzle, M.L. and Eastwood, R.L. (1985). Relationship between compressional-wave and shear-wave velocities in clastic silicates. *Geophys*., 50, 571-581.

Castagna, J. P., Batzle M. L. and Kan, T. K. (1993). Rock physics the link between rock properties and AVO response, in offset-dependent reflectivity. Theory and practice of AVO analysis. In, Castagna, J. P. and M. Backus. eds. Investigations in Geophysics, 8. *SEG*. 135-171.

Celik, H. (2013). The effects of linear coarse grained slope channel bodies on the orientations of fold developments: A case study from middle Eocene-Lower Oligocene Kirkgecit Formation, Elazig, eastern Turkey. *Turkish Journal of Earth Sciences*, 22,320-338.

Clemenceau, G. R., Colbert, J. and Edens, D. (2000). Production results from levee-overbank turbidite sands at Ram/Powell field, deep water Gulf of Mexico, *in* P. Weimer, R. Slatt, J. Coleman, N. Rosen, H. Nelson, A.Bouma, M. Styzen, and D. Lawrence, eds., Deepwater reservoirs of the world: Gulf Coast Section *SEPM* Foundation Bob F. Perkins 20th Annual Research Conference, 756–775.

Cobbold, P. R., B. J. Clarke and H. Loseth. (2008). Structural consequences of fluid overpressure and seepage forces in the outer thrust belt of Niger Delta. *Petroleum Geoscience*, 15, 3-15.

Cohen, H.A. and McClay, K. (1996). Sedimentation and shale tectonics of the northwestern Niger Delta front. *Marine and Petroleum Geology*, **13**, 313– 328.

Connors, C. D., Radovich, B., Danforth, A. and Venkatraman, S. (2009). The structure of the offshore Niger Delta. *Trabajos de Geologia, Universidad de Oviedo*, 29, 182-188.

Corredor, F., Shaw, J.H and Bilotti F. (2005). Structural Styles in the deep-water fold and thrust belts of the Niger Delta. *AAPG Bulletin*, 89, (6) , 753-780.

Damuth, J. E. (1994). Neogene gravity tectonics and depositional processes on the deep Niger Delta continental margin: *Marine and Petroleum Geology*, 11, (3), 320– 346.

Deptuck, M. E., Steffens, G. S., Barton, M. and Pirmez, C.(2003). Architecture and evolution of upper fan channel belts on the Niger Delta slope and in the Arabian Sea: *Marine and Petroleum Geology*, 20, 649–676.

Doust H, and Omatsola, E. (1990). Niger Delta in divergent/passive margin basins, *in J. D. Edwards and P. A. Santogrossied, eds., Am. Assoc. Petrol. Geol*. Memoir, 48: 201-238.

Duval, B. C., Cramez, C. and Vail, P. R. (1998). Stratigraphic cycles and major marine source rocks, in J. Hardenbal, J. Thierry, M. B. Farrley, T. Jacquin, P. C. de Graciansky, and P. R. Vail, eds., Mesozoic and Cenozoic sequence stratigraphy of European Basins. *Society for Sedimentary Geology (SEPM) Special Publication*, 60,43-51.

Engelmark, F. (2000). Using converted shear waves to image reservoirs with low-impedance contrast. *The Leading Edge*, 19(6), 600-603.

Evamy, B. D., Herebourne, J., Kameling, P., Knap, W. A., Molle,y F. A., Rowlands,P.H. (1978). Hydrocarbon habitat of Tertiary Niger Delta. *AAPG* Bulletin, 62: 1-39.

Frankl, E. J., and Cordry, E. A. (1967). The Niger delta oil province-recent developments onshore and off- shore: 7th World Petroleum Cong., Mexico City, Proc., 2, 195-209.

Gjelberg, J. G., T. Enoken, P. Kjaernes, O. J. Martinsen, E. Roe, and E. Vagnes. (2001). Depositional environment of the Upper Jorsalfare-lower Vale Formation (across the Cretaceous-Tertiary Boundary), at the eastern margin of the More Basin (Mid Norwegian shelf); implications for reservoir development of the Ormen Lange field:*in* O. J. Martinsen and T. Dreyer, eds., Sedimentary environments offshore Norway-Palaeozoic to Recent: *Norwegian Petroleum Society Special Publication* (10), 421-440.

Goodway, B, Perez, M., Varsek, J., and Abaco, C. (2010). Seismic Petrophysics and isotropic-anisotropic AVO methods for unconventional gas exploration: *The Leading Edge*, **29**, (12), 1500-1508.

Graue, K. (2000). Mud volcanoe in deepwater Nigeria: *Marine and Petroleum Geology* 17 (2000), 959–974.

Haack, R.C., Sundararaman, P., Diedjomahor, J.O., Xiao, H., Gant, N.J., May, E.D. and Kelsch, K. (2000). Niger Delta petroleum systems, Nigeria. *In:* Mello,M.R. and Katz, B.J. (eds) *Petroleum systems of South Atlantic margins*. *AAPG* Memoir, **73**, 213 – 2 32.

Han, D. H., Nur, A., and Morgan, D. (1986). Effects of porosity and clay content on wave velocities in sand stones, *Geophys*., 51, 2093-2107.

Hart, B. S. (2002). Validating seismic attributes: Beyond statistics:*The Leading Edge*, 21, 1016–1021.

Hart, B. S. (2008). Channel detection in 3D seismic data using sweetness:*AAPG* Bulletin,92, (6), 733–742.

Heinio, P., and Davies, R. J. (2006). Degradation of compressive fold belts, Deepwater Niger Delta. *AAPG* Bulletin, 90, (5), 753-770.

Journel, A. G. (2005). Beyond covariance: the advent of multiple-point geostatistics,O. Leuangthong and C. V. Deutsch (eds.), Geostatistics, Banff, 2004, 225-233.

Kelker, M., and Perez, G. G. (2002). Applied geostatistics for reservoir characterization: *Soceity of Petroleum Engineers*, 264.

Kirk, R. (1994). Submarin fans in Australia and New Zealand in a sequence stratigraphic framework: An overview, in P. Wiemer, A. H. Bouma, and B. F. Perkins, eds., submarine fans and turbidite systems. *Gulf Coast Section Society for Sedimentary Geology (SEPM) Foundation 15th Annual Research Conference*, 193-208.

Knox, G. J., and Omatsola, E. M. (1989). Development of the Cenozoic Niger Delta in terms of the "escalator regression" model and impact on hydrocarbon distribution, *in* W. J. M. van der Linden et al., eds., 1987 Proceedings KNGMG Symposium on Coastal Lowlands, Geology, and Geotechnology: Dordrecht, The Netherlands, Klumer Academic Publishers, 181–202.

Kostenko, O. V., Naruk, S. J., Hack, W., Poupon, M., Meyer, H., Mora-Glukstad, M., Anowai, C. and Mordi, M. (2008). Structural evaluation of column- height controls at a toe-thrust discovery, deepwater Niger Delta. *AAPG* Bulletin, 92 (12), 1615-1638.

Kulke, H. (1995). Nigeria, in. Kulke, H., ed., Regional Petroleum Geology of the world. Part II: Africa, America, Australia and Antarctica: Berlin, Gebruder Borntraeger,143-172.

Lawrence, D. T., and Bosman-Smits, D. F. (2000). Exploring deep water technical challenges in the Gulf of Mexico, *in* P. Weimer, R. M. Slatt, J. L. Coleman, . Rosen, C. H. Nelson, A. H. Bouma, M. Styzen, and D. T. Lawrence, eds., 2000, Global Deepwater Reservoirs: Gulf Coast Section *SEPM* Foundation Bob F. Perkins 20th Annual Research Conference, 473–477.

Leiphart, D. J., and B. S. Hart. (2001). Comparison of linear regression and a probabilistic neural network to predict porosity from 3-D seismic attributes in Lower Brushy Canyon channeled sandstones, southeast New Mexico: *Geophysics*, 66, 1349–1358.

Mahaffie, M. J. (1994). Reservoir classification for turbidite intervals at the Mars discovery, Mississippi Canyon 807, Gulf of Mexico, *in* P. Weimer, A.H. Bouma, and B.F. Perkins, eds., Submarine fans and turbidite systems: Gulf Coast Section-*SEPM* Foundation 15th Annual Research Conference, 233-244.

Maiti, S. and Tiwani, R. K. (2010) Automatic discriminations among geophysical signals via the Bayesian neural network approach. *Geophysics*, 75, 1: 67-78.

McGrory, R., R. Pennegar, and R. Stewart. (2006). Gas field characterization through the use of multi- resolution seismic attributes: Proceedings, Canadian Society of Petroleum Geologists–Canadian Society of Exploration Geophysicists–Canadian Well Logging Society Joint Convention, Calgary, 265.

Meyer, E. Douglas, Elizabeth L. Harvey, Terra E. Bulloch, Jennifer C. Voncannon and Tatun M. Sheffield. (2001). Use of seismic attributes in 3-D geovolume interpretation, *The Leading Edge*. 1377-1380.

Morgan, R. (2003). Prospectivity in ultra deep water: the case for petroleum generation and migration within the outer parts of the Niger Delta apron. *In:* Arthur, T.J., McGregor, D.S. and Cameron, N.R. (eds) *Petroleum Geology of Africa: new themes and developing technologies*. Geological Society, London, Special Publications, 207, 151–164.

Mulder, T. and Chapron, E. (2011). Flood deposits in continental and marine environments: character and significance, in: Sediment transfer from shelf to deep water - Revisiting the delivery system, AAPG Studies in Geology, 61, edited by: Slatt, R. M. and Zavala, C., 1–30.

Mutti, E. and Normark, W. R. (1987). Comparing examples of modern and ancient turbidite systems: problems and concepts, *in* J. K. Leggett, and G. G. Zuffa, eds.,*Marine clastic sedimentology*: Graham-Trotman, London, 1-38.

Mutti, E. and Normark, W.R. (1991). An integrated approach to the study of turbidite systems, *in* P. Weimer, and M. H. Link, eds, Seismic facies and sedimentary processes of submarine fans and turbidite systems: Springer Verlag, New York, 75-106.

Mutti, E., G. Davoli, R. Tinterri, and C. Zavala. (1996). The importance of ancient fluvio-deltaic systems dominated by catastrophic flooding in tectonically active basins: *Journal of Geological Science*, 48, 233 - 291.

Murat, R. C. (1972). Stratigraphy and paleogeography of the Cretaceous and lower Tertiary in southern Nigeria, *in African geology*; Cretaceous rocks of Nigeria and adjacent areas: Ibadan, Nigeria, Ibadan Univ., Dept. Geology, 251-265.

Nwachukwu, J. I. and Chukwura, P.I. (1986). Organic matter of Agbada Formation, Niger Delta, Nigeria. AAPG Bulletin, 70, 48-55.

Ofurhie, M. A., Agha, G. U., Lufadeju, A. O. and Ineh, G. C. (2002). Turbidite depositional environment in deepwater of Nigeria. *Offshore Technology Conference*, 14068.

Oomkens, E. (1974). Lithofacies relations in the Late Quaternary Niger delta complex: *Sedimentology*, 21, 195-222.

Peters, K. E., Snedden, J. W., Sulaeman, A., Sarg, J. F. and Enrico, R. J. (2000). A new geochemical–sequence stratigraphic model for the Mahakam Delta and Makassar slope, Kalimantan, Indonesia: *AAPG* Bulletin, 84, 12–44.

Pettingill, H. S. (1998). Worldwide turbidite exploration and production: a globally immature play with opportunities in stratigraphic traps: paper *SPE* 49245, 1998 *SPE* Annual Convention.

Pettingill, H. S., and Weimer, P. (2001). Global deep water exploration: past, present and future frontiers: *in* R. H. Fillon, N. C. Rosen, P. Weimer, A. Lowrie, H. W. Pettingill, R. L. Phair, H. H. Roberts, and B. Van Hoorn, eds., 2001, Petroleum systems of deepwater basins: global and Gulf and Mexico experience: Gulf Coast Section *SEPM* Foundation Bob F. Perkins 21st Annual Research Conference, 1–22.

Pettingill, H. S., and Weimer, P. (2002). Global Deep Water Exploration: Past, Present and Future Frontiers: *The Leading Edge*, 21, 371–376.

Posamentier, H. W., Erskine, R.D. and Mitchum, R. M. (1991). Submarine fan deposition within a sequence stratigraphic framework, in Weimer, P., and M. H. Link. eds., Seismic facies and sedimentary processes of submarine fans and turbidite systems: Springer-Verlag, New York, 127-136.

Posamentier, H. W., and Kolla, V. (2003). Seismic geomorphology and stratigraphy of depositional elements in deep-water settings: *Journal of Sedimentary Research*, 73, 367–388.

Reading, H. G., and Richards, M. (1994). Turbidite systems in deepwater basin margins classified by grain size and feeder system: *AAPG Bulletin*, 78, (5), 792– 822.

Rider, M. (1996). The geological interpretation of well logs, 2nd edition, Gulf Publishing Company Houston, 280.

Richards, M., Bowman, M. and Reading, H. (1998). Submarine fan systems: I. Characterization and stratigraphic prediction:*Marine and Petroleum Geology*, 15, 689-717.

Robertson, J. D. and Nogami, H. H. (1984). Complex seismic trace analysis of thin beds. *Geophysics*, 49 (4), 344-352.

Saugy, L. and Eyer, J.A. (2003). Fifty years of exploration in the Niger Delta (West Africa). *In:* Halbouty, M.T. (ed.) *Giant Oil and Gas Fields of the Decade1990–1999.AAPG* Memoir, 78, 211–226.

Schiefelbein, C.F., Zumberge, J.E., Cameron, N.R. and Brown, S.W. (1999). Petroleum systems in the South Atlantic margins. *In:* Cameron, N.R., Bate, R.H. and Clure, V.S. (eds) *The Oil and Gas Habitats of the South Atlantic*. *Geological Society*, London, Special Publications, **153**, 169–179.

Schiefelbein, C. F., Zumberge, J. E., Cameron, N. C. and Brown, S. W. (2000). Geochemical comparison of crude oil along the South Atlantic Margin, *in* M. R. Mello and B. J. Katz, eds., Petroleum systems of South Atlantic Margins: *AAPG* Memoir 73, 15–26.

Schultz, P. S., S. Ronen, M. Hattori, and C. Corbett. (1994). Seismic-guided estimation of log properties: Part 2. Using artificial neural networks for non- linear attribute calibration:*The Leading Edge*, 13, 674–678.

Shanmugam, G. (1992). Submarine canyons. 7th Edition of Encyclopedia of Science and Technology. Mc-Graw-Hill Book Company, New York, 548-552.

Shanmugam, G. (1998). Dimensions and geometries of the components of deep- water systems. Mobil Technology Special Publication, Dallas, Texas, 110.

Shanmugam, G. (2006). Deep-water processes and facies models: Implication for sandstone petroleum reservoirs: Elsevier, Handbook of Petroleum Exploration and Production, 5, 476.

Shew, R. D., Rollins, D. R., Tiller, G. M., Hackbarth, C. J. and White, C. D. (1994). Characterisation and modeling of thin-bedded turbidite deposits from Gulf of Mexico using detailed subsurface and analog data, *in* P. Weimer, A. H. Bouma, and B. F. Perkins, eds., Submarine fans and turbidite systems: Gulf CoastSection–*SEPM* Foundation 15th Annual Research Conference, 327–334.

Short, K. C., and Stauble, A. J. (1967). Outline of geology of Niger Delta: *AAPG* Bulletin, 51,761-799.

Stacher, P. (1995). "Present Understanding of the Niger Delta Hydrocarbon Habitat". In: *Geology of Deltas*. Oti, M.N. and G. Postma (eds). A.A. Balkema: Rotterdam, The Netherlands. 257-267.

Steffens, G. S. (1993). Gulf of Mexico deepwater seismic stratigraphy: *AAPG* Annual Meeting Abstracts with programs, New Orleans, 186.

Stevenson, C. J., Talling, P. S., Wynn, R. B., Masson, D. G., Hunt, J. E., Frenz, M., Akhmetzhanhov, A. and Cronin, B. T. (2012). The flow that left no trace:Very large volume turbidity currents that by-passed sediments through submarine channels without eroding the sea floor. *Marine and Petroleum Geology, Article in Press*, 1-20.

Stow, D. A., Johansson, M., Braakenburg, N. E and Faugeres J. C. (1999). Deepwater massive sands: facies, processes and channel geometry in Numidian Flysch. N. Sicily: *Reply Sedim. Geol*, 127, 119-123.

Strebelle, S. (2002). Conditional Simulation of Complex Geological Structures Using Multiple-Point Statistics, *Mathematical Geology*, 34, (1).

Taner, M. T., F. Koehler, and R. E. Sheriff. (1979). Complex seismic trace analysis: *Geophysics*, 44,1041–1063.

Tuttle, L.W.M., Charpentier, R.R., and Brownfield, E.M. (1999). The Niger Delta Petroleum System: Niger Delta Province, Nigeria Cameroon, and Equatorial Guinea,Africa.*U.S. Geological Survey Open-File Report 99-50-H*, Denver, Colorado, 70.

Ulrych, T. J., Sacchi, M. D., Graul, M., and Taner, M. T. (2007). Instantaneous attributes- the what and the how: *ASEG* Extended Abstract: 19th Geophysicical Conference, 1-5.

Weber, K. J., and E. Daukoru. (1975). Petroleum geology of the Niger Delta: Ninth World Petroleum Congress Proceedings, 209–221.

Weber, K. J. (1971). Sedimentological aspects of oil fields in the Niger delta: *Geologie en Mijnbouw*, 50, 559-576.

Whiteman, A. (1982). Nigeria: Its Petroleum Geology, Resources and Potential: London, Graham and Trotman, 394.

Widess, M. B. (1973). How thin is thin bed? Geophysics, 38, 1176-1180.

Wood, J. Lesli, Daniel Pecuch and Ben Schulein. (2000). Seismic attribute and sequence stratigraphic integration methods for resolving reservoir geometry in San Jorge Basin, Argentina: *The Leading Edge*, 952-962.

Worrall, D. M., Bourque, M. W., and Steele, D. R. (2001). Exploration in deep water basins…where next? *in* R. H. Fillon, N. C. Rosen, P. Weimer, A. Lowrie,H.W. Pettingill, R. L. Phair, H. H. Roberts, and B. Van Hoorn, eds., 2001, Petroleum systems of deepwater basins: global and Gulf and Mexico experience: Gulf Coast Section *SEPM* Foundation Bob F. Perkins 21st Annual Research Conference, 273.

Wu, S., and Bally, A. W. (2000). Slope tectonics—Comparisons and contrasts of structural styles of salt and shale tectonics of the northern Gulf of Mexico with shale tectonics of offshore Nigeria in Gulf of Guinea, in W. Mohriak and M. Talwani, eds., Atlantic rifts and continental margins: *American Geophysical Union*, 151–172.

Zavala, C; Gaurero, H; and Arcuri, M. (2006). Lofting rhytthmites: A diagenetic feature for the recognition of hyperpycnal deposits (abs.): *Geological society of America* Abstracts with Programs, 38, (7), 541.

Appendix A

A1. Mathematical derivation of rock physics velocities and elastic constants

Considering displacement vector in the 3 different direction of x, y and z for a unit volume of rock (Appendix A1), the relationship between stress and strain can be expressed using Hooke's law as below.

$T_{ij} = \lambda\delta_{ij}\alpha_{xx} + 2\mu\alpha_{ij}$ (normal stress) and $T_{ij} = \mu\alpha_{ij}$ (Shear stress)

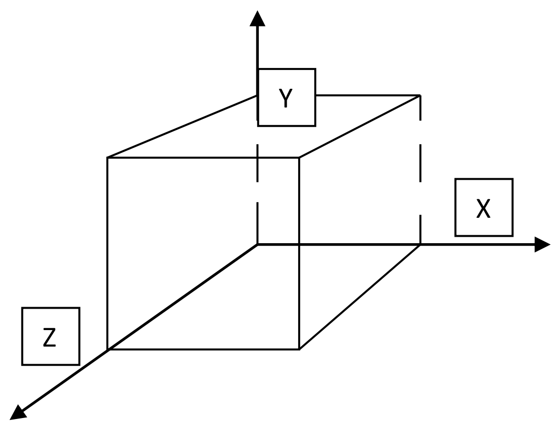

Appendix A1: Elemental volume of rock.

According to Newton's 2nd law of motion, Force =mass x acceleration i.e F =ma.

Thus, the total force acting on a solid rock of elemental volume (ΔV) to produce displacement (U) in the x – coordinate direction can be represented as

$F_x = Ma_x$ where a_x = acceleration = $\frac{\partial^2 u}{\partial t^2}$ { 2nd derivative of displacement (u)}.

But mass = density (ρ) x volume (ΔV) ; $M = \rho\Delta V = \rho\,\Delta x\,\Delta y\,\Delta z$

Therefore, $F_x = \rho\Delta x\Delta y\Delta z\,\frac{\partial^2 u}{\partial t^2}$ (A1)

Also Force = stress x area. Hence, for normal and shear stress acting along the three co-ordinate directions in appendix A1,

$$F_x = \left(\frac{\partial T_{xx}}{\partial x} + \frac{\partial T_{Xy}}{\partial y} + \frac{\partial T_{xz}}{\partial z} \right) \Delta x \Delta y \Delta z \tag{A2}$$

Where T_{xx} = normal stress, Txy and Txz = shear stress

By equating (A1) and (A2)

$$\left(\frac{\partial T_{xx}}{\partial x} + \frac{\partial T_{Xy}}{\partial y} + \frac{\partial T_{xz}}{\partial z} \right) = \frac{\rho \partial^2 u}{\partial t^2} \tag{A3}$$

For a three dimensional solid, Hooke's law relates stress and strain by the tensor equations

$T_{ij} = \delta_{ij} \lambda\, \theta + 2\mu\alpha_{ij}$ where T_{ij} = stress and δ_{ij} = Kroneka delta

and (λ μ) elastic constant.

If i=j then $\delta_{ij} = 1$ $\quad$ $T_{ij} = \lambda\, \theta + 2\mu \propto_{ii}$ (For normal stress)

But if $i \neq j$ $\quad$ $T_{ij} = \mu\alpha_{ii}$ (for shear stress)

By substituting the appropriate elastic constants, stress and strain in the tensor equations, in an elastic isotropic medium, the following equation results.

$T_{xx} = \lambda\, \theta + 2\mu\alpha_{xx}$ (A4) where $\propto_{xx} = \frac{\partial u}{\partial x}$

$T_{yy} = \lambda\, \theta + 2\mu\alpha_{yy}$ (A5) where $\propto_{yy} = \frac{\partial v}{\partial y}$

$T_{zz} = \lambda\,\theta + 2\mu\alpha_{zz}$ (A6) where $\propto_{zz} = \frac{\partial w}{\partial z}$

$T_{xy} = \lambda\,\theta + 2\mu\alpha_{xy}$ (A7) where $\propto_{xy} = \frac{\partial u}{\partial y} + \frac{\partial v}{\partial x}$

$T_{xz} = \lambda\,\theta + 2\mu\alpha_{xz}$ (A8) where $\propto_{xz} = \frac{\partial w}{\partial x} + \frac{\partial u}{\partial z}$

$T_{yz} = \lambda\,\theta + 2\mu\alpha_{yz}$ (A9) where $\propto_{zy} = \frac{\partial w}{\partial y} + \frac{\partial v}{\partial z}$

u, v, and w are displacement along x, y, and z direction respectively. By substituting the appropriate strain for stress in equation A3

$$(\lambda + \mu)\frac{\partial\theta}{\partial x} + \mu\left[\frac{\partial^2 u}{\partial x^2} + \frac{\partial^2 u}{\partial y^2} + \frac{\partial^2 u}{\partial z^2}\right] = \frac{p\partial^2 u}{\partial t^2} \quad \text{(A10)}$$

Similarly $(\lambda + \mu)\frac{\partial\theta}{\partial x} + \mu\left[\frac{\partial^2 v}{\partial x^2} + \frac{\partial^2 v}{\partial y^2} + \frac{\partial^2 v}{\partial z^2}\right] = \frac{p\partial^2 v}{\partial t^2}$ (A11)

$$(\lambda + \mu)\frac{\partial\theta}{\partial z} + \mu\left[\frac{\partial^2 w}{\partial x^2} + \frac{\partial^2 w}{\partial y^2} + \frac{\partial^2 w}{\partial z^2}\right] = \frac{p\partial^2 w}{\partial t^2} \quad \text{(A12)}$$

Where $\theta = \propto_{xx} + \propto_{yy} + \propto_{zz} = \frac{\partial u}{\partial x} + \frac{\partial u}{\partial y} + \frac{\partial w}{\partial z}$

For a plane wave propagating in the x – direction, partial derivatives

w.r.t. y and z = 0 ⇒ $(\lambda + 2\mu)\frac{\partial^2 u}{\partial x^2} = \frac{\rho\partial^2 u}{\partial t^2}$

$$\therefore \quad \frac{\lambda+2\mu}{\rho} = \frac{\frac{\partial^2 u}{\partial x^2}}{\frac{\partial^2 u}{\partial t^2}} = \frac{\partial x^2}{\partial t^2} = \left[\frac{\partial x}{\partial t}\right]^2 = V^2$$

Hence $V_p = \sqrt{\frac{\lambda + 2\mu}{\rho}}$ (Primary wave velocity) (A13)

By solving for shear stress in equation A8 and A9 for a seismic wave propagating in the x-direction, then the shear wave equations becomes

$$\mu \frac{\partial^2 v}{\partial x^2} = \frac{\rho \partial^2 v}{\partial t^2} \quad \text{(A14)} \quad \text{and} \quad \mu \frac{\partial^2 w}{\partial x^2} = \frac{\rho \partial^2 w}{\partial t^2} \quad \text{(A15)}$$

Hence, $V_s = \sqrt{\frac{\mu}{\rho}}$ (Secondary wave velocity) (A16)

Equations A13 and A16 constitute the main equations for rock physics analysis and interpretation. Lambda (λ), incompressibility modulus and mu(μ), rigidity modulus are important elastic constants, which are combined with density (ρ) to compute all other elastic rock physics properties (Equations A17 to A26).

i. Acoustic impedance: This is the product of compressional velocity and density. It is expressed as $I_p = \rho v_p$ (A17)

   where $I_p =$ primary wave impedance (acoustic impedance), $\rho =$ density, and $v_p =$ primary wave velocity.

ii. Shear impedance: This is the product of shear velocity and density. It is expressed as $I_s = \rho v_s$ (A18)

   where $I_s =$ Shear wave impedance , $\rho =$ density, and $v_s =$ secondary wave velocity.

iii. Compressional-shear velocity ratio: This is the ratio of primary wave velocity to the secondary wave velocity, Vp/Vs.

iv. Lambda, λ: This is referred to as the first Lame's parameter or incompressibility modulus. This can be expressed as $\lambda = \kappa - 2\mu / 3$ (A19)

v. Mu, μ: This is referred to as the second Lame's parameter or rigidity modulus. It is also known as the shear modulus and is defined as the ratio of the shear stress to the shear strain.

It can be expressed as $\mu = 3(\kappa - \lambda)/2$ (A20)

vi. Bulk modulus, κ: This is the ratio of hydrostatic stress to the volumetric strain. It is the reciprocal of the compressibility and is widely used to describe the volumetric compliance of liquid, solid, or gas. Bulk modulus can be expressed as $\kappa = \lambda + 2\mu / 3$ (A21)

vii. Young modulus, E: This is defined as the ratio of extensional stress to the extensional strain in a uniaxial stress state. It is expressed as

$$E = \mu \frac{3\lambda + 2\mu}{\lambda + \mu} \quad \text{(A22)}$$

viii. Poisson's ratio, δ: This is defined as the negative ratio of the lateral strain to the axial strain in a uniaxial stress state. It can be expressed as

$$\delta = -\frac{\lambda}{2(\lambda + \mu)} \quad \text{(A23)}$$

ix. Mu-rho, $\mu\rho$:This is a measure of rigidity and is expressed as $\mu\rho = (\rho v_s)^2$ (A24)

x. Lambda-rho, $\lambda\rho$: This is a measure of incompressibility and is expressed as

$$\lambda\rho = (\rho v_p)^2 - 2(\rho v_s)^2 \qquad \text{(A25)}$$

xi. Closure stress scalar, cs: It is defined by Goodway *et al*., (2010) and expressed as

$$\text{CSS}= \frac{\lambda}{\lambda + 2\mu} \qquad \text{(A26)}$$

It is an indication of brittleness and is related to how a rock will fail. It is directly related to Poisson's ratio and pore pressure variation.

Appendix B

Geostatistical Variance, Covariance and Mathematical Expectation

i. Variance is the quantitative measure of how data are distributed in space. Mathematically, variance is expressed as

$$S^2 = \frac{\sum_{i=1}^{n}\left(xi - \bar{x}\right)^2}{n-1} \tag{B1}$$

where S^2 =sample variance, $\bar{x}$ =sample mean, and n=total number of samples.

The square root of variance is called standard deviation.

By definition, variance , Var(X)= $E\left(X^2\right) - \left[E(X)\right]^2$, where E=expected value (arithmetic mean).

ii. Covariance measures the similarity between two variables. Hence, if two variables are not related, the covariance will be close to zero. Mathematically, covariance can be expressed as

$$C(x,y) = \frac{1}{n}\sum_{i-1}^{n} x_i y_i - \frac{1}{n}\sum_{i=1}^{n} x_i \sum_{i=1}^{n} y_i \tag{B2}$$

where x_i and y_i=samples of the variable x and y respectively, n=total number of sample pairs.

When x=y, covariance =variance.

If x and y are the same variable separated by lag distance L, then covariance becomes

$$C[x(u), x(u+L)] = \frac{1}{n}\sum_{i=1}^{n} x(u_i)x(u_i + L) - \frac{1}{n}\sum_{i=1}^{n} x(u_i)\frac{1}{n}\sum_{i=1}^{n} x(u_i + L) \tag{B3}$$

where L=distance between two variables called lag distance, $x(u)$=value of x at location u, and $x(u+\mathrm{L})$=values of x at location u+L

In practice covariance can be expressed as the functions that relate two variables separated by distance, L.

Hence, for first order stationarity, $f\left[X\left(\vec{u}\right)\right] = f\left[X\left(\vec{u}+\vec{L}\right)\right]$ (B4)

where $f[\ ]$=any function of a random variable, and $\left(\vec{u}\right)$ and $\left(\vec{u+L}\right)$ define the two locations of the random variable.

Equation B4 can also be expressed as another function called expected value.

Expected value, $E\left[X\left(\vec{u}\right)\right] = E\left[X\left(\vec{u}+\vec{L}\right)\right]$ (B5)

Within the region of stationarity, the expected value equal to the arithmetic mean of the random variable.

The second order stationarity assumes that the covariance is a function of only the vector,L and not the variable itself.

$$f\left[X\left(\vec{u}_1\right), X\left(\vec{u}_1+\vec{L}\right)\right] = f\left[X\left(\vec{u}_2\right), X\left(\vec{u}_2+\vec{L}\right)\right] \quad \text{(B6)}$$

This implies that covariance, C will become

$$C\left[X\left(\vec{u}_1\right), X\left(\vec{u}_1+\vec{L}\right)\right] = C\left[X\left(\vec{u}_2\right), X\left(\vec{u}_2+\vec{L}\right)\right] \quad \text{(B7)}$$

Equation B7 can also be written as

$$C\left[X\left(\vec{u}\right), X\left(\vec{u}+\vec{L}\right)\right] = C\left(\vec{L}\right) \quad \text{(B8)}$$

Hence, covariance can be expressed as

$$C\left[X\left(\vec{u}\right), X\left(\vec{u}+\vec{L}\right)\right] = E\left[X\left(\vec{u}\right), X\left(\vec{u}+\vec{L}\right)\right] - E\left[X\left(\vec{u}\right)\right], E\left[X\left(\vec{u}+\vec{L}\right)\right] \quad \text{(B9)}$$

Equation B9 can still be simplified as

$$C\left[X\left(\vec{u}\right), X\left(\vec{u}+\vec{L}\right)\right] = E\left[X\left(\vec{u}\right), X\left(\vec{u}+\vec{L}\right)\right] - \left(E\left[X\left(\vec{u}\right)\right]\right)^{2} \quad \text{(B10)}$$

Appendix C

Seismic data frequency spectra between 1.8 seconds to 6.0seconds

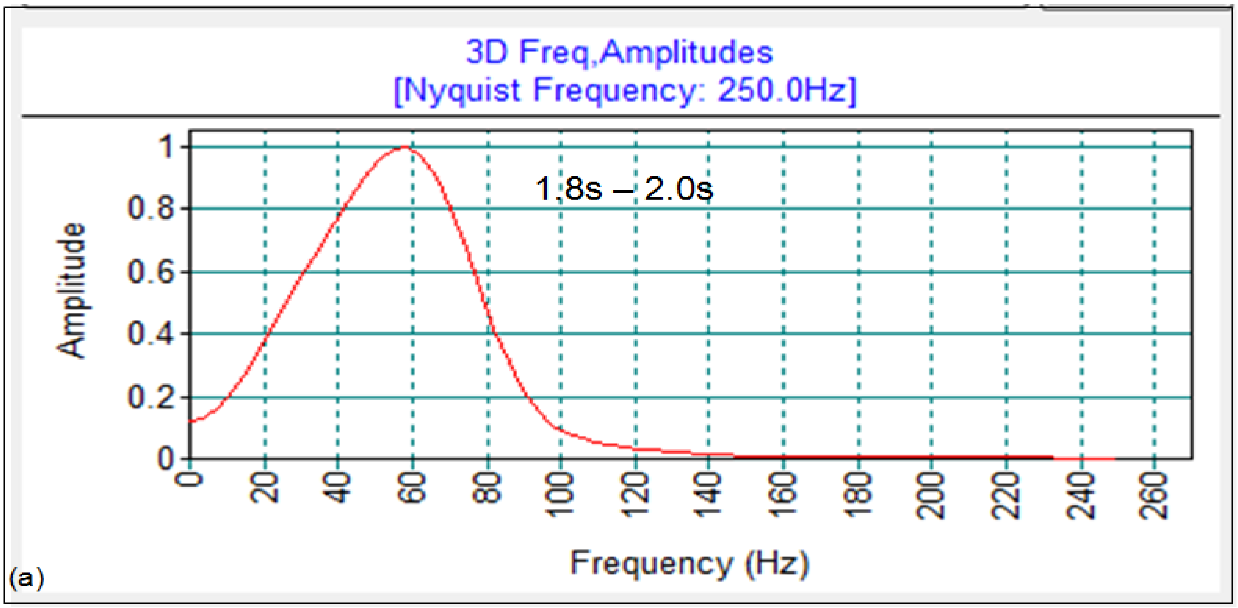

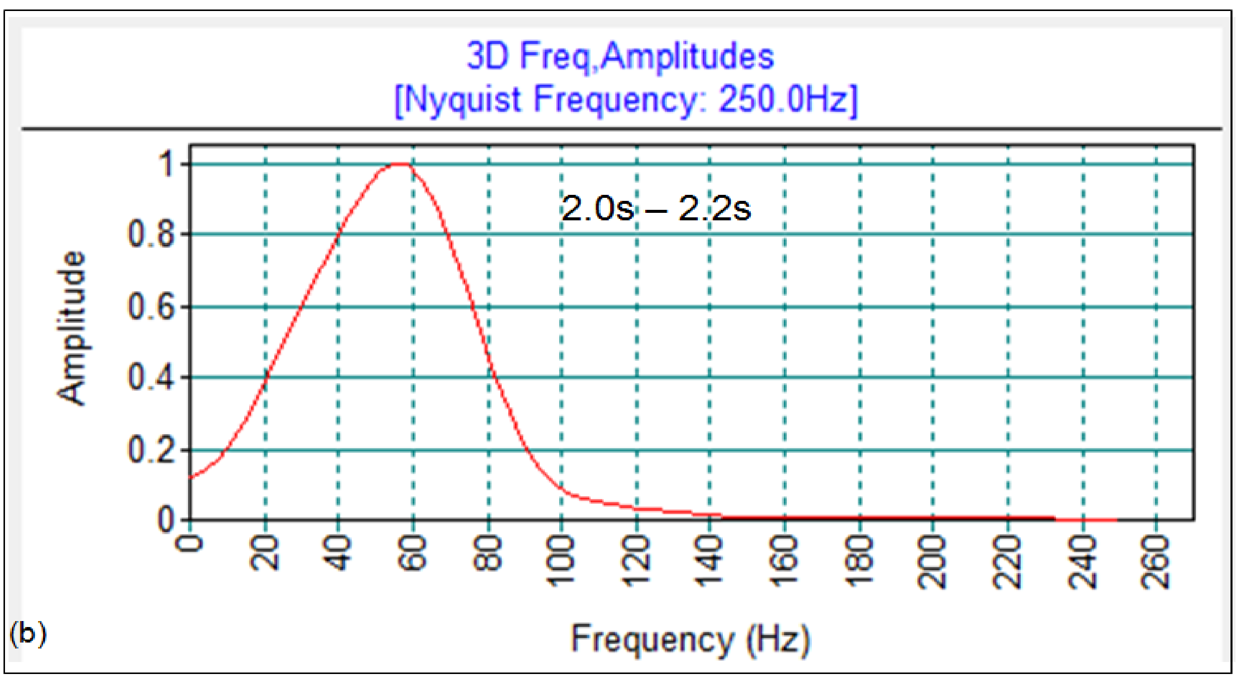

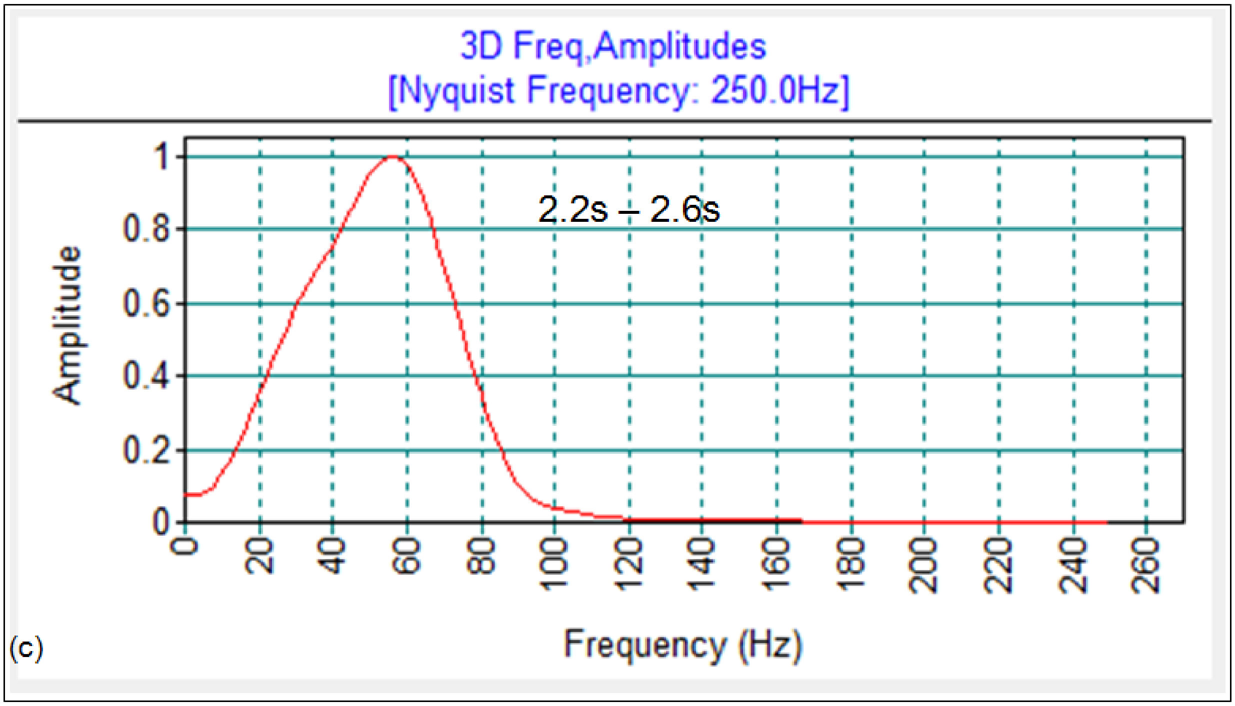
3D Freq,Amplitudes
[Nyquist Frequency: 250.0Hz]
2.2s – 2.6s
Amplitude
Frequency (Hz)
(c)

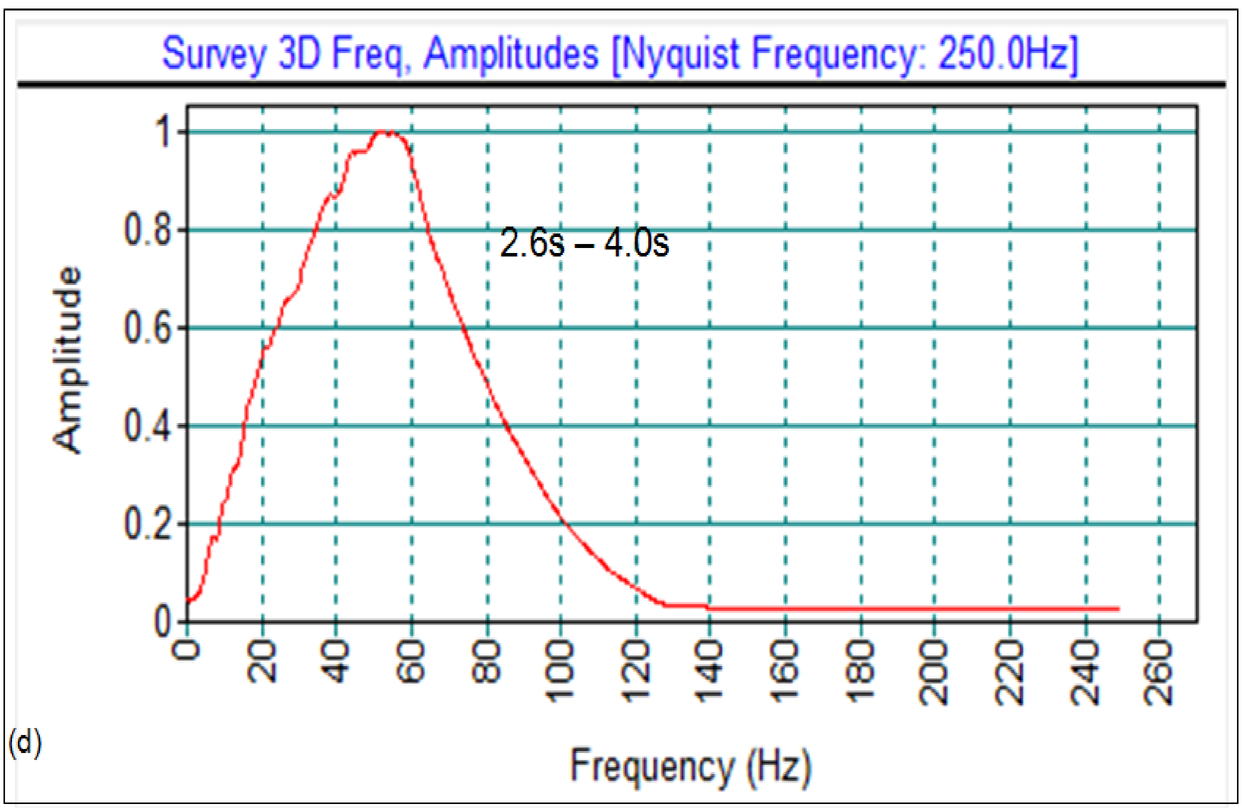
Survey 3D Freq, Amplitudes [Nyquist Frequency: 250.0Hz]
2.6s – 4.0s
Amplitude
Frequency (Hz)
(d)

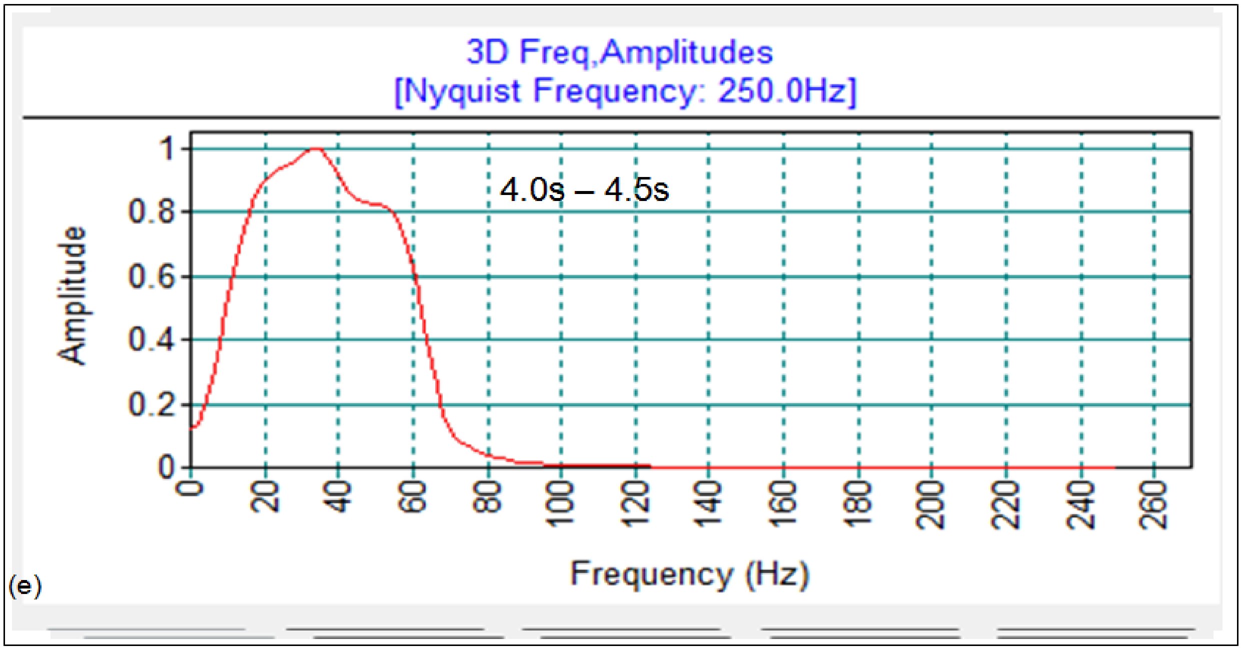
3D Freq,Amplitudes
[Nyquist Frequency: 250.0Hz]
4.0s – 4.5s
Amplitude
Frequency (Hz)
(e)

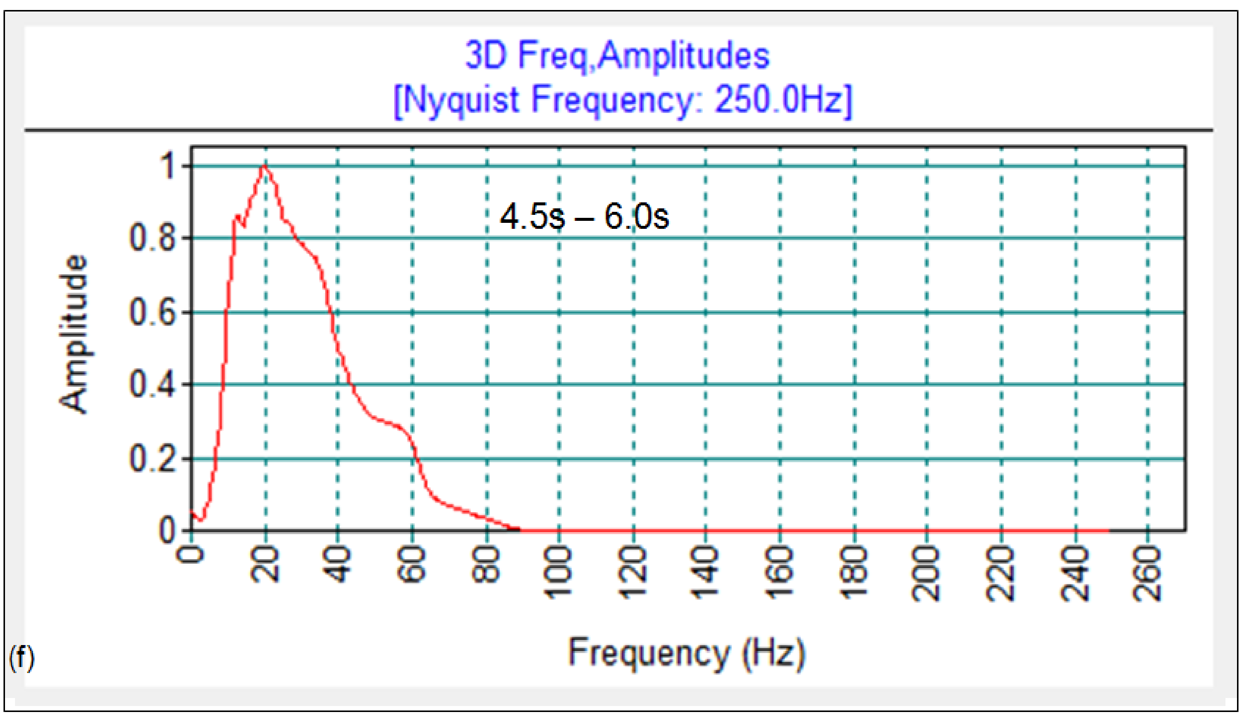
3D Freq,Amplitudes
[Nyquist Frequency: 250.0Hz]
4.5s – 6.0s
Amplitude
Frequency (Hz)
(f)

Appendix D

Day light core photographs

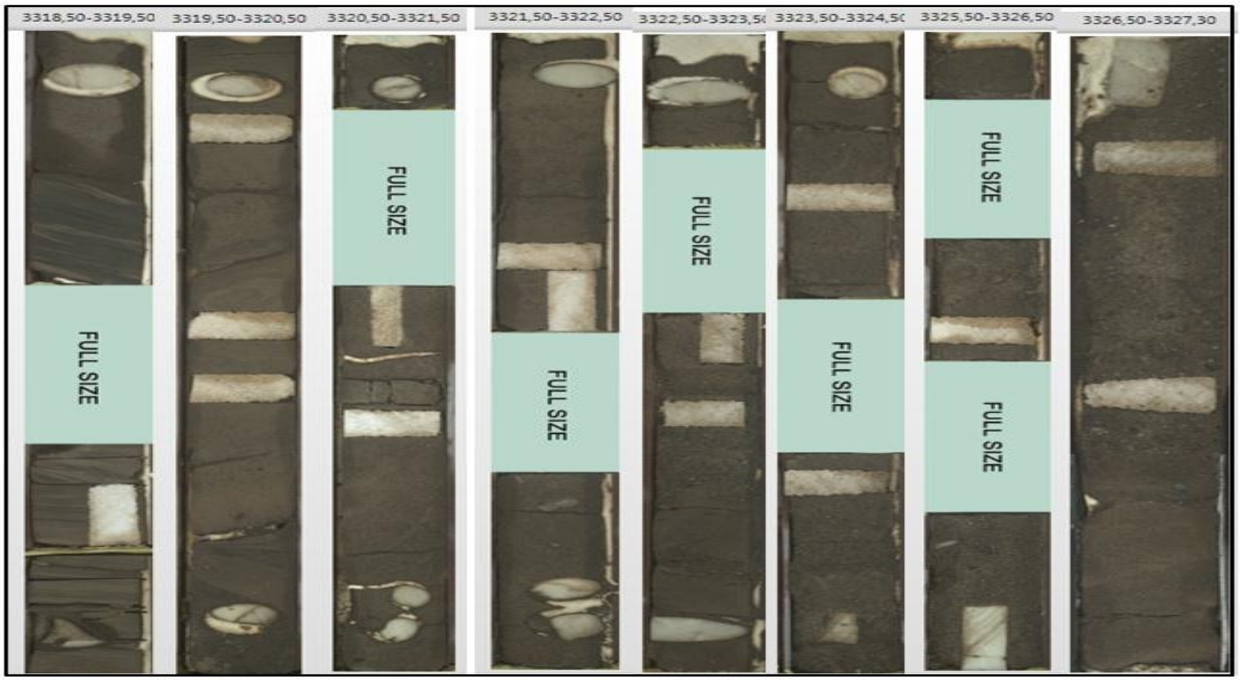

Figure D1 Core photograph from 3318.50m to 3327.30m in Well-5

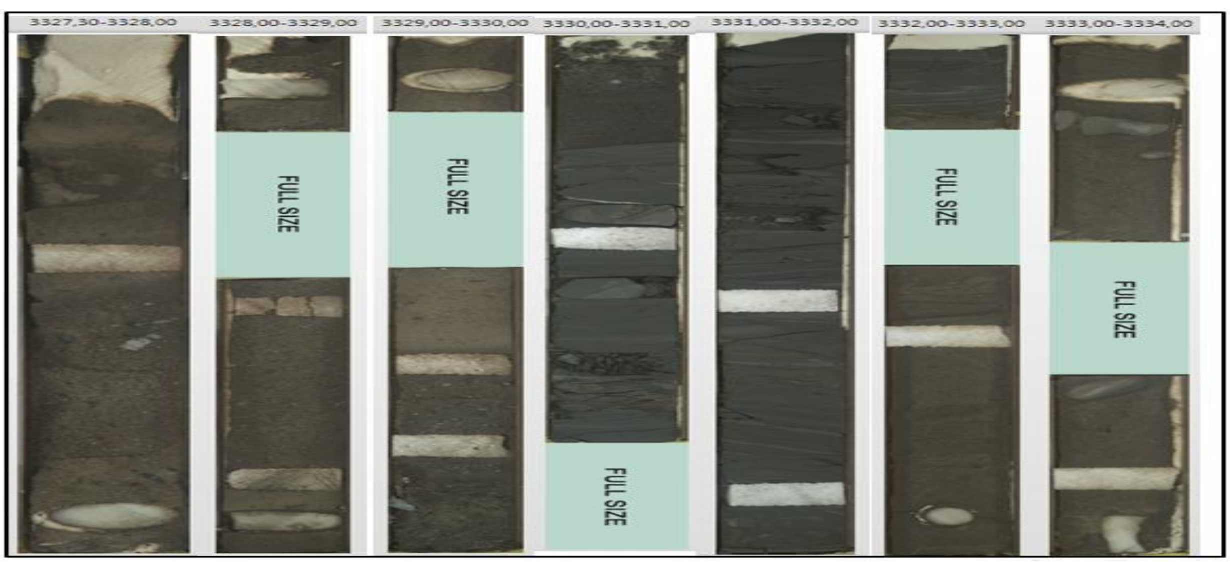

Figure D2 Core photograph from 3327.30m to 3334m in Well-5

Figure D3 Core photograph from 3334.0m to 3340.0m in Well-5

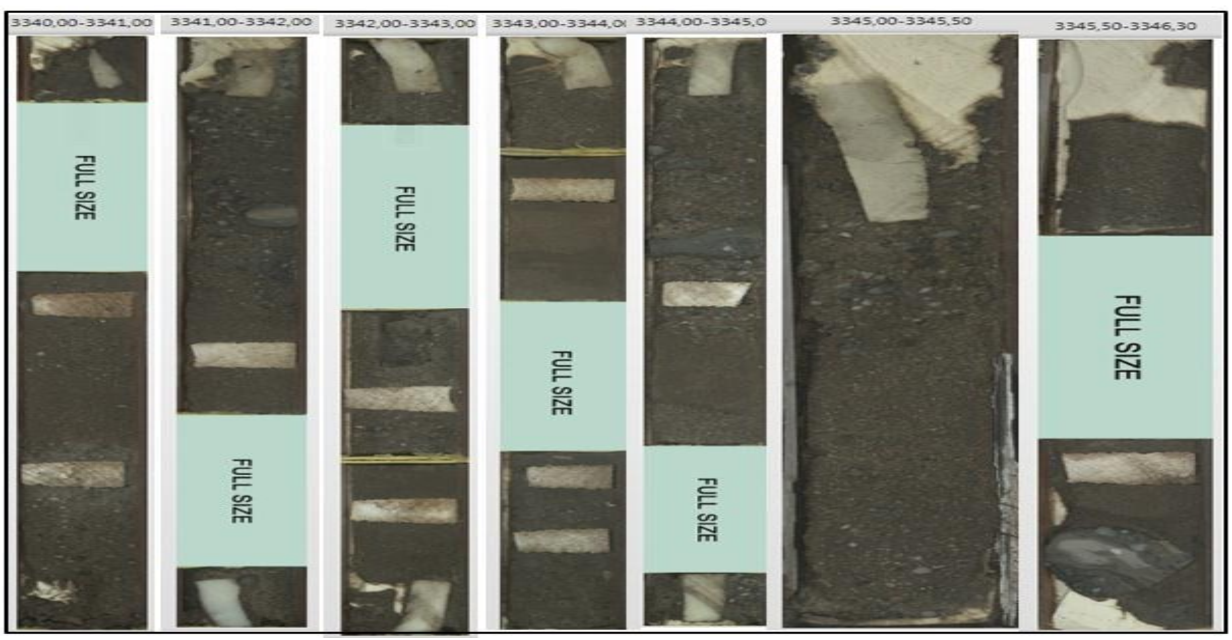

Figure D4 Core photograph from 3340m to 3346.30m in Well-5

Figure D5 Core photograph from 3121.0m to 3130.93m in Well-4

Figure D6 Core photograph from 3383.50m to 3394.41m in Well-4

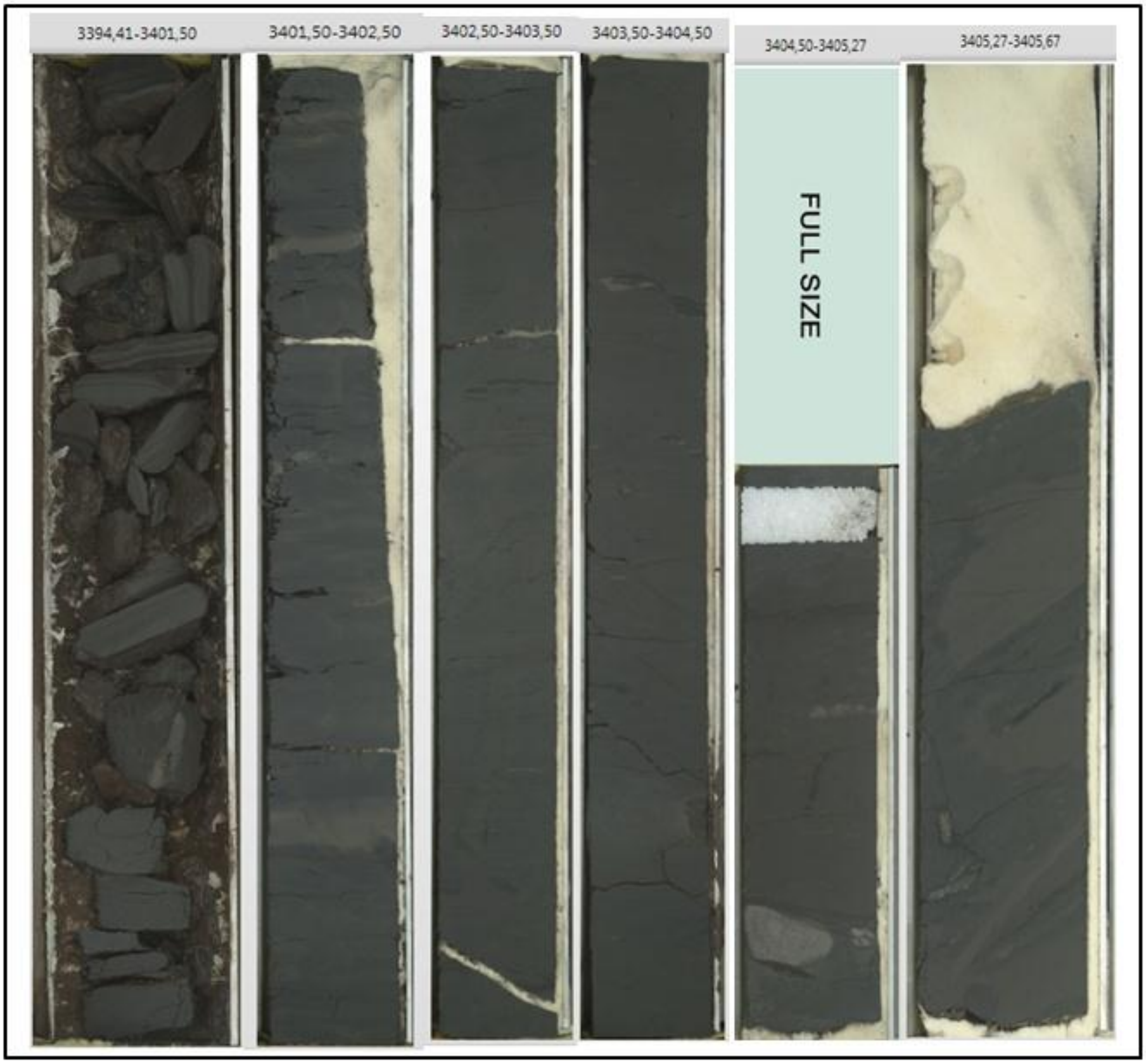

Figure D7 Core photograph from 3394.41m to 3405.67m in Well-4

Appendix E

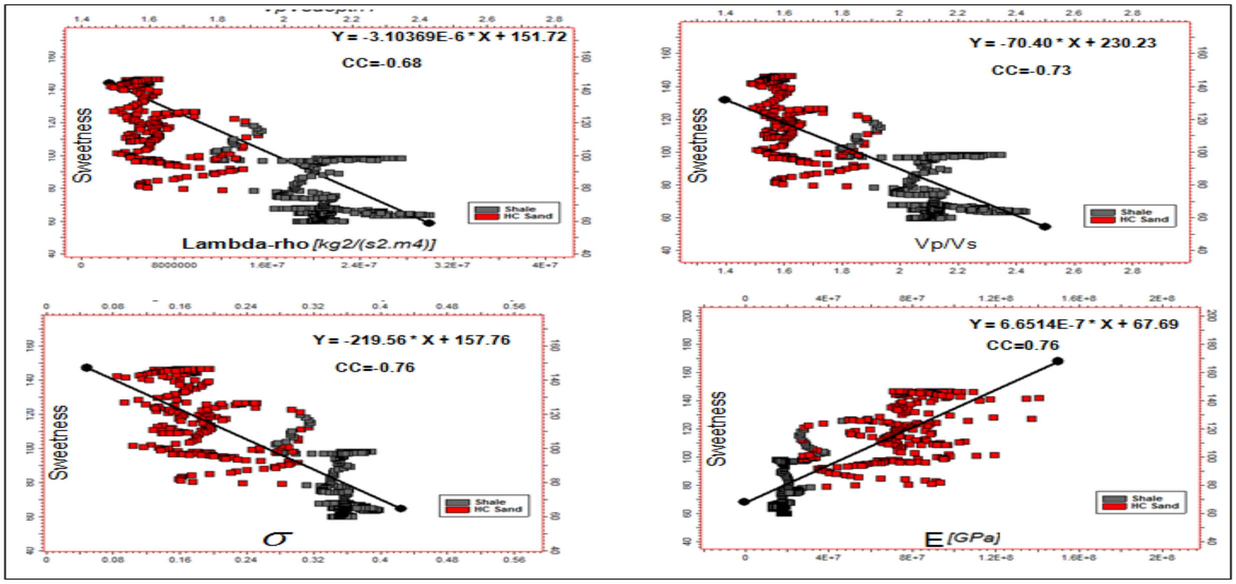

Figure E1 Sweetness attribute versus elastic rock properties correlation in sand.

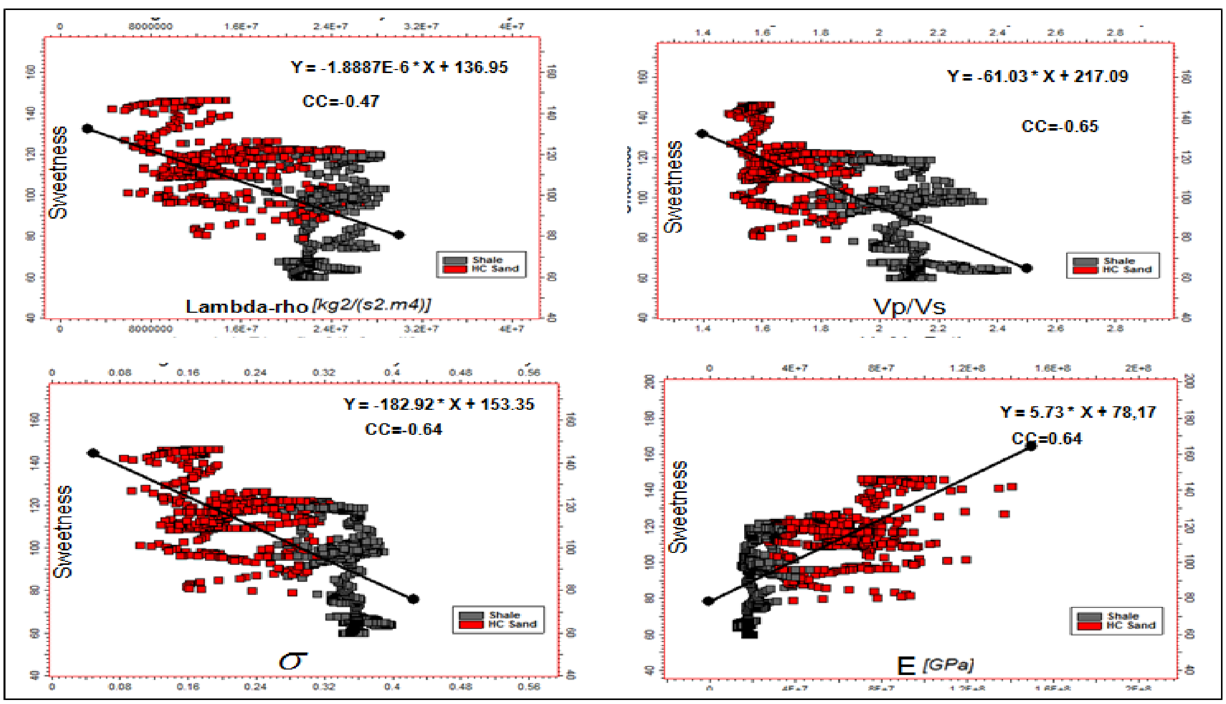

Figure E2 Sweetness attribute versus elastic rock properties correlation in shaly sand.

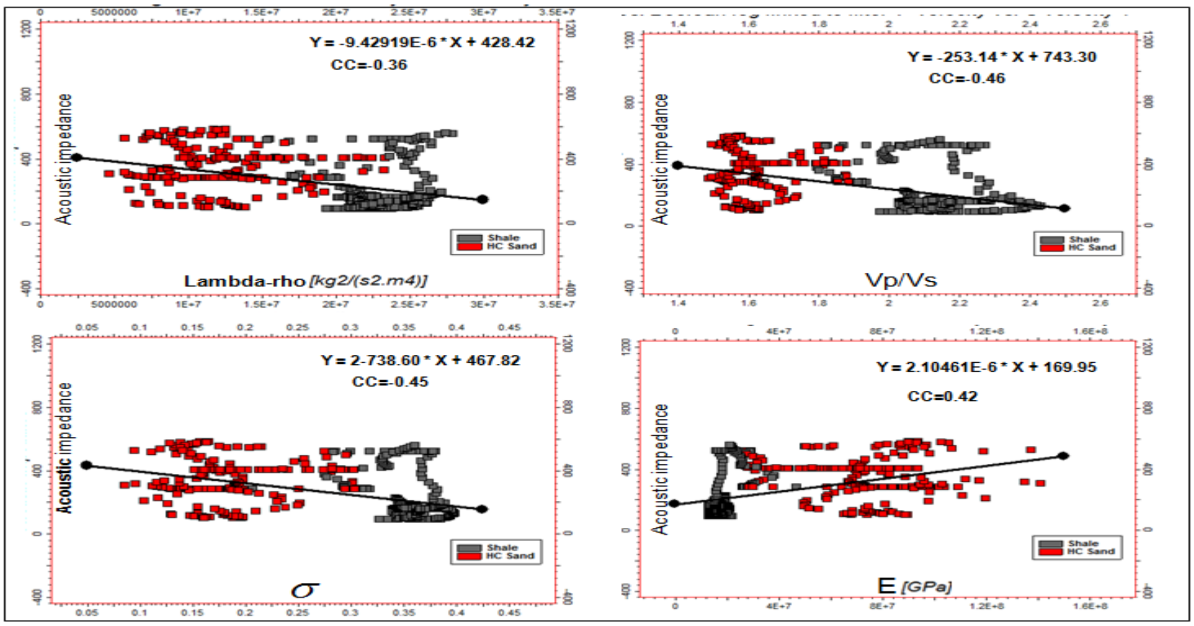

Figure E3 Acoustic impedance attribute versus elastic rock properties correlation in sand.

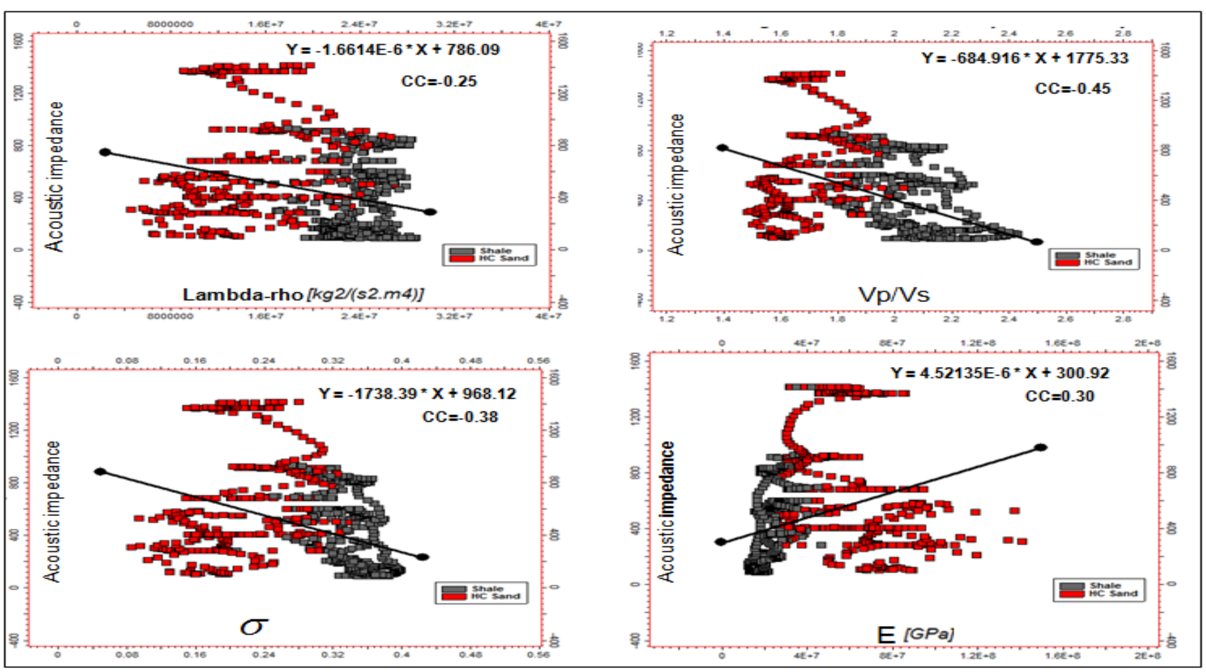

Figure E4 Acoustic impedance attribute versus elastic rock properties correlation in shaly sand.